THESE DE DOCTORAT DE L’ETABLISSEMENT UNIVERSITE BOURGOGNE FRANCHE-COMTE

PREPAREE AU LABORATOIRE INTERDISCIPLINAIRE CARNOT DE BOURGOGNE

Ecole doctorale n°553

École doctorale Carnot Pasteur

Doctorat de Physique

Par

Konstantin Malchow

Light from electrically driven nanogaps

Thèse présentée et soutenue à Dijon, le 26.07.2022

Composition du Jury :

Alain Dereux	Professeur à l’Univ. de Bourgogne	Président
Christophe Couteau	Professeur à l’Univ. Technologie de Troyes	Rapporteur
Christophe Galland	Professeur à l’ EPF Lausanne	Rapporteur
Pascal Martin	Professeur à l'Université de Paris Cité	Examinateur
Guillaume Schull	Directeur de Recherche CNRS, Univ. Strasbourg	Examinateur
Alexandre Bouhelier	Directeur de Recherche CNRS, Univ. Bourgogne	Directeur de thèse

ECOLE DOCTORALE
CARNOT - PASTEUR

Title : Light from electrically driven nanogaps: From electroluminescence to overbias emission

Keywords : tunnel junction, memristors, overbias light emission, nonlinear photoluminescence, nano-optics, electro-optical antennas

Abstract : The quest for more energy efficient on-chip transmission has driven the search of small electrically modulable light sources with sizes comparable to current on chip transistors. This thesis is interested in the light emission of a class of very small and surprisingly simple structures: Two metal electrodes separated by a small dielectric gap. In spite of their simple structure these devices show a variety of different physical behaviors and have been investigated with growing interest in recent years. The present thesis continues this line of research by presenting different experimental approaches to characterize and analyze their radiation.

It expands the study of such junctions to larger gaps, adding new emission mechanisms to their arsenal. Larger gaps show an intricate current behavior with a history dependent conductance and light emission triggered by electro-chemical dynamics involving field-induced electroluminescent defects. The thesis investigates also the overbias light emission of ultra-small gaps, characterized by a violation of the standard quantum limit. The thesis performs second order photon correlation measurements on the nonlinear photoluminescence in metals as a preparatory step to characterize electrically driven overbias emission.

Titre : Émission de lumière d’interstices métalliques nanométriques excités électriquement

Mots clés : jonction tunnel, memristors, émission de lumière anormale, photoluminescence non-linéaire, nano-optique, antennes électro-optiques

Abstract : La recherche d'une transmission sur puce plus économe en énergie a conduit à la recherche de sources lumineuses miniatures modulables électriquement avec des tailles comparables aux transistors électroniques. Cette thèse s'intéresse à l'émission lumineuse d'une classe de structures très petites et étonnamment simples : deux électrodes métalliques séparées par un petit espace diélectrique. Malgré leur structure simple, ces dispositifs présentent une variété de comportements physiques différents et ont été étudiés avec un intérêt croissant ces dernières années. La thèse poursuit cette ligne de recherche en présentant différentes approches expérimentales pour caractériser et analyser leur rayonnement.

Elle étend l'étude de telles jonctions à de plus grands interstices, ajoutant de nouveaux mécanismes d'émission à leur arsenal. Des grands interstices montrent un comportement de courant complexe avec une conductance dépendante de l'histoire et une émission de lumière déclenchée par une dynamique électrochimique impliquant des défauts électroluminescents induits par le champ. La thèse étudie également l'émission de lumière anormale des interstices ultra-petits, caractérisée par une violation de la limite quantique standard. La thèse propose des mesures de corrélation de photons de second ordre sur la photoluminescence non linéaire dans les métaux en tant qu'étape préparatoire pour caractériser l’emission des photons émis en régime anormal.

UBFC
UNIVERSITE
BOURGOGNE FRANCHE-COMTE

Université Bourgogne Franche-Comté
32, avenue de l’Observatoire
25000 Besancon

Light from electrically driven nanogaps

From electroluminescence to overbias photon emission

Konstantin Malchow

Acknowledgements

Although a PhD thesis might appear as a lonely quest of several years, pursued by temerarious students just to obtain the doctor title, such an endeavor in reality is not possible without the support, counsel and input from supervisors, colleagues and friends.

This thesis work is no different.

Therefore I would like to mention here a few persons who helped me throughout these four years. In particular I would like to thank my supervisor Alexandre Bouhelier. First training me in fabrication and optical experiments, ready to help when needed, then being a partner in the interpretation of these results and on which experiments to perform next, and finally forcing me to order my confused thoughts and making sure that this thesis would be comprehensible to outside readers.

I also very much enjoyed the interactions with my collaborators Bojun Cheng and Till Zellweger from the institute of electromagnetic fields at ETH Zurich. Together we pursued and discussed experiments, typically during short intense one week sessions in Dijon, where I learned better how to do electrical measurements and discovered even more good restaurants.

I was lucky to have also nice and encouraging lab colleagues and office mates such as Adrian Agreda, Reinaldo Chacon, Dimitri Rusakov, Deepak Kumar Sharma, Xiao Yu, Florian dell'Ova, Sarah Hamdad and more. Whenever needed, I could ask them for help and we had fruitful discussion over lunch and coffee breaks, and fun while performing activities outside the lab. A special mention goes to Dr. Aymeric Leray who provided help in fitting both the lifetime measurements of Chapter 3 and input for the discussion and fitting of the photon autocorrelations. I also thank all the members of the ARCEN platform for their support in using the fabrication facilities.

Last but not least, I would like to thank all flatmates and friends met during my stay in Dijon, they often helped me to shift my focus away from my thesis and reminded me to enjoy life.

Table of contents

Chapter 1.

Introduction, motivation and overview of this thesis

The structures investigated in this thesis are quite simple: two thin metal surfaces, acting as electrodes, sitting on top of a standard glass cover slip and separated by a gap of 50 nm or smaller. And yet, by applying a low electrical voltage, such as one that can be obtained from standard AA-batteries, these structures emit light.

This is at first glance surprising, as we typically associate light emission to the presence of a specific radiating body, be it a hot tungsten filament or a luminescent semiconductor. Nonetheless, in our experiments, the presence of light is always attributed to the gap region with a priori no native active materials. The study of these radiation phenomena is the subject of this thesis with the objective to understand how light is emitted from nanoscale dielectric gaps.

This is not only motivated by a fundamental fascination and scientific interest of electrical generated light emission at small scales. The research on electrically driven nano-sized light sources is spurred by practical applications. In particular, the conversion of an electrical signal into an optical signal on a scale similar to the transistor size, is of paramount importance to the development of optical interconnects for integrated circuits. The gap devices studied in this thesis have no pretension to provide a final solution, as these devices lack in brightness and efficiency. They are rather an exploration of smaller sources with a relative simple fabrication process compared to the current candidates. This will be detailed in the following sections of this introduction chapter.

1.1. Electro-optical transducers for optical interconnects

1.1.1. The need for optical interconnects

Today, it is rare to find any technology without some form of integrated circuit. From washing machines to smartphones and the internet, electronic chips are ubiquitous in our every day life. Over the past century, these circuits have become faster and more powerful due to technological advancements at improving and miniaturizing elementary processing elements. Commercially available transistors have been nowadays reduced to dimensions of 5 nm (for example in Apple's M-processors) [1], and IBM reported the fabrication of 2 nm size transistors (not commercially available) [2].

However, further improvement of integrated circuits is currently not only limited by the transistors itself, but also by the transmission of information between different processing elements [3–5] through electrical interconnects. These connections have intrinsic physical limitations in speed and power consumption [6]. This limit is an important technological and environmental issue, as a steady increase of data flow and energy consumption has been observed in the internet and data centers in the past years [7–10], accounting in 2020 for an estimated 1.1% of the global power consumption.

1.1.2. Integrated optical interconnects

A possible solution to overcome the issue of electrical interconnects is to replace them by optical counterparts [4, 5, 12]. This has been proposed already in 1984 [13]. Optical interconnects have been first implemented for long haul communications such as optical fibers for high speed internet and are implemented now in ever shorter distances for example in board-to-board communication within the same data center [14].

To provide a data link between different electronic components, an optical interconnect needs to have at least three elements. The first, called transducer, converts an electrical signal onto an optical signal. This signal is then transported through an optical link, such as an optical waveguide [11, 14], to the receiver, which converts back the optical signal into electrical information. This signal is then further processed [4, 14].

According to [4], in order for optical interconnects to be competitive with electrical interconnects, the optical interconnect, with all its elements combined together, should allow data transmission with speeds of at least 14.3 GHz and have energy cost per transmitted bit in the order of 10 fJ, equivalent to about $6 \cdot 10^4$ eV. This is still about 100 times the minimal (thermal limited) energy

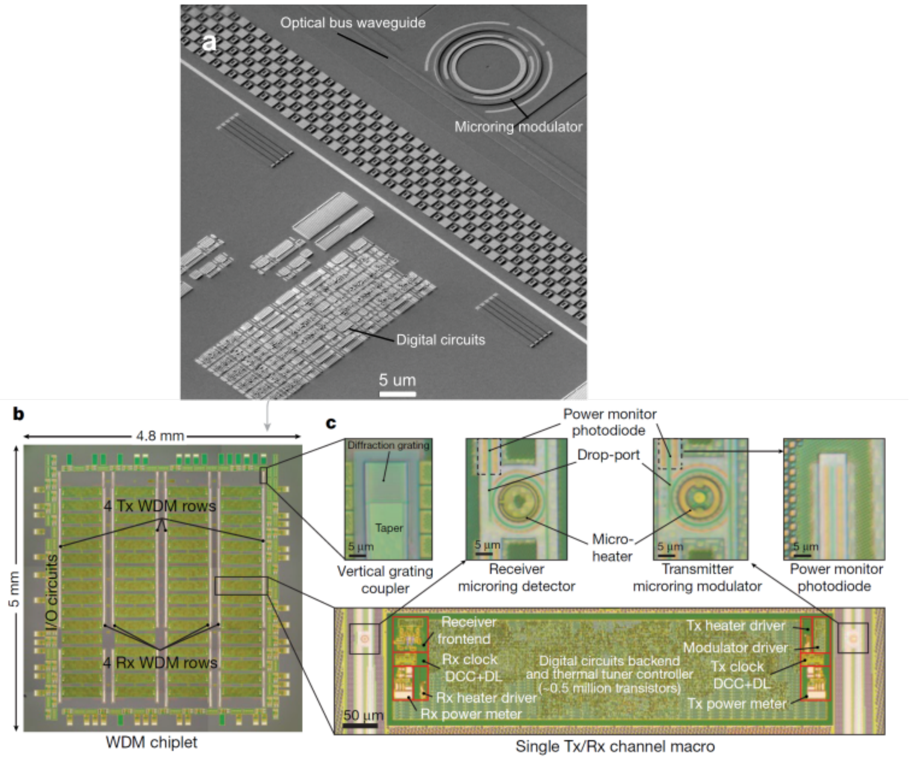

Figure 1.1.: *Implementation of an on chip optical interconnect. In a) SEM image showing both the electrical computing units (digital circuits) and the optical interconnect. In b) microscope image of a chip section, showing the structure of the chip, with in c) a highlight of the optical interconnect elements. Reprinted by permission from [11], Springer Nature © 2018.*

cost of 0.13 fJ of optical interconnects [15, 16].
Already a full implementation of on chip electro-optical interconnects has been shown in [11], illustrated here also in Figure 1.1. In the paper, data rates of 11 GHz and an energy cost of 100 fJ per transmitted bit were achieved.

The size-mismatch between electronics and photonics If one considers Figure 1.1 one distinguishes clearly a size mismatch between the optical components and the digital circuit, with the latter being considerably smaller. This size difference is due the photon wavelength of 1550 nm and the refractive index of silicon, which fundamentally limits the minimum waveguide size, in this case in [11] to a 220 nm · 400 nm cross section.

Therefore alternatives to circumvent the size limiting photonic waveguides and to shrink down the size of the optical link are also investigated, with sometimes niche applications such as plasmonic waveguides or on chip free space propagation.

By associating part of their energy to electron oscillations in metals, propagating electromagnetic waves can be confined to smaller volumes and structures, these are called surface plasmons [17]. Surface plasmons however experience propagation losses. In general, the tighter the electric field confinement, the higher the propagation losses are [18]. Still over short distances plasmonic circuits might be a valid alternative to shrink down the size required for the transmission link [19].

As an alternative one might use directly the free space propagation of photons. This requires to implement, analogous to the radio domain, optical antennas [20,21] to direct and to collect the light signal.

As this thesis work focuses on light sources, I will disregard the problematics of photon transport (the link) or detection (receiver, not at all discussed so far) in the following.

1.1.3. Electro-optical modulators

There are two approaches envisioned to transfer an electrical signal onto an optical signal [5]. The first is to electrically modulate the light emission intensity of an on-chip light source, the second is to electrically modulate the light transmission in a waveguide by an electro-optical modulator. The latter concept is used in [11] and is also seen in Figure 1.1. Although electro-optical modulators show high speed transmission rates (more than 100 GHz in [22]) and a good energy cost per bit transmitted (100 fJ, [11]), they are ultimately size-limited to about a few 100 nm scale. This limit is not given by the modulator itself, which can be shrunk down to almost single atom scale [23], but by the required waveguide whose transmission is modulated. This is considerably larger than today's transistor size of 5 nm. Electro-optical modulators are therefore more suited for larger distances of few µm than for transistor-to-transistor communication.

Next I will thus present different electrical on-chip light sources for optical signal encoding.

1.1.4. Diode lasers

Diode lasers such as vertical surface cavity emitting lasers (VCSELs), or relying on active areas within photonic crystals, have been shown to provide high data transfer speeds at low energy bit cost, which can be shrunk down to on chip sources [16]. For example more than 100 $\mathrm{Gbit\,s^{-1}}$ have been shown in [24] for a VCSEL and in [25] 10 $\mathrm{Gbit\,s^{-1}}$ data rates were achieved with an energy cost of 4.4 $\mathrm{fJ\,bit^{-1}}$ by using a photonic crystal cavity laser.

The threshold pumping energy needed for lasing and high speed modulation is shrunk when miniaturizing the laser cavities. However, this miniaturization limited to about 0.03 μm^3 necessary to maintain the lasing and modulation properties [16].
This size requirement is similar to the one needed by electro-optical modulators. Diode lasers provide thus an alternative for data transmission distances above some µm. They are however not a solution for smaller distances and require a considerable amount of fabrication complexity.

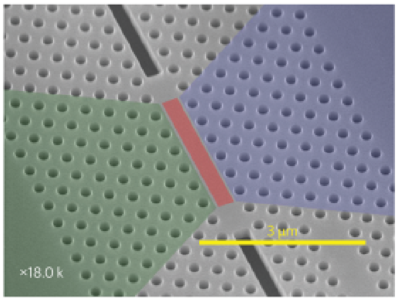

Figure 1.2.: *Photonic crystal diode laser cavity, the red area shows the active area (of light emission into the cavity) in the laser. The scale bar indicates* 3 µm. *Reprinted by permission from [25], Springer Nature © 2013.*

1.1.5. Small light emitting diodes

As an alternative to the on chip lasers, small light emitting diodes are usually proposed [5,15,16]. These diodes are potentially more energy efficient than diode lasers but lack intrinsic modulation speed due to carrrier recombination lifetimes in the order of 1 ns. This limit can be partially overcome by embedding these sources into optical cavities [15]. For example in [26] small LEDs integrated into nanopillar optical resonators and directly coupled to a waveguide showed a reduced lifetime of 290 ps with light directly modulated at 5 GHz and an efficiency up to 0.01 (at 7 K temperature). The structure of the diode is shown in Figure 1.3 and is quite elaborate, requiring several fabrication steps and multiple materials. This results in an overall size larger than 100 nm, as seen in Figure 1.3. The size limit of such sources is not limited by the luminescent material but by the optical resonator and electrode sizes. Therefore smaller light sources can be (theoretically) expected within this approach.

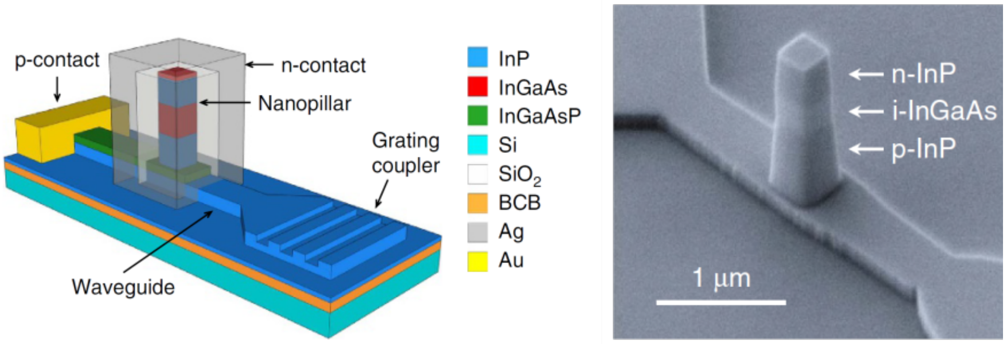

Figure 1.3.: *Small light emitting diode inside a nanopillar cavity coupled to a waveguide. On the left illustration of the device's structure, on the right a SEM image before the metal deposition to contact the device. Reprinted from [26] (CC BY 4.0).*

1.1.6. Thermal emission

Incandescent sources (such as a tungsten filament) could be an alternative to small light emitting diodes, particularly for optical links operating in the infrared spectral range. The broad emission spectrum can be engineered to a desired shape through optical resonators [27]. However the modulation speed of thermal sources is typically rather slow, limited by the thermalization processes. For conventional sources only 10 MHz in [27] have been reached.
This modulation speed has been greatly improved in graphene based sources, where, as a consequence of a small heat capacity [28, 29], modulation speeds of up to 3 GHz with electron temperatures of more than 2000 K were demonstrated.

1.2. Light emission by metal gaps

A quite different approach of generating light is found in thin metal/insulator/metal junctions relying on photon emission during inelastic electron tunneling. In particular the desire to electrically excite optical antennas analogous to their radio-frequency counterparts, has led in recent years into a renewed interest into such structures [21, 30], as illustrated in Figure 1.4. Inelastic electron tunneling is observed in thin metal/insulator/metal stacks with typical insulator thicknesses below 5 nm. This mechanism does not imply a (localized) electron

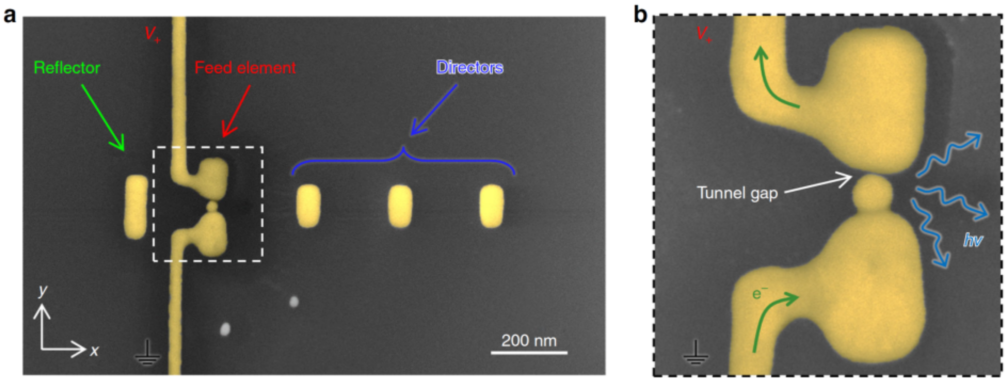

Figure 1.4.: *SEM images of an optical antenna driven by inelastic electron tunneling. In a) the full antenna, in b) a zoom into the gap light generation region. Reprinted from [21] (licensed under CC BY 4.0).*

decay from a conduction band to a valence band as in a diode (or from an excited state to ground state in a molecule). Rather light is emitted during the (delocalized) electron transition between the conductance bands of two spatially separated metal layers.

Light emission by inelastic electron tunneling was first reported in 1976 [31], with the excitation of localized surface plasmons during electron tunneling demonstrated and discussed even earlier [32, 33].

Compared to light emitting diodes, light emission by inelastic tunneling is a very fast process, which in principle is limited only by the tunneling time of a few fs [34]. However, light emission through inelastic tunneling is intrinsically not very efficient. In [35] for example an electron-to-photon conversion efficiency of $2.5 \cdot 10^{-5}$ was reported. This low yield is partially due to poor coupling of the emitted radiation with the optical far field [36] and because of the short electron interaction time during the tunneling process [37].

The efficiency can therefore be increased by improving the out-coupling efficiency, by increasing the optical emission rate through optical resonances [30,35], obtaining an emission efficiency up to 1 % [38] or by exploiting more elaborate electronic resonances [37], reaching extrapolated plasmon emission efficiency up to 25 % [39].

Inelastic tunneling is however not the only emission process occurring in metal gaps [40]. At even smaller gap separations new photon emission characteristics, radically different from inelastic tunneling, are observed.

1.3. Scope and organization of this thesis

Metal gaps (or metal insulator metal) provide thus electrically driven light sources with active area sizes (neglecting any optical resonators) comparable to the transistor size. Such structures are also the smallest engineered electrical light sources possible, as each electrical driven element requires metallic (or semiconducting) contact electrodes. Still such simple devices hide a rich variety of physical and chemical phenomena to understand their light emission and current transport.

In this thesis I investigate and characterize the electron dynamics and photon generation in metal/insulator/metal gaps while trying at the same time to uncover the physical mechanism responsible for the light emission. Although similar gap structures have been studied before, see previous section, this thesis both expands such studies to larger gap sizes and further aims to expand and characterize the previously observed light emission in ultra small gaps.

This naturally provides an overview of different photon generation mechanisms, which could be exploited in more refined devices. Along with the discovery of the gap dynamics, different experimental and theoretical analyses are explored. Each of the chapters presents a different type of device and physical mechanism at play. The chapters are ordered from larger gap sizes going successively to smaller ones, with the exception of Chapter 6, covering all gap sizes within a single device. In the following a short summary of each chapter is provided.

Chapter 2: Light emission in wide-gap gold junctions

Chapter 2 investigates the light created within wide-gap gold junctions (with gap size from 20 nm to 50 nm) on top of glass cover slips. When applying a voltage the wide-gap gold junctions react with internal configuration changes leading to distinct current properties and light emission. The behavior of these changes are described and analyzed using different experimental approaches, such as spectra and time resolved measurements to gain a clearer understanding.

Chapter 3: Silver-platinum tips embedded in SiO_2

The next device discussed is quite similar to the wide-gap gold junctions, except that the gold electrodes are replaced by silver and platinum. These are embedded in SiO_2 and separated by 10 nm to 60 nm. Whereas the silver electrode is electrochemically active, oxidizing under a positive voltage, the platinum electrode remains inert. Under the application of an electrical field these devices show a reliable and repeatable change of resistance due to a silver filament growth [41] and light is released during the resistance evolution. The similarities and differences in the observed light emission compared to the wide-gap gold junctions allows to gain further insight into the radiative mechanisms of both junctions.

Chapter 4: Overbias emission in electromigrated gold nanowires

Chapter 4 studies the light emission from very small gold gaps (less than 1 nm) showing overbias light emission, i.e. the detection of photons which cannot be emitted in a single electron process. Such gaps are obtained through carefully controlled breaking [40, 42] of very thin gold constrictions. After presenting briefly the electromigration process used to create these gaps and the observed electrical light characteristics, the two mechanisms currently envisioned to explain the overbias emission are discussed: multi-electron inelastic tunneling [43] or light emission from a hot electron bath [40].

Chapter 5: Photon bunching of the nonlinear photoluminescence in metals

Because the photon statistics reflect the emission processes at play, we aim to measure the photon correlation of the overbias emission. As an intermediate step the photon statistics is first measured using a substitute signal: the nonlinear photoluminescence in metals [44]. This photoluminescence shares a strong resemblance with the overbias emission. This chapter presents thus the photon correlation measurements of the nonlinear photoluminescence in noble metals and presents the constraints to extend these measurements to the overbias light emission and other sources.

Chapter 6: Silver filament in PMMA

The last experimental chapter summarizes the findings of the whole thesis, in studying silver to silver electrodes embedded in PMMA. By pushing the silver filament growth within these junctions from large gap sizes until the formation of a ballistic contact channel, all the light emission regimes studied in this thesis are observed.

Chapter 7: Conclusion and outlook

The last chapter summarizes this thesis work and provides a general outlook.

Chapter 2.

Light emission in wide-gap gold junctions

This chapter presents the experimental results of electrical light emission from wide-gap gold junctions: two in-plane gold electrodes deposited on top of standard glass cover slips, separated by a gap of 20 nm to 80 nm. These junctions are exposed either to ambient air or covered by a thermally sputtered SiO_2.
Stacked structures consisting of two metal metal layers separated by a insulator (with a thickness above 5-10 nm) have been already investigated more then 50 years ago [45–50] reporting consistently light emission, current hysteresis and negative differential resistance. To explain these features several hypotheses have been advanced, considering for example the defect creation and deformation of the insulator (typically an oxide) [49], ion migration from metal electrodes [48] or filament formation due to organic contaminants [47, 50, 51]. Overviews are found in [45, 50]. Very similar current and light behaviors were also observed in films of electrically disconnected gold particles [52–55].
In this chapter I will however not introduce all the different hypotheses from the above references, this is left to the interested reader. I will rather show the behavior of the wide-gap gold junctions and present the most likely hypotheses explaining the experimental observations under standard atmospheric conditions.
Since this is the first chapter discussing light emission from metal gaps, some of the concepts and discussions will also be applied to the other devices presented in this thesis. In particular, chapter 3 presenting light emission from silver-platinum memristors is closely tied to the observations of this chapter.

2.1. Fabrication

Before to present the design and structure of the gap junctions in detail, I will give here a short overview of their fabrication process, also used for the other devices presented in this thesis. A sketch of the (pretty standard) process flow is presented in Figure 2.1.

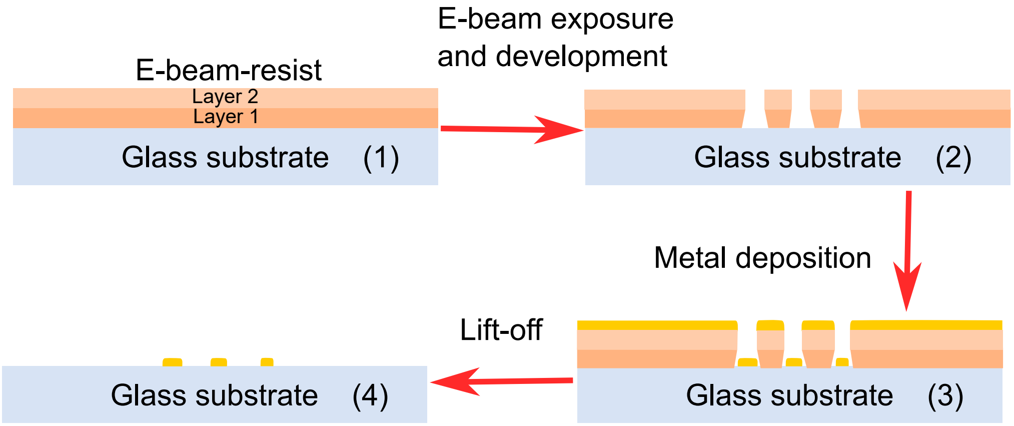

Figure 2.1.: *Sketch of the fabrication of the wide gap gold junctions showing the sample after each fabrication step. First a double layer of PMMA is deposited on a clean glass cover slip (1). Then the resist is patterned by an e-beam exposure and a development step, which removes the exposed parts (2), leaving a negative of the desired structures. A thin layer of titanium (2 nm) and gold (20 nm) is evaporated on the sample (3) and in the end the remaining resist is removed leaving the sample with the designed structures, (4).*

Cleaning of samples All samples are fabricated on top of standard square glass cover slips of 22 mm length and a thickness of 170 μm. This allows us to use a high NA (1.49) oil immersion objective in our measurements.

I clean the substrates by immersing them first inside a Decon water solution for 10 minutes inside an ultrasonicator, to remove a thin organic layer protecting the glass cover slips. Next, they are put three times in de-ionized water for a total of 10 minutes to remove the decon soap. Finally they are inserted 10 min in acetone, 10 min in isopropanol and then dried using nitrogen gun. Usually an additional step of 3-5 min of oxygen plasma cleaning at medium power is performed.

E-beam lithography To define the gap junction design, an electron beam lithography step followed by a thin layer metal deposition is performed. The process is illustrated in Figure 2.1 in steps (1) and (2). First a double layer of

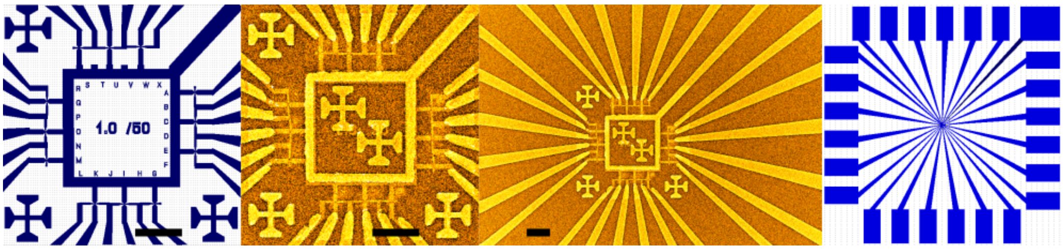

Figure 2.2.: *On the left e-beam design of the devices, the size of the crosses is* 20 µm. *In the middle left and right SEM images (false color) of the fabricated structures showing both the e-beam structures and the reaching contact electrodes. The two crosses in the center are added in the UV lithography step, overshadowing the central e-beam writing. On the right UV mask of the contact electrodes. The size of the whole UV structures is 21 mm x 21 mm. The (black) scalebar on the three left figures indicates* 20 µm.

PMMA (50K and 200K) is spin coated on a clean glass coverslip. To make the sample conductive for the e-beam exposure I also add a thin layer of Electra 92 (Allresist, AR-PC 5090.02). The design, an example is shown in Figure 2.2 on the left, is patterned by e-beam exposure and the subsequent development step onto the sample. This creates a mask for the metal deposition. The double layer of PMMA leads to an undercut.

Metal deposition In the next step a thin layer of gold is deposited. I typically deposit first 1-2 nm of titanium or chromium as an adhesion layer and then 30 to 50 nm of gold. As sketched in Figure 2.1 step (3), the undercut avoids that the metal is deposited onto the resist side walls, this facilitates the lift-off process. For the lift-off process the sample is put into a solution of the remover AR 600-71 (Allresist) or acetone, which removes the exposed resist from the sample. This leaves then only the designed gold structures.

UV-lithography To electrically connect the gold junctions, an additional step of UV-lithography is performed. The fabrication work flow is similar to e-beam lithography illustrated in Figure 2.1, except that the e-beam patterning is replaced by an UV exposure using a hard mask.
The sample is again cleaned with acetone, isopropanol and an oxygen plasma, although at lower ultrasonication and plasma intensities to preserve the e-beam defined structures. Then a negative UV-resist is spin coated (AZnLOF from MicroChemicals), the sample is exposed, post baked and developed.

I then deposit 10 nm of chromium and 25 nm of gold and perform again a liftoff to obtain the electrodes. This thicker metal deposition allows to perform wire-bonding onto the sample.
A mask with a standardized electrode design is used, shown on Figure 2.2 right. The electrodes are then connected either by wire-bonding to a PCB board or directly contacted with a pair of tungsten tips. Electrode structures could also be patterned by using e-beam lithography directly, as it is done for the samples provided by our collaborators from ETH Zurich.

2.2. Devices

Two types of devices are studied in this chapter: gap junctions exposed to air and gap junctions embedded in a dielectric matrix of sputtered SiO_2. Initially, the experiments were carried out only on junctions exposed to air. To quantify or exclude the contribution from the room atmosphere, such as moisture or other contaminants, I decided to also investigate structures fully embedded in SiO_2.

2.2.1. Gold gaps in air

The structure of the wide-gap gold junctions in air is shown in Figure 2.3 a). The junctions consist of a sharp planar gold tip (labeled control electrode in the figure) separated by 20 nm to 80 nm from a gold nanowire. In all the experiments presented here the voltage (positive or negative) is applied on the control electrode whereas the constriction is at ground potential.
The geometry of these structures has not any intricate design considerations. Initially, the control electrodes were intended to simply generate an electrostatic field on the nanowire constriction. The observation of both light emission and current transport from these gaps, however, lead us to reconsider our experiments focusing instead to understand the mechanism behind these unexpected findings.

2.2.2. Gold gaps in SiO_2

The sample containing wide gaps embedded in SiO_2 was kindly provided by B. Cheng and collaborators from ETH Zurich. As shown in Figure 2.3 b) and c), the devices consist of two small separated triangles forming a bow tie antenna (seen in the center of Figure 2.3 c)), connected electrically to larger electrodes.

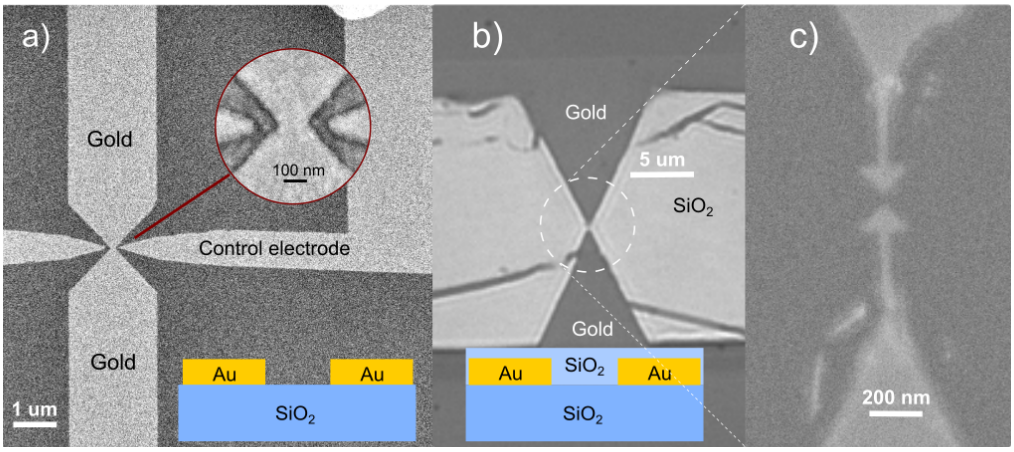

Figure 2.3.: *Overview of the fabricated wide-gap gold junctions in air (a) and embedded into* SiO_2 *(b,c). (a) A scanning electron microscope image of a fabricated wide gold gap junction in air is shown. The gap is located between a small gold constriction separated typically by 20 to 80 nm from the counter electrodes, shown in the inset. (b) Bright field image of a wide-gap gold junction embedded in* SiO_2*, (c) SEM image of the tip structure, revealing the bow-tie antenna design of the electrodes. The coloured sketches in a) and b) show the cross sections of both structures.*

The purpose of the antenna is to increase the collection efficiency and enhance the light emission, as demonstrated in [21,35,38] in the context of inelastic electron tunneling.

The gap size varies across the sample for different junctions. For the measurements presented here only junctions with gap distances of 20 nm were investigated.

The fabrication of the sample from ETH Zürich is slightly different than to what is presented above in Section 2.1. After cleaning of the glass cover slip, a metal layer (1 nm chromium, 50 nm gold) is deposited. Using e-beam lithography, a mask is patterned on top and part of the metal is removed through argon plasma etching. Then a 60 nm thick layer of SiO_2 is added on top by RF-sputtering. To electrically contact the gaps, the SiO_2 located on top of the electrodes is removed by dry reactive ion etching using CHF_3.

2.3. Current transport

As hinted in the introduction, the current behavior of a wide-gap gold junction is far from being simple. The wide-gap gold junctions do not show a monotonous current voltage relation, as for example a standard tunnel junction, because the wide-gap junction's conductance evolves dynamically under an applied voltage.

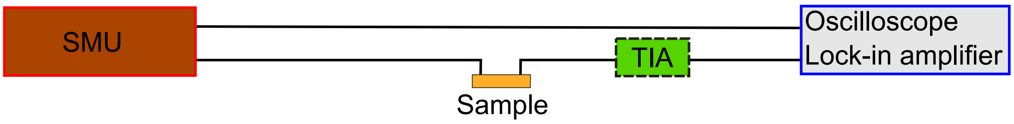

Figure 2.4.: *Sketch of the elements to electrically characterize the gold gap junctions. The voltage source, in this case a source measurement unit (SMU), is connected to the junction. The current is typically measured by an additional device, here a trans-impedance amplifier (TIA), and then displayed on an oscilloscope. To allow a synchronization of the the current detection with the excitation the same voltage sequence is also sent to the oscilloscope. Sometimes the TIA is replaced by a high speed active probe with an input resistance of* 1.25 MΩ.

This is seen in voltage sweeps using a source measurement unit (SMU, Keithley 4200A-SCS). The SMU delivers a predefined voltage sequence (in this case a voltage ramp) and measures at the same time the (averaged) current. This allows the SMU to lower its output voltage whenever the current is too high and protect the device under test. The electrical connections of such a measurement are shown in Figure 2.4. Typically a transimpedance amplifier (FEMTO DHPCA-100) with variable gain (10^2 to 10^8) is added to measure the current with a higher time resolution as shown below in Figure 2.13 (minimal bandwidth of 220 kHz)). The measurement is displayed in real time on an oscilloscope. The TIA is replaced for pulsed measurements on the gold junctions embedded in SiO_2 by a low noise high speed (26 GHz) active probe with an input resistance of 1.25 MΩ (Model 35, GGB Industries), for example in Figure 2.12.

Such a voltage sweep is shown in Figure 2.5, displaying the current measured by the SMU in function of the applied voltage. At the beginning of the voltage sweep (arrow 1), almost no current flows through the junction, as expected from the wide dielectric spacer. The current increases only slightly with the applied voltage. The junction is in a high resistance state (HRS), with a resistance in the order of 10^{10} Ω or higher. At a given threshold voltage V_{thr}, around 9 V in

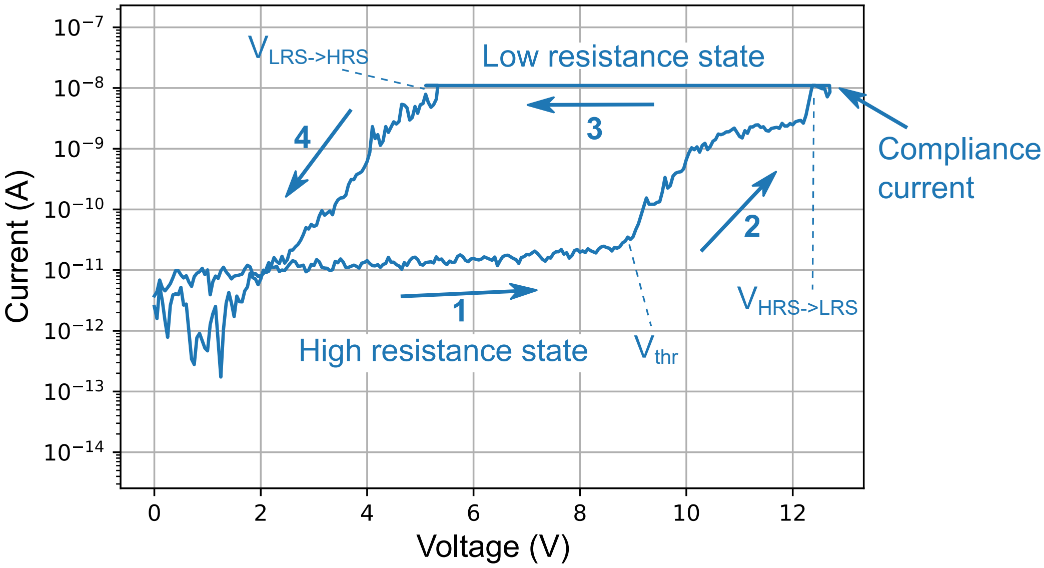

Figure 2.5.: *Measured current versus applied bias for a voltage sweep on a wide-gap gold junction in air. The arrows indicate time evolution of the sweep. At the beginning (1) the device is a high resistance state (HRS), with almost no current observed up to 9 V. Starting from 9 V, indicated by* V_{thr}*, a fast increase in the current over several order of magnitudes is observed (2), the junction becomes more and more conductive. At 12.5 V the current reaches the compliance limit, (*$V_{HRS \rightarrow LRS}$*), the applied bias is thus regulated by the SMU to not exceed the current limit. The regulation remains active during the backward sweep as long as the junction has a low resistance, down to values of* $V_{LRS \rightarrow HRS}$ equal to *5 V, (3). For lower applied biases the current decreases, the device gradually settles again into a high resistive state (4).*

Figure 2.5, the current increases however rapidly over several orders of magnitude with an increment of only few volts of the applied voltage (2); the device becomes more and more conductive and reaches a low resistive state (LRS).
Around a voltage of 12.5 V, indicated in Figure 2.5 by $V_{HRS \rightarrow LRS}$, the current reaches the compliance limit of 11 nA set on the SMU by the user. This compliance current protects the junction by limiting the dissipated electrical power. When reaching the compliance current, the SMU automatically adapts its output voltage in order to not exceed the compliance current on the device. The compliance current is reached also in the backward sweep for voltages down to

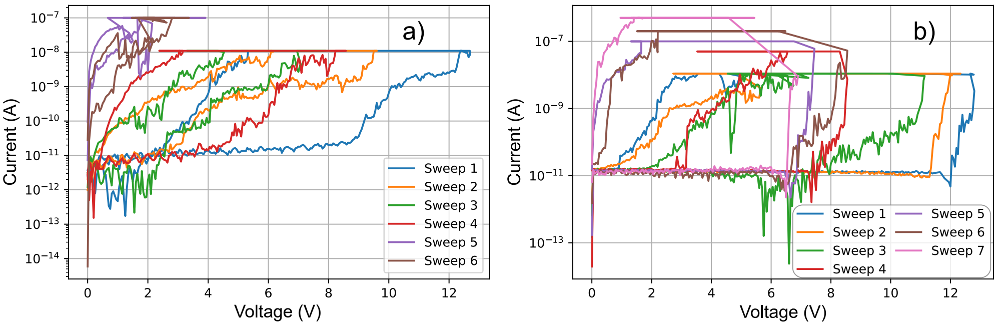

Figure 2.6.: *Repeated voltage sweeps for a wide-gap junction in air a) and in* SiO_2 *b). The junction of a) is the same junction shown in Figure 2.5 with the blue curve being identical to the curve shown in Figure 2.5. In both figures, the threshold voltage required for initiating the resistive switch is reached at lower applied bias over repeated voltage cycles. The compliance current was also manually increased between sweeps.*

5 V (3), a voltage where only 20 pA was measured during the upward sweep. During the backward voltage sweep at about 5 V, indicated in the figure with $V_{LRS\rightarrow HRS}$, the current decreases and the device undergoes a resistive switch back to HRS, (4).

For successive voltage sweeps applied on the same junction the threshold voltage V_{thr} and the compliance current are reached at lower voltages, as illustrated in Figure 2.6 a). As the device switches to the LRS at lower voltages, a higher compliance current can be set without destroying the device. The device could be operated safely with a compliance current as high as 1 µA.

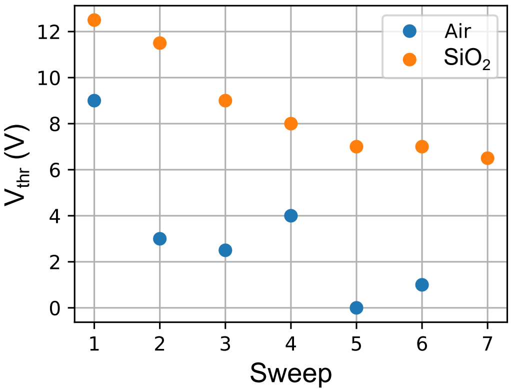

Figure 2.7.: *The evolution of* V_{thr} *over repeated voltage sweeps of Figure 2.6.*

This behavior is not particular to the junction in air but is also observed when embedded in SiO_2. For instance, Figure 2.6 b) shows consecutive voltage sweeps for a junction embedded in SiO_2. The threshold of resistive switching also reduces with sweep order.

The evolution of V_{thr} over repeated voltage sweeps is plotted in Figure 2.7 for both junctions and confirms the

decrease of V_{thr} over repeated voltage
sweeps. The behavior and reaction of the wide-gap junction to electrical bias is thus changed and set by the history of previously applied voltages. Otherwise formulated, the wide gap junctions retain some memory of the applied voltage and currents.

Both gold gap junctions show thus the same (qualitative) voltage-current behavior with a consistent switching between two resistive states. Although for the junction embedded in SiO_2, the initial voltages V_{thr} are higher, after multiple sweeps one is able to reach the same and even higher compliance current limits as for the gold gap junction in air.

In the following I will discuss the underlying mechanism responsible for the switching in the wide-gap gold junctions.

2.3.1. Dielectric breakdown in SiO_2

The current behavior of the wide-gap gold junctions can be understood from the well-studied phenomenon of dielectric breakdown in SiO_2 [56–58]. Even though part of the gaps are exposed to air, the electron transport in this case may occur through the SiO_2 substrate and air-SiO_2 interface. Here, I will follow in large part the description of [56] discussing the electrically induced degradation of thin SiO_2 layers. The influence of moisture and other surface contaminations is here neglected.

2.3.1.1. Pristine junction and low current: Fowler-Nordheim tunneling

In the beginning of the voltage sweep, when the junction is in a high resistance state (HRS), electron conduction occurs mainly via Fowler-Nordheim tunneling [56]. This mechanism is sketched in Figure 2.8.

Fowler-Nordheim tunneling is essentially a three step process. In the first step, electrons from the source electrode (negatively biased gold electrode) tunnel to the conduction band of SiO_2, as indicated by (1) in Figure 2.8. This tunneling process is limited by the barrier height between gold and SiO_2 of 4.1 eV [60] and the electric field strength across the junction and gives rise to a tunneling current (density) J_{FN} [56]:

$$J_{\mathrm{FN}} = \frac{e^3 E^2}{16\pi^2 \phi_{\mathrm{b}}} \frac{m_e}{m_{\mathrm{ox}}} \exp\left(-\frac{4}{3} \frac{\sqrt{2 m_{\mathrm{ox}}}}{e\hbar} \frac{\phi_{\mathrm{b}}^{3/2}}{E} \right) \tag{2.1}$$

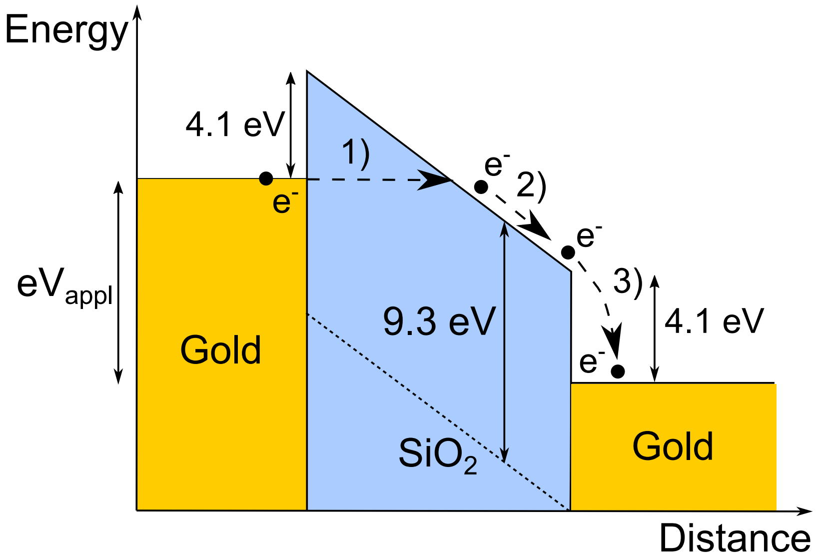

Figure 2.8.: *Sketch of Fowler Nordheim tunneling in a wide-gap gold junction from the source electrode (negative bias) through SiO_2 layer to the drain electrode. For the gold electrodes the thick lines indicate their Fermi energy, whereas in SiO_2 the thick line indicates the energy level of the conduction band. The dashed line marks the energy level of the valence band in SiO_2, separated by* 9.3 eV *from the conduction band [59]. In the first step, electrons tunnel from the source electrode to the conduction band of SiO_2 (1). Then these electrons move to the source electrode due to the applied electric field (2). The electrons enter the source electrode with an excess energy equal to the gold-SiO_2 barrier height* (4.1 eV) *which is dissipated locally.*

where E is the applied electric field, ϕ_b the gold-$\mathrm{SiO_2}$ barrier height, e the electron charge, m_e the electron mass in vacuum and m_ox the electron mass in the conduction band of $\mathrm{SiO_2}$.

The barrier height between gold and $\mathrm{SiO_2}$ is not only affected by the electrode material but also by the electrode shape, the temperature and interface charge traps [56]. The actual barrier height in our experiments is likely to be lower than 4.1 eV, as in similar structures, also conditioned by several voltage sweeps, barrier heights of 3.3 eV have been reported [61] .

Once the electrons have tunneled to the conduction band they are accelerated towards the drain electrode (positive bias) (2). Their maximum kinetic energy is however limited due to scattering of the electrons. According to [56] the kinetic energy remains below 1 eV, whereas [62] gives an upper limit of 4 eV at an applied electric field of 10 MV cm^{-1}. 10 MV cm^{-1} is typically an upper limit of the electric field observed at the $V_{LRS \rightarrow HRS}$ for the first sweep on a fresh junction in air.

Finally in the last step electrons are injected into the drain electrode (3). This excess energy of the tunneling electrons is dissipated locally leading to bond breaking in SiO_2 and causing the creation of localized defect states close to the drain electrode [56]. The same mechanism described above for electron transport can also apply to holes (the absence of an electron in otherwise occupied energies). However as the barrier height is greater for holes [56] their contribution is less important.

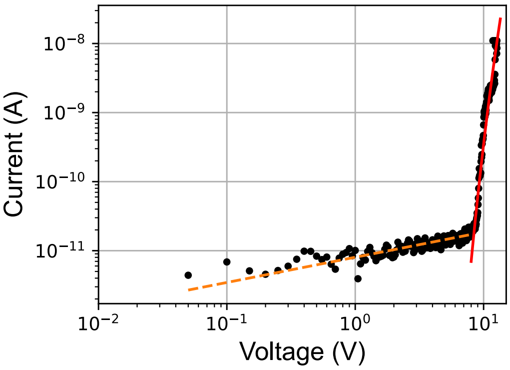

Figure 2.9.: *The HRS part of the voltage sweep of Figure 2.5 in a double logarithmic plot (black points). In orange the estimated $V^{0.3}$ current dependence, in red the fit of the Fowler-Nordheim tunneling current.*

The current voltage relation of Fowler Nordheim tunneling (equation 2.1) is not observed in the beginning of the voltage sweeps of Figure 2.6. As shown in Figure 2.9 for the first sweep of Figure 2.6 a), the current I initially observes approximately a $I \propto V^{0.3}$ dependence, instead of the exponential behavior predicted by equation 2.1. Such a current voltage relationship is observed consistently for most of the other sweeps in Fig. 2.6 a) and could be due to the presence of moisture and surface contaminants. However once the threshold voltage V_{thr} is reached, the subsequent steep current increase follows the Fowler Nordheim equation. The fit of eq. 2.1 is shown in Fig. 2.9 by the red dashed line. This overlap is only observed during the initial (first) voltage sweep.

For the junctions embedded in SiO_2, see Fig. 2.6 b), the current remains below measurement noise until the threshold voltage V_{thr} is reached. The subsequent current increase occurs over a few measurements steps. This makes it difficult to estimate whether this current increase similarly obeys the Fowler-Nordheim equation.

2.3.1.2. Trap generation and trap assisted tunneling

The energy dissipated by the electrons in the Fowler-Nordheim tunneling causes defect and charge trap generation inside the SiO_2 layer. This modifies eventually the transport mechanism through the wide-gap junction [56,58,63–65] and leads to the observed hysteresis.

The creation of defects and charge traps is predominant at the drain electrode [56], as there each electron releases the energy of the SiO_2 gold barrier height, about 4 eV.

Due to the applied electric field these newly created traps are likely to be charged positively, therefore attracting electrons, which therein dissipate their energy. This leads to an accumulation of charge traps growing from the drain electrode towards the source electrode. This decreases thus the effective thickness of the insulating layer. Therefore the same voltage leads to a higher electric field and thus to a higher current [56].

Once a continuity of charge traps reaches the source electrode a conduction path for the electrons is created, leading to a breakdown of the SiO_2, causing an abrupt release of energy and destroying the device [56].

As the energy released by a single electron at the injection into the drain electrode is more or less the same irrespective of the applied electric field, the breakdown mechanism is independent of the applied voltage but only depends on the number of injected electrons and their relaxation kinetics [56]. This would explain why in the experiments I typically observe a higher V_{thr} for faster voltage sweeps.

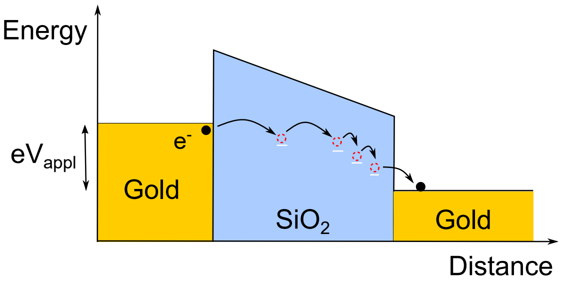

Figure 2.10.: *Sketch showing trap-assisted tunneling in wide-gap gold junctions. Electrons from the source electrode (left gold electrode), tunnel between different trap states (white line) created within the SiO_2 layer to the drain electrode.*

Charge traps can also be created well within the SiO_2 layer due to the excess energy of fast electrons within the conduction band, or already be present due to intrinsic defects in the SiO_2 [56].

Creation of electron charge traps leads to an additional transport pathway for electrical current called trap-assisted tunneling [65–67], where electrons hop between different localized trap states from the source to the drain electrode. This is depicted in Figure 2.10, where the localized electron energy states (or

traps) inside the dielectric are shown with white lines.
The exact nature of the charge traps is still debated [67]. In [64], charge traps are associated to oxygen vacancy defects in SiO_2. In [67], an influence of the gas atmosphere on the defect creation has been shown, helping the reduction and removal of oxygen, and the creation of Si-H bonds. This is consistent with the increase in V_{thr} in [61] for very similar wide gold gap junctions in vacuum compared to air, but does not explain the switching for junctions embedded in SiO_2. The switching back from a high resistance state to a low resistance state is attributed in [67] to an electro-chemical induced reorganization of the charge trap state.

2.3.1.3. Current fluctuations in trap-assisted tunneling

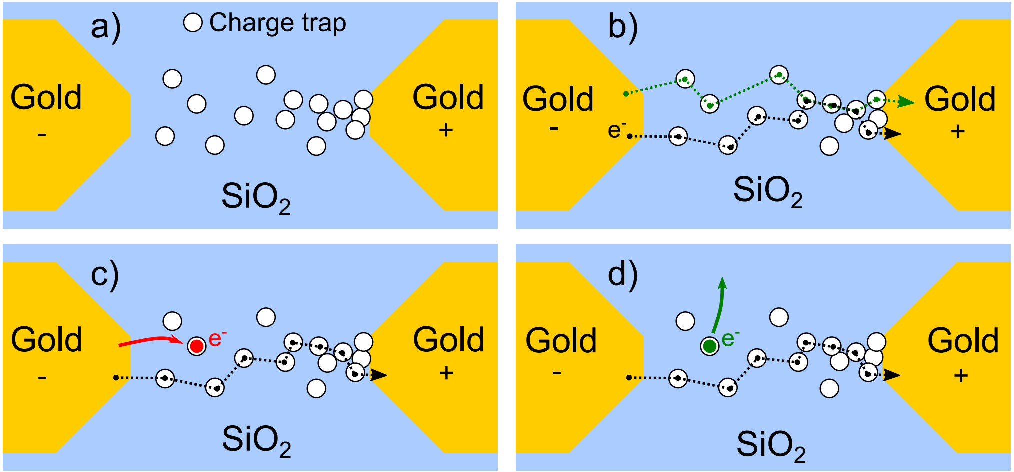

Figure 2.11.: *Conductance variations in trap-assisted tunneling. In a) the simplistic (spatial) charge trap distribution in the SiO_2 layer between the source electrode (left, negative bias), and the drain electrode (on the right). In b) two possible electron hopping paths (green and black) are depicted (among many more). In c), the trapping of an electron in a trap, indicated in red, inhibits the green hopping path shown in b). The conductance of the junction thus drops, although electron transport through the black path is still possible. d), the release of the electron from the trap, reopens the green conduction path of b). Compared to c) the conductance of the junction increases.*

Together with the increase of current flowing through the gap, an increase in current noise as well as random telegraph noise [63, 69–71] are also observed.
This current noise is associated to electron capture in charge traps [69, 70, 72], which causes a conductance variation in the trap-assisted tunneling of electrons. In trap-assisted tunneling, the presence of multiple defects inside SiO_2 allows electron conduction inside the dielectric by electron tunneling from defect to defect state. Typically, electron hopping through different defects paths are possible, as illustrated in Figure 2.11 a) and b).
Once an electron is trapped at some site, the energy required to accept a second electron is raised both inside the same trap and, due to its electric field, also for nearby traps. This effectively closes some of the conductance paths between both electrodes, see Figure 2.11 c) and leads to a drop in the conductance of the junction.
Conversely, releasing an electron from a charge trap, Figure 2.11 d), opens up new conduction paths and results therefore in an increased conductance.
All these cause observable fluctuations of the current. The magnitude of these current changes does not indicate the number of electrons trapped or released but rather the number of alternative current hopping pathways. Still, large con-

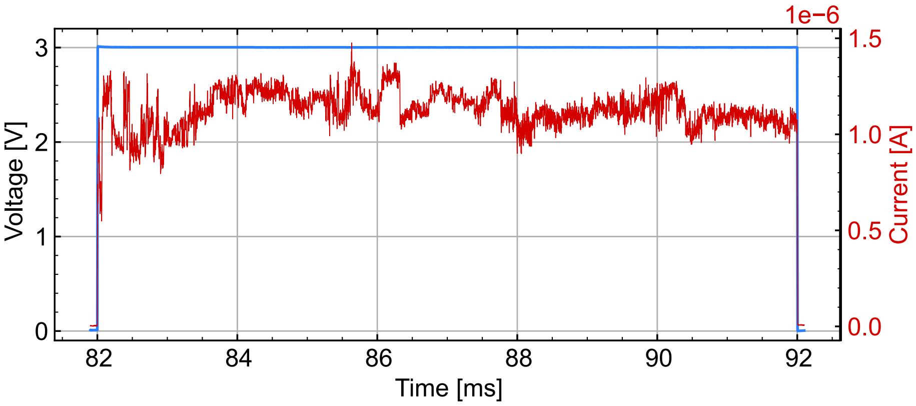

Figure 2.12.: *Current (red) from a wide-gap junction excited by 3 V, 10 ms pulses (blue) using an arbitrary wave form generator (AWG), measured using a high speed active probe having* 1.25 MΩ *input resistance. The junction switches in the beginning of the applied pulse to a low resistance state. In the current one clearly distinguishes several discrete conductance jumps, seen for example between 82 ms and 83 ms or at 86 ms, together with faster and smaller superposed current oscillations.*

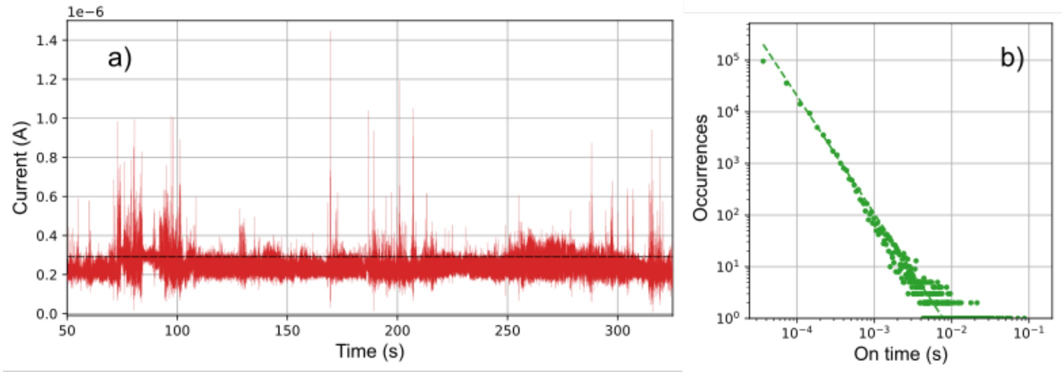

Figure 2.13.: *In a), the current measured (using a TIA) for a wide-gap gold junction in air in series with* 11 MΩ *for a total applied voltage of 4 V. The junction is in a low resistance state, the current shows a constant base of about* 200 nA*. Additionally, short current spikes are seen. The dashed black line indicates the threshold for the "on time" analysis shown in b). In b) the occurrences of different on-times are shown in a loglog plot. The occurrences follow a straight line indicative of a power law. The fit (dashed line) shows a negative power exponent of -2.28, similar to what is reported in [68]. The power exponent slightly shifts by changing the threshold (within some limits), but a power law is always clearly visible.*

ductance variations occur less compared to small conductance changes which are more frequent [70].

Such current noise and conductance fluctuations are observed in the measurements on the wide-gap gold junctions, both for junctions embedded in SiO_2 and exposed to air, as shown resp. in Figures 2.12 and 2.13 a).

In particular, the current shown in Figure 2.12 features several jumps between discrete states of current. These jumps can be clearly associated to the closing and reopening of conduction paths.

The current shown on longer time scales in Figure 2.13 a) displays current noise in the form of rather short spikes. These resemble the current traces reported in [68], where the current conduction of a single quantum dot was studied. These fluctuations are attributed to charge trapping into a surface state of the quantum dot, similarly shifting the internal energy levels and inhibiting the transport of the following electrons.

The current spikes in [68] are further analyzed by looking at the distribution of their duration. By choosing a suitable threshold, shown in our case by the dashed line in 2.13 a), one extracts the duration a current spike remains above this threshold, the ”on time” of the current. By plotting then the number of occurrences N for a given duration τ, a power law behavior was seen in [68]:

$$N(\tau) \propto \tau^{\alpha} \tag{2.2}$$

with exponents α for on (and off times) of $\alpha = -2.5$ (resp. $\alpha = -2.1$). In our case the current spikes are also distributed in a clear power law behavior of the occurrences with an exponent of $\alpha = -2.28$, as plotted in Figure 2.13 b). The observation of a similar power law in the wide-gap junction’s current corroborates thus electron trapping and the trap-assisted tunneling mechanism.

2.3.2. Electrode deformation and gold cluster migration

The current conduction in the wide-gap gold junctions is not only depending on the interaction with the SiO_2 matrix or interface discussed so far. The gold electrodes play also a role in the transport mechanism. As displayed in Figure 2.14, the wide-gap gold junctions exposed to air show a clear deformation of the drain electrode after being submitted to electrical stress. The presence of gold nano-particles growing towards the source electrode is observed in the SEM images taken after several voltage sweeps.[1] Similar electrode deformation and gold nano-particle migration was observed in [61] for gold gaps exposed to ambient atmosphere or placed in vacuum on a SiO_2 substrate, and in [73] for gold gaps in air on ZnO. Both papers attribute the resistance switching as a consequence of this gold migration. This gold migration is likely to contribute, together with the SiO_2 charge traps, to the current transport and resistance switching of the wide-gap gold junctions.

The diffusion of gold atoms into SiO_2 is nothing unexpected and new, as it has been already reported in 1966 [74, 75] after thermal annealing (200 °C) of gold films on top of SiO_2. The migration (for thermal annealing) is similarly favored by an applied electric field [76].

In parallel to drive the electron transport, the electric field causes also the creation of gold ions (Au^+ and Au^{3+}) at the drain electrode through oxidation of gold [48, 76–78]. These (positively) charged gold ions are then attracted by the electric field towards the source electrode [76, 79] and diffuse into SiO_2. These gold ions may reduce at oxygen vacancies inside SiO_2, as do silver ions [80], leading to a local formation of small gold clusters. In general a complex interaction

---

[1] Wide-gap gold junctions embedded in SiO_2 were not investigated with SEM images, due to lack of time of this thesis’ author.

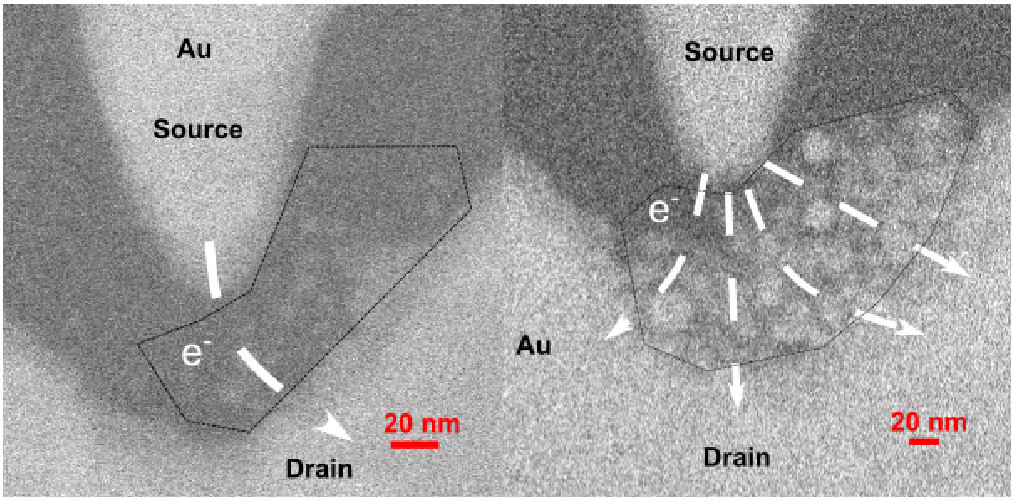

Figure 2.14.: *SEM images of two wide gold gap junctions in air after electrical activation, showing drain electrode deformation and small gold particles diffusing towards the source electrode. The area of deformation is enclosed in both figures by a dashed dark line.*

between gold ion migration and diffusion through the SiO_2 is expected [76].
The presence of gold ions or clusters provides additional localized electron states [48] to the trap and defect states of SiO_2, allowing once again trap-assisted tunneling as discussed above.
Charge-induced resistance increase (Coulomb blockade) has indeed been observed in devices relying on electron hopping from source to drain electrodes via a small gold particle. When the particle is charged (an electron is trapped) the conductance of such a device is decreased [81–84].

Differences between junctions in air and embedded in SiO_2 Although both type of junctions show similar current transport and noise, the involved SiO_2 defects or gold clusters are not necessarily the same. The SiO_2-air interface defects occurring in the junctions exposed to air most likely differ from the bulk defects created in thermally evaporated SiO_2. Similarly, the growth and displacement of gold nanoclusters and ions is hindered by the presence of the dielectric SiO_2, whereas the gold clusters on the SiO_2-air interface are not limited by the same constraint.
From the current measurements and analyses performed here it is however dif-

ficult to distinguish between the different defects present. The main difference observed in the measurements is that the junctions embedded in SiO_2 show a higher V_{thr} for the first sweeps on a pristine device. This is only indicative, as the initial V_{thr} depends also on the initial gap size and geometry of the electrodes. Additionally, V_{thr} can reach similar values regardless of the dielectric environment after successive sweeps.

2.4. Light emission during voltage sweeps

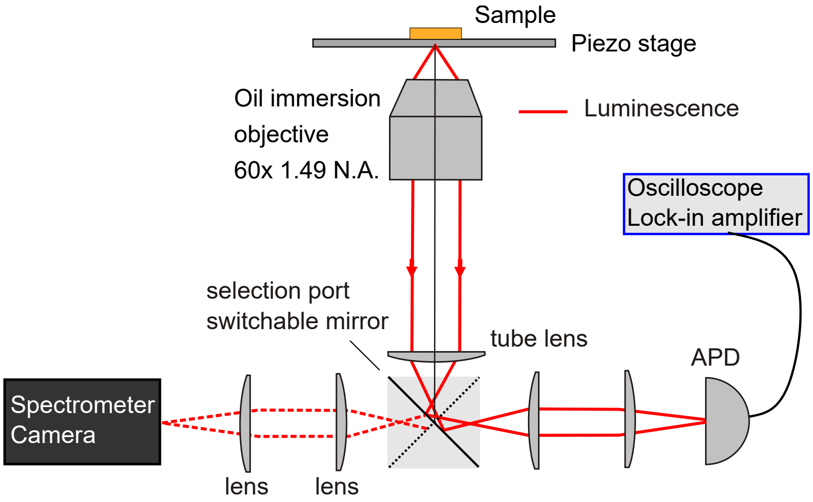

Figure 2.15.: *Sketch of the optical setup used to collected the light emission from the wide gap junctions. The sample is placed on an inverted microscope. A piezo stage allows precise positioning of the desired gap. The light is collected using an oil immersion objective and then sent to a spectrometer, camera or an avalanche photodiode (APD). The latter is connected to the same oscilloscope used to monitor the electrical signals in Fig. 2.4 and allows to observe the evolution of the photon counts in real time.*

Let us now turn to the electrically induced light emission from the wide-gap gold junctions. To efficiently collect this radiation the samples are placed on an inverted microscope. A piezo-electric translation stage allows precise position of the gaps. As sketched in Figure 2.15, with a high NA oil immersion objective (Nikon, 60x, NA 1.49) the light is captured and then sent onto different optical detectors, such as a camera (i-Kon M, Andor Technology), a spectrometer

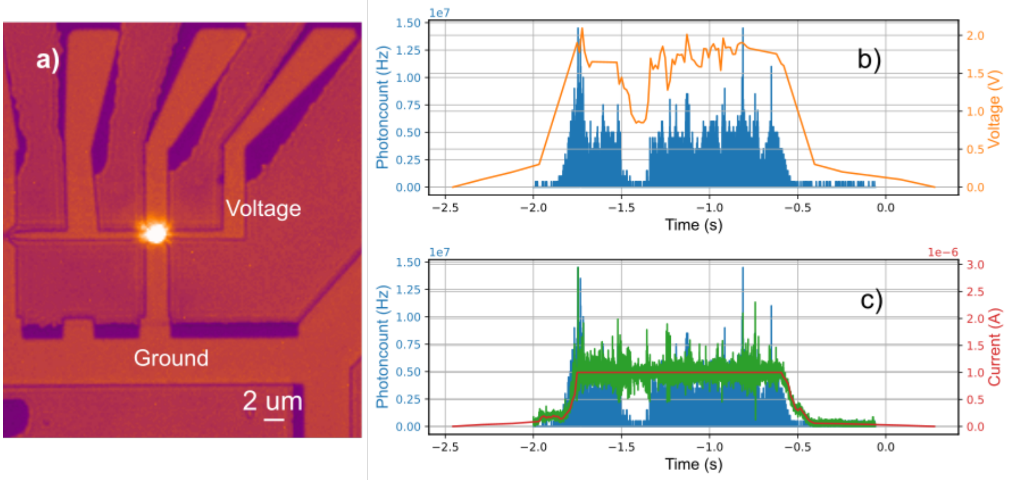

Figure 2.16.: *a) Bright field camera image (false color scale), depicting the light emission from a wide-gap gold junction in air during a voltage sweep. The two graphs (b) and (c) display such a voltage sweep in time. In (b) the applied voltage by the SMU (orange), in (c) the current, in red as measured by the SMU, in green measured with the TIA are plotted. In both graphs the blue curves indicate the detected photon counts.*

(Shamrock 300i, camera Newton, Andor) and avalanche photodiode (APD) (Excelitas SPCM-AQRH, 350 ps time resolution), by choosing the right microscope output port.

Light emission is observed during voltage sweeps. As shown in the camera image of Figure 2.16 a) this light originates from the gap region. Figure 2.16 b) and c) plot the time trace of such a voltage sweep, showing the detected photon counts (by the APD) in blue. In addition, the plot b) displays the voltage applied by the SMU (orange) whereas the plot in c) shows the current measured by the SMU (red) and by the TIA (green). Clearly the SMU measures the current over longer time bins then the TIA. The latter has a higher time resolution, but this comes at the price of more noise in the measurement. This is particularly striking when reaching the compliance current set at 1 µA: for example in Figure 2.16 c) the TIA registers large current spikes with values above 2 µA, but the SMU, expectedly, indicates a constant current of 1 µA.

From both time traces one can make already a few remarks about the photon radiation. The start of photon emission clearly coincides with the rise of current (see 2.16 c)). It seems thus that photon are released from the gap as soon as a low resistance state of the junction is reached. Indeed photons are continuously

registered during the whole time the current is at kept at the compliance limit, except for a drop to zero at -1.5 s. The drop coincides with the decrease of the voltage below 1 V as observed in a). This decrease is imparted by the SMU to maintain the current at the compliance limit.
The dependence of the photon count rate on the applied bias becomes clearer if one extracts the average (over the whole measurement) photon count rates in function of the applied voltage. Such an analysis is shown in Fig. 2.17. This is particularly interesting as the current is independent of the applied voltage (due to the junction's resistance change) and fluctuates during most of the measurement around the compliance limit of 1 µA. The photon rate in Fig. 2.17 thus does not depend on the amount of electrons going through the gap but only on their potential energy set through the applied voltage.

As can be seen in Figure 2.17, below a threshold voltage of 1.1 V no photons are detected.
The steep raise in detected photon counts above 1.1 V is partially explained by the APD's detection efficiency (the gray curve in 2.17), as the APD detects photons with 1.5 eV energy more efficiently then photons at 1.2 eV. The increase of photon count rates implies also that a larger amount of photons is emitted into the APDs spectral detection range for higher voltages.
The threshold behavior with the detection limit of the APD naturally raises the following question: if the detection limit of the APD would be lowered to 0.5 eV, would one also observe an onset of photon counts at a voltage of 0.5 V?

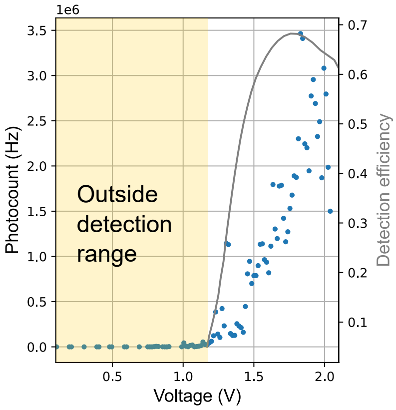

Figure 2.17.: *The normalized statistics of photon counts in function of applied bias extracted from 2.16 a). There is a clear voltage threshold for the photon counts at 1.1 V. This threshold coincides with the lower detection limit of the APD. The detection efficiency of the APD is shown in the gray curve.*

To confirm that the light activity is not due to surface contaminants but a shared property of the dielectric gap also the photon emission from embedded wide-gap Au junctions was measured. As illustrated in Figure 2.18 light is also detected in this case. Compared to Figure 2.16, the compliance current is 20 times lower, with 50 nA instead of 1 µA, and the applied voltage is roughly the

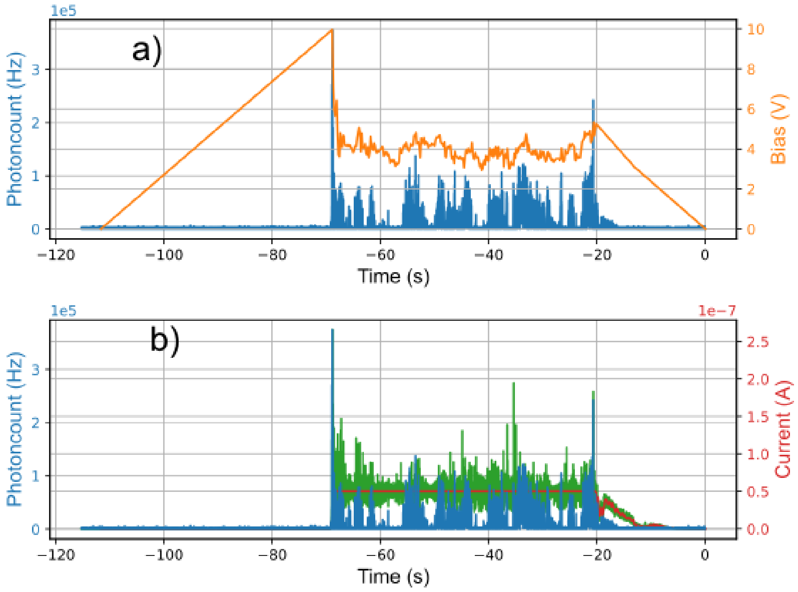

Figure 2.18.: *Light emission during a voltage sweep as in Figure 2.16 for a gap embedded in* SiO_2*. In (a) the applied voltage by the SMU (orange), in (b) the current, in red as measured by the SMU and in green as measured by the TIA. In both graphs the blue curves indicate the detected the photon counts.*

double. The photon counts are about 20 to 100 times lower, which is partially expected as less current flows in the device. The photon appear to arrive in bursts, seemingly correlated with current peaks and fluctuations recorded in the TIA measurement (green curve of Fig. 2.18 b)). Such a relation between photon emission and current fluctuations will be studied more in detail in 2.7. But overall, both devices show a very similar emission behavior.

2.5. Light emission mechanisms

To explain the light emission in the wide-gap junctions, several hypotheses can be considered. Here I will discuss the most plausible ones which I group here into two categories.

The first hypothesis considers on an inelastic electron process [31, 85] which includes Fowler-Nordheim tunneling [56, 86, 87]. The second hypothesis explains the radiation by an electroluminescence mechanism stemming either from luminescent centers within the SiO_2 matrix itself [88–91] or from small gold clusters [92], which, as shown earlier, migrate into the dielectric matrix.

2.5.1. Light emission by inelastic electron tunneling

Light emission by inelastic tunneling was described in 1976 [31]. Quantum mechanics allows particles to cross regions where classically it would be energetically forbidden. This is called tunneling and was previously encountered in the discussion about Fowler-Nordheim tunneling. For voltages smaller than the metal gold barrier height and for smaller thicknesses (below 5 nm) electrons may tunnel directly from source electrode to drain electrode, as illustrated in Figure 2.19.

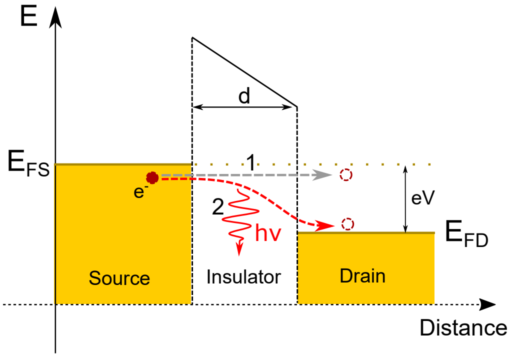

Figure 2.19.: *Elastic and inelastic electron tunneling for a tunnel junction. The yellow areas show the occupied energy states. The energy offset of eV, is given by V the applied voltage difference on the junction. E_{FS}, E_{FD} are resp. the Fermi energies of the source and drain. The conduction band energy of the insulator is shown in black. An electron may flow from the source to drain either by elastic tunneling (gray dotted arrow (1)) or inelastic tunneling (red dotted arrow, 2) accompanied in this case by a photon emission of energy hν.*

This tunneling process is either energy-conserved (elastic), in which case the electron has the same energy before and after the tunneling process, labeled (1) in Figure 2.19, or inelastic where the electron looses its energy in the tunneling process, for example by emitting a photon (2). This second process occurs typically in 1 out of 10^6 tunneled electrons [35].

Due to the Pauli exclusion principle, the maximum energy such an electron can loose is the energy difference between its initial energy and the lowest unoccupied electron state in the electrode. This gives a cut-off in the maximum emitted photon energy $h\nu$ as[2]:

$$h\nu \leq eV \qquad (2.3)$$

which is the signature of this process, and has been reported several times [31, 35].

For inelastic tunneling mechanism the

---

[2] Neglecting temperature broadening at 300 K.

relationship between the applied voltage and detected photon emission in Figure 2.17 is therefore evident. No photon can be emitted into the detection range for voltages below 1.1 V, whereas above the fraction increases steadily. Similar to direct electron tunneling, in Fowler-Nordheim tunneling (see Figure 2.8) light emission may also occur [56]. Either in the first tunneling step itself [86], which conditions the same cut-off as inelastic tunneling or during the injection step into the drain electrode (3, in Figure 2.8) [56]. In that case, the energy cut-off is given by the SiO_2-gold barrier height (about 4.1 eV [60]).

2.5.2. Electroluminescence

The second mechanism to consider is charge injection into luminescent centers distributed along the transport channels [93], as illustrated in Figure 2.20. During the transport of electrons through the SiO_2 dielectric some electrons may tunnel into the excited state of a luminescent center (either directly from the source electrode or from another defect in trap-assisted tunneling). These electrons then decay to the ground state of the luminescent center whilst emitting a photon. The electrons then continue their transport (at lower energies) through the SiO_2 to the drain electrode.

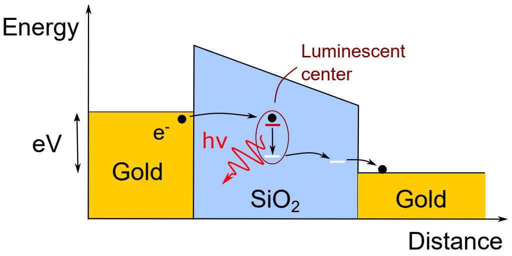

Figure 2.20.: *Light emission by electroluminescence. When crossing the SiO_2 matrix electrons can tunnel into an excited state of a luminescent center (red line). The decay to the ground state (white line) leads then to emission of a photon (curly red line). From the ground state the electrons may then continue to the drain electrode.*

Like for inelastic electron tunneling, the photon energies are limited by the energy difference between the highest occupied state in the source electrode and the lowest unoccupied state in the drain electrode, given by equation 2.3. However, the spectrum is also shaped by the discrete transitions of the luminescent defects, potentially showing up as discrete peaks. A higher applied voltage on the junction allows the electrons to explore a wide range energetically distributed traps. This typically leads to a higher photon count rate for higher voltages, consistent with what is observed in Figure 2.17.

Two kind of luminescent centers can be considered in the case of the wide-gap junctions. The first are luminescent defects within the SiO_2 matrix [90,91,94,95] such as silicon clusters. The second are small gold clusters [92, 96] already invoked in the current conduction. Both the gold and silicon clusters feature a size dependent emission wavelength between 400 nm to 1000 nm, and lifetimes in the order of a few ns [96–98].

2.6. Spectra

The analysis of photon count rate in function of the applied voltage shown in Figure 2.17 is not enough to distinguish between inelastic tunneling hypothesis and the electroluminescence mechanism presented above. To do so I measured therefore the spectral distribution of the emitted light, as will be presented in this section.

Surprisingly, the measured spectra are not constant but evolve over time, both for gaps in air and embedded in SiO_2. This is seen in time series of spectra acquired during voltage sweeps, shown in Figure 2.21. From these spectra one can already conclude a few things.

First of all, the spectra for both junctions present broad spectral peaks emitting into a range between 550 nm and 1000 nm. The latter value coincides with the detection limit of our silicon-based camera, it is therefore not a true emission limit (spectra are not corrected by the efficiency of the detector, see also Appendix C). The lower limit of 550 nm is more interesting as it is not instrument limited. It also cannot be explained by the quantum limit of inelastic tunneling of equation 2.3 as 550 nm wavelength corresponds to 2.26 eV photon energy. The maximum applied voltage in Fig. 2.21 b) is 8 V (equivalent to a cut-off at 155 nm) and during most of the sweep, the applied bias is greater than 4 V (310 nm cut-off) during the emission. One could associate the lower wavelength limit to the near-field interactions with the gold electrodes [99] shaping the emission of emitters as in optical antennas [20]. As gold starts to absorb light considerably for wavelengths below 516 nm [100] due to interband transitions, this may cause quenching (suppression) of the photon emission for shorter wavelengths.

Gold interband transitions can however not explain the fluctuating nature of the recorded spectra. For example the red and purple spectra (for both a) and d) of Fig. 2.21) change manifestly in amplitude and peak position.

In order to quantify the peak dynamics better, I fitted the observed peaks in the spectra with a gaussian curve $A \exp\left(-\frac{(\lambda-\lambda_0)^2}{2\Delta\lambda^2}\right)$, where λ_0 gives the center wavelength, $\Delta\lambda$ the width and A the amplitude of the peak, shown by the dashed lines in Figure 2.21. The spectra in Fig. 2.21 a) are fitted with two peaks, whereas the spectra Fig. 2.21 d) are well fitted with a single broad peak

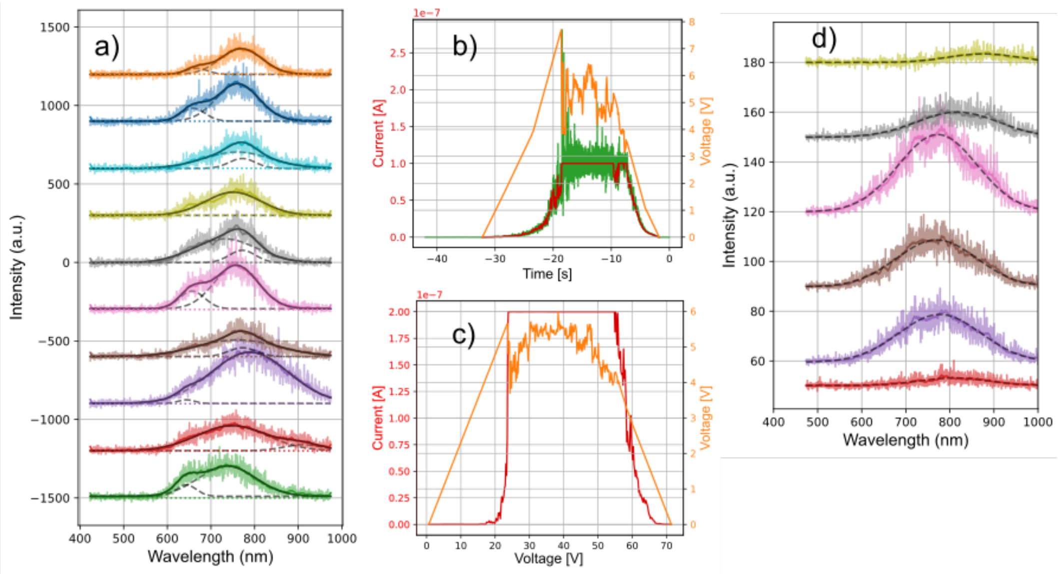

Figure 2.21.: *In a) a series of spectra (1 s integration time each) recorded successively during the same voltage sweep shown in b) on a wide-gap junction in air. The red curve indicates the current measured by the SMU, the green curve shows the current measured by the TIA and the applied bias is plotted in orange. For a better readability of the graph, each spectrum in a) is shown with an additional offset. For each spectrum also a running average (darker colour) is plotted. The spectra are ordered in time, with the first spectra at the bottom and the last on the top. The black line shows the sum of the two fitted gaussian peaks for each spectrum. The dashed black lines show the contribution of the individual peaks. Similarly in d) a time series of spectra (integration time 5 s) for a voltage sweep on a gold gap in* SiO_2 *is shown for the voltage sweep shown in c). Spectra in d) are fitted with a single gaussian peak (dashed black line).*

of roughly 100 nm linewidth. The center wavelength and the width of the peaks are shown for both series of spectra in Figure 2.22.

Both peaks for the junction in air, shown in Fig. 2.22 a), seem to fluctuate stochastically between the different spectra. There is however almost always a dominant peak around 730 nm to 790 nm. For the junctions in SiO_2, see Fig. 2.22 b), first a blue shift with a rather stable peak around 775 nm increasing in amplitude and then a red shift of the peak to 820 nm and beyond, together with a decreasing amplitude is observed. Whether this difference is due to a dif-

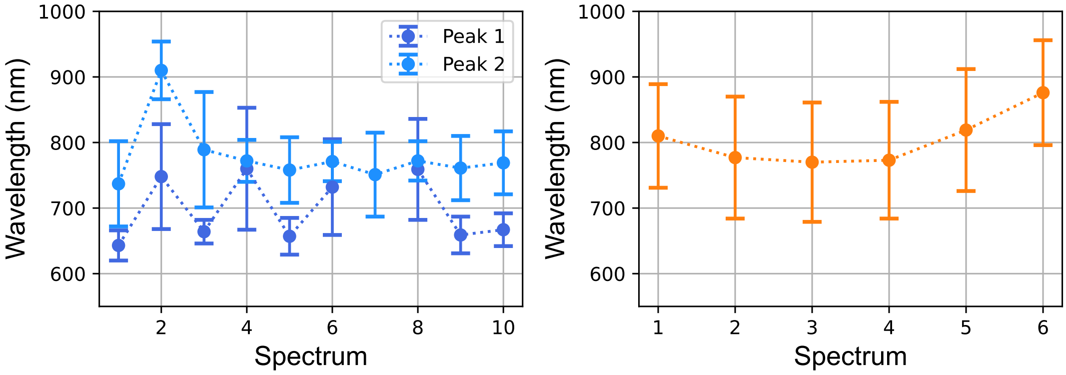

Figure 2.22.: *The center wavelength and width of the fitted peaks in the spectra of Fig. 2.21 (a,d), resp. in blue (a) for the junction in air and in orange (b) for the junction in* SiO_2*. The spectra are ordered (by number) from left to right corresponding from bottom to top in Figure 2.21.*

ferent integration time, the nature of emission process (i.e. different defects) or a difference in spectral stability would require additional measurements.

A change in the spectral emission over time is not only observed during voltage sweeps, but also for a constant voltage. This is shown in Figure 2.23 for three runs on the same junction in air. For each run a different voltage (9 V, 10 V and 13 V) was applied. As no compliance limit was set during these measurements a resistance in series of 100 MΩ was added to protect the junctions.

The spectral shape between the three series varies quite a bit. Within the same series however a certain continuity between the spectra is observed, as some peaks remain present in several successive spectra. Nevertheless, sometimes completely new peaks appear, as for example between the green and red spectrum in Fig 2.23 a) or the first and second spectrum in Fig 2.23 b).

Compared to the peaks of Figure 2.21 a), the spectra of Figure 2.23 feature narrower peaks, with typical widths below 30 nm as shown in Figure 2.24. Between subsequent spectra, in particular for the blue curves in Fig 2.24, one observes an almost constant peak position and peak width, with only the amplitude of the peaks varying over time.

This difference in peak width between Figures 2.21 a) and 2.23 could be due to the inhomogeneous broadening, the spectral superposition of several emitters. Depending on the electrical excitation, few (constant voltage) or more emitters (voltage sweep) contribute to the spectra. During the voltage sweep, the junction switches from HRS to LRS by forming and activating new conductance paths. The electrons therefore are forced to explore a wider range of energies to pass from the high resistance to the trap-assisted tunneling regime. This may

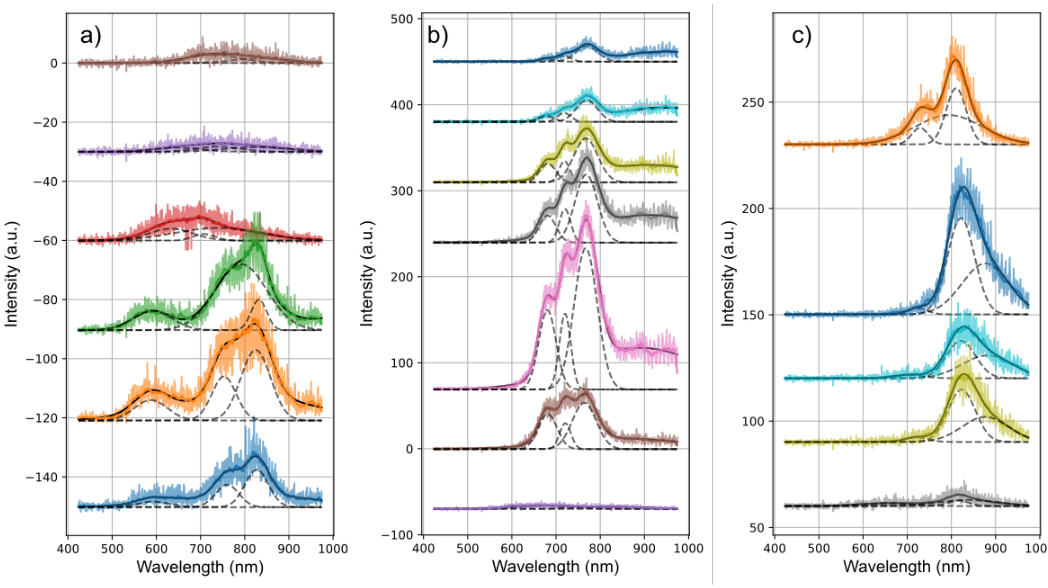

Figure 2.23.: *Three time series of spectra, integrated 5 s, for a constant applied voltage and ordered in time from bottom to top. In a) V=9 V, in b) V=10 V and in c) V=13 V, onto resistance* 100 MΩ *in series with a wide gold gap junction in air. As for Figure 2.21 the black curve shows the sum of multiple gaussian peaks, the dashed lines the individual peaks, the fitted width and position are found in Figure 2.24.*

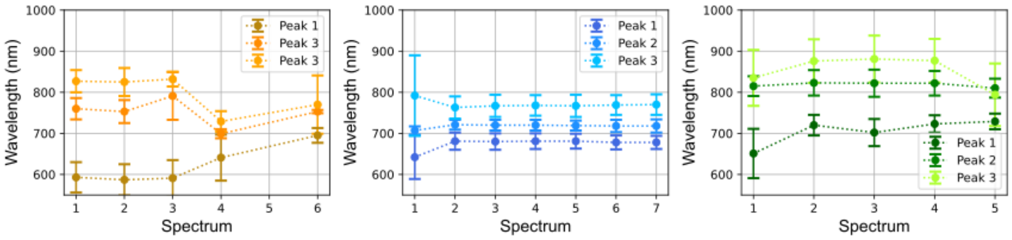

Figure 2.24.: *The center wavelength and width of the fitted peaks in the spectra of Fig. 2.23* (a,b,c) *resp. in orange, blue and green from left to right. The spectra are ordered in time (by number) from left to right.*

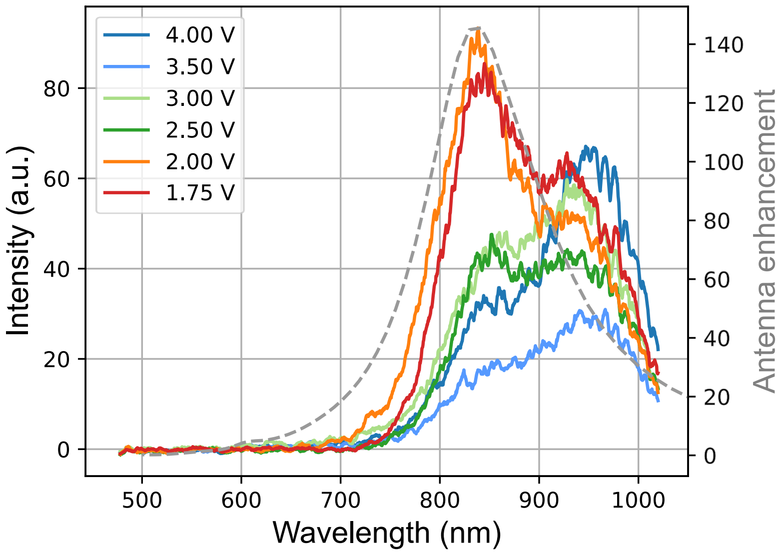

Figure 2.25.: *Spectra emitted by a gold gap embedded in SiO_2 excited by 10 ms voltage pulses, with an integration time of 2 s. The junction is in series with a resistance of* $1.25\,\mathrm{M\Omega}$. *For a better readability the fitted peaks are not shown in the figure, the peak position and width are reported in Figure 2.26. The dashed grey line shows the simulated antenna emission enhancement due to the structure of the electrodes, with the y-scale located on the right sight of the graph.*

lead to an excitation of multiple luminescent defects. For a constant voltage, the junction experiences only relatively small voltage variation and typically stays in a LRS during the whole acquisition time. The conduction path therefore is rather stable and in consequence accesses only the same few emission centers.

The spectra discussed so far were acquired continuously one after another while keeping the excitation or experiment running. This is not the case for the spectra of junction embedded in SiO_2 shown in Figure 2.25, where each spectrum was acquired for a single pulse train during 2 s with 10 ms pulses for a fixed voltage, varying between 1.75 V and 4 V. This different excitation for junctions in SiO_2 is due to data size constraints of time resolved current measurements with high temporal resolution

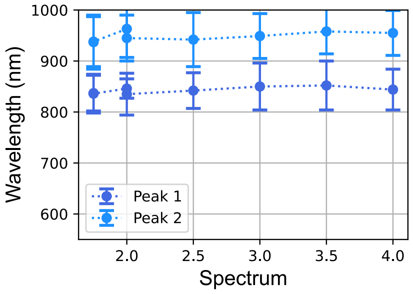

Figure 2.26.: *The center wavelength and width of the fitted peaks in the spectra of Fig. 2.25 The spectra are ordered by the applied pulse voltage during the acquisition.*

as discussed in section 2.7. To ensure a correspondence between the spectra and the time traces the same voltage pulses were kept during spectral acquisitions. The spectra display a consistent shorter wavelength cut-off at 700 nm and in almost all cases two peaks, with the center wavelength varying by less than 10 nm around 842 nm and typical peak with around 40 nm as shown in Figure 2.26. The second peak is again limited by the loss in detection efficiency towards longer wavelengths around 1000 nm and its position can therefore not be determined accurately. For this, it would be interesting to repeat the same measurements with a near infrared spectrometer operating in a longer wavelength range.

The position of the peak around 842 nm in Figure 2.25 nicely overlaps with the simulated emission enhancement of the electrodes (dashed line in the Figure).[3] The presence of spectral peaks is however independent of antenna resonances. For example the peak at 950 nm of Figure 2.25 has no equivalent antenna resonance. Also the peaks of Figure 2.21 d) are well outside the simulated antenna enhancement peak, as shown in Figure 2.27. The antenna shapes thus the emission of already present (possibly broadband) peaks.

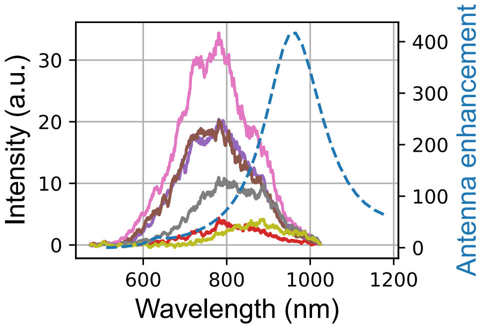

Figure 2.27.: *The simulated antenna enhancement for the device of Fig. 2.21 d) together with the measured spectra.*

Interpretation In light of the spectral features the inelastic electron tunneling hypothesis seems implausible. First, the emission features a wavelength limit lower than expected from the applied voltage and the kinetic energy given to the electrons. Second, the shift of this low wavelength limit shows no clear relationship to the applied voltage. Finally, the observation of discrete, appearing and disappearing peaks is hardly explained by inelastic tunneling.
The spectra rather suggest light emission through the electrically induced luminescence of some (or multiples) species inside the gap, as already postulated previously for the trap assisted tunneling current transport in 2.3. Two systems in particular are emitting in the observed spectral range: few atom

---

[3] The simulations were kindly provided by T. Zellweger from the Institute of electromagnetic fields. Details about the simulation method can be found in [101] and in the paper [102].

gold clusters [92, 96] and silicon rich nanoclusters within the SiO_2 substrate and matrix [91, 94, 103–105]. Their size dependence on the emission wavelength [90, 96, 103, 106] explains most of the observed spectral features. The presence of multiple peaks in the spectra is in this sense be a consequence of different emitting luminescent centers with different sizes. The broad peaks are caused by an inhomogenous superposition of several clusters with slightly different sizes and therefore emission wavelengths. The evolution of the amplitude or disappearance of some peaks is well explained by the luminescent centers diffusing in and out of the current path. Additionally, the growth or shrinking of both silicon and gold nanoclusters results into the observed spectral wandering of the peaks towards longer resp. shorter wavelengths.

2.7. Temporal dynamics and statistics of the light emission in wide-gap gold junctions

To characterize the electroluminescence of the junctions further, it is interesting to take a look again at the temporal dynamics of current and light. This will be treated in this section where two measurements in particular will be analyzed in greater detail. These two experiments are representative of the obtained results. The experiments in question are presented in Figure 2.28, showing the light emission of junction in air under constant bias, and in Figure 2.29, showing current and light emission of a wide gold gap junction embedded in SiO_2 excited with short voltage pulses.

Both measurements have a resistance in series acting as a voltage divider. For the junction in air a resistance of $R = 11\,\mathrm{M\Omega}$ is added to protect the device from destruction by limiting the electrical power on the junction. For the junction embedded in SiO_2 the $R = 1.25\,\mathrm{M\Omega}$ resistance comes from the ultrafast probe used to measure the current.

The actual voltage on the junctions $\mathrm{V_j}$ is thus not equal to the set voltage exiting the AWG $\mathrm{V_{set}}$ but can be estimated from the measured current I and the known resistance value R as

$$\mathrm{V_j} = \mathrm{V_{set}} - R \cdot I \tag{2.4}$$

This is shown in Figures 2.28 and 2.29 by the black curves together with the measured current (red) and the detected photon counts (blue).

In both measurements the junctions are driven in a low resistance state and are therefore in the trap-assisted tunneling regime. The trap assisted tunneling regime is also confirmed in the current fluctuations, which were already discussed in Section 2.3.1.3 for the same measurements of Figures 2.28 & 2.29 (in Fig. 2.12

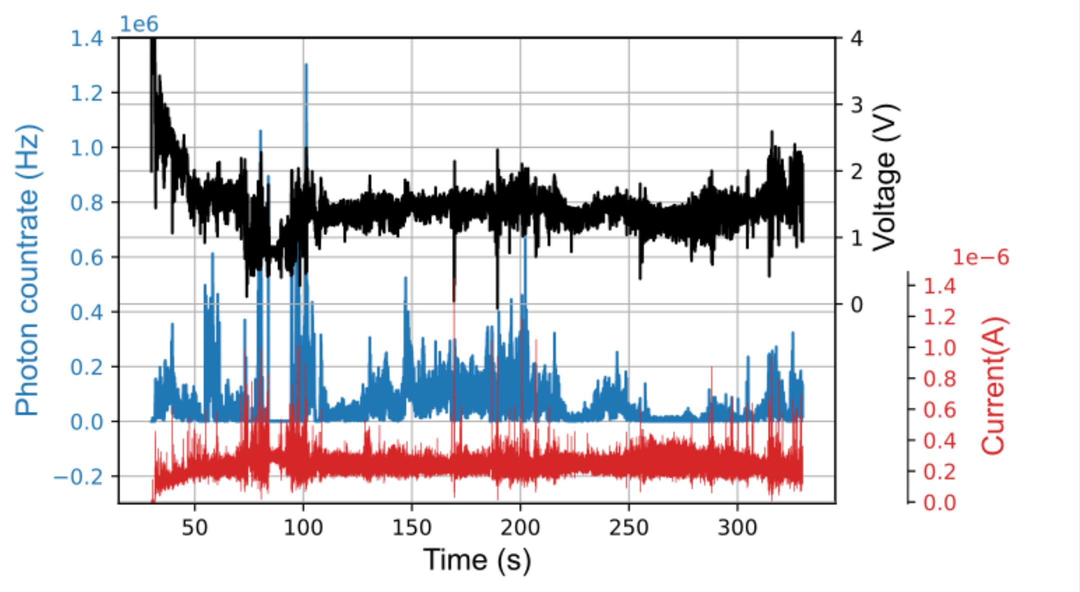

Figure 2.28.: *Time evolution of current (red) and photon counts (blue) for a wide-gap gold junction in air under constant bias. The junction is connected in series with a resistance of* 11 MΩ. *The voltage dropped onto the junction (black curve) depends thus on the current (see main text). The current is also shown in Figure 2.13 a) discussing the current noise observed of junctions in air.*

and Fig. 2.13).

In general with a resistance in series, attention needs to be paid to have the right amount of current flowing. If the current is too high, most of the voltage is dropped on the resistance, the voltage on the gap is then below 1.1 V and no photons are detected. On the other hand if the current is too low the detection sensitivity limits the measurement.

The correct excitation is typically obtained by performing previously several voltage sweeps to reach a desired compliance current. For the constant voltage excitation the applied bias is then set manually to observe a steady but not too rapid current increase. In the experiment of Figure 2.28 the right condition is reached at 4 V. If the current turns out to be to high, reducing the resistance in series to a lower value usually helps lowering the voltage dropped at the resistance.

For the pulsed measurements on the gold gaps in SiO_2, it is more critical to achieve the right amount of current in the gap, as the resistance in series cannot

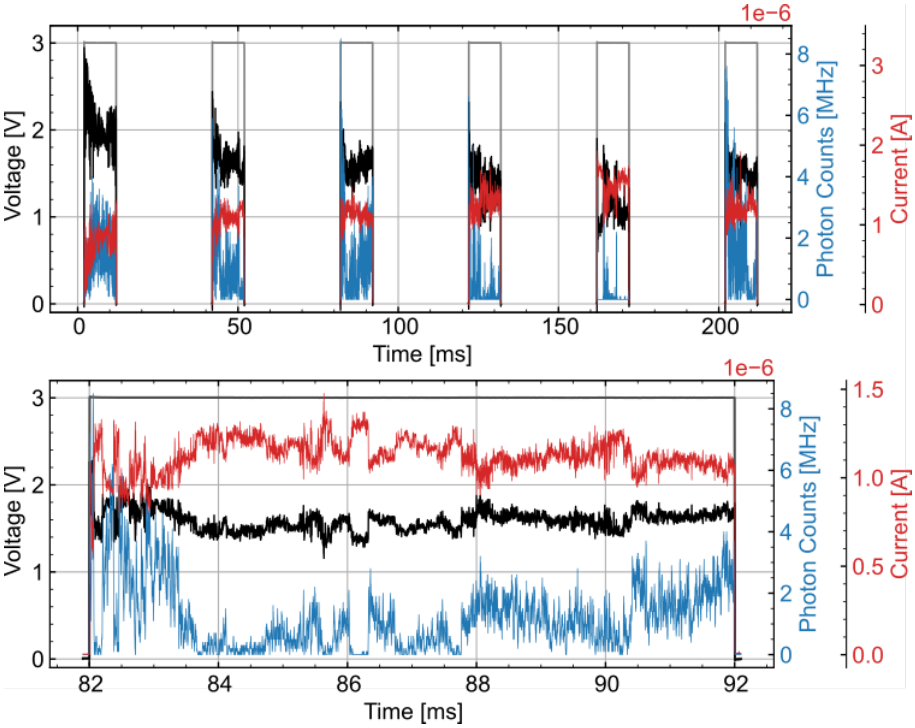

Figure 2.29.: *Pulsed excitation with 3 V pulses (10 ms duration, 20 Hz repetition rate), of a wide-gap gold junction embedded in* SiO_2*. The upper graph shows the first 6 measured pulses, the lower graph zooms into the third pulse. The gray curve shows the total pulse voltage, in black the estimated voltage dropped on the junction, the measured current is shown in orange and the blue curve represents the detected photon counts. The current in the lower graph has already been displayed and discussed in Figure 2.12.*

be changed (set by the active device probe). Besides the voltage amplitude one can play also with the pulse duration to achieve the desired current amplitude. Together with B. Cheng, who kindly provided also the active probe, we were able to reach the sweet spot for several pulsed measurements at different voltages.
The two different electrical excitations are given by experimental measurement constraints. Applying a constant voltage is the most straightforward way of characterizing the junctions, as shown in Figure 2.28. One can run a measurement for 5 minutes, or longer, without any need to change the excitation voltage. In this configuration the junction can slowly (few seconds) reach the desired cur-

rent regime. This is however typically limited in time resolution to avoid large data files and computer memory issues.

To increase the time resolution we used the high speed active probe, replacing the previously used TIA, together with a high time resolution (10 ns to capture the APD signal reliably) on a oscilloscope. This leads to large data files even for measurements lasting only 1 s. Additionally, for such high time resolution the oscilloscope can not display the data in real time as the data handling requires more time then the measurement duration. Therefore we chose to excite the junction with a short train of voltage pulses while still observing conductance switching. From both measurements in air and in SiO_2, one can deduce additional characteristics of the light emission not seen in the spectra shown in the previous section. For example, the already discussed dependence of the light emission on the applied voltage, which may be interfered in the lower plot of Figure 2.29, can be extracted quite immediately from time resolved measurements.

As other effects are not always so obvious to discern, in the rest of this section I will present some additional statistical analysis on both measurements. These will further clarify the light emission mechanism in wide-gap gold junctions.

2.7.1. Photon emission in function of the applied voltage

The relation between photon counts and applied voltage has been already shown in Figure 2.17. However, the voltage range for that particular measurement was limited. Here we explore a larger voltage and therefore electron energy range.

Instead of looking at the photon count rate in function of applied bias, we compute the detected photon emission efficiency, i.e. the number of photons detected divided by the number of electrons flowing inside the junction (which is inferred from the current). As light is emitted by electroluminescence, the number of photons is expected to be proportional to the number of electrons. Looking at the emission efficiency instead of the absolute count rate allows therefore to compare measurements featuring different current magnitudes.

To perform the analysis, the voltage dropped on the junction (black curve in Fig. 2.29,) is binned into discrete voltage steps. Then for each voltage step the mean photon emission efficiency is calculated over the desired measurement range. Such an analysis is shown in Figure 2.30, for 9 series of voltage pulses of 10 ms duration, each having a different set voltage on the AWG.

All the runs (on the same device) show a similar trend. As already noticed in Figure 2.17, one observes a cut-off for applied voltages below 1.1 V (due to the APD detection limit) and a fast increase (several orders of magnitude!) in the

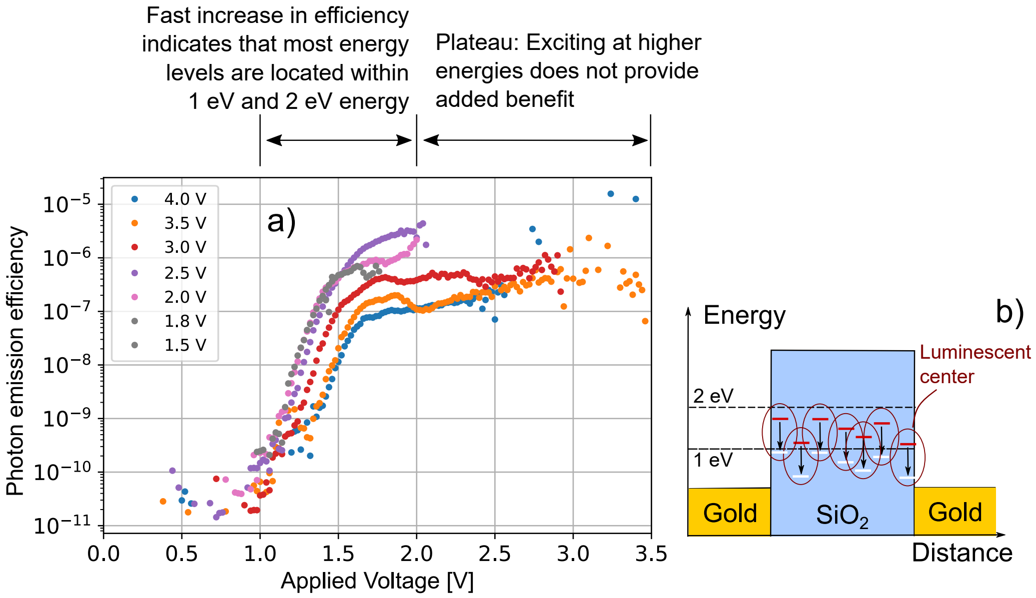

Figure 2.30.: *In a) the detected photon emission efficiencies (plotted in a logarithmic scale) in function of the voltage dropped on the junction measured from different pulse series, such as shown in Figure 2.29, on the same gap embedded in* SiO_2*. The legend indicates the output pulse voltage in the experiment dropped on the junction in series with the* $1.25\,\mathrm{M}\Omega$ *resistance of the active probe. All of the curves follow a similar trend, showing a fast emission increase between 1 V and 2 V and then stable (or slower increase) of the photon emission efficiency for higher applied voltages. This expresses that most of the excited luminescent states lay between 1 eV and 2 eV energy, as sketched in figure b).*

emission efficiency until about 2.0 V. For higher voltages the emission efficiency reaches a plateau. The fast emission increase together with the observation of a saturation at higher applied voltages is partially explained by the APD's spectral detection efficiency, as discussed already in Figure 2.17. The increase also suggests that the excited energy levels of most of the detected luminescent centers lay in an energy range between 1.1 eV and 2 eV. This energy range is also close to the energy range of the emitted photons between 1.24 eV (1000 nm) and 1.8 eV (700 nm) as observed in the spectra of Figure 2.25. It seems thus that when a photon is emitted (for applied voltages up to 2 V) most of the kinetic electron energy is converted into photon energy. In this case the presence of intermediate nonradiative steps resulting in considerable energy loss can be excluded to contribute to the emission process at the luminescence centers. Nevertheless, in absolute value, there are important differences between the runs: at 2 V applied bias, we observe photon emission efficiencies ranging between 10^{-7} photons/e^- and $5 \cdot 10^{-6}$ photons/e^-. This might be intrinsic to the electroluminescence mechanism itself, as light emission by electron injection into luminescent defects competes with current conduction through non-radiative defect states. Depending on the condition photon release might be at times more or less probable. This range of efficiencies is comparable to what is observed for similar gap devices relying on light emission from inelastic tunneling [35, 107].

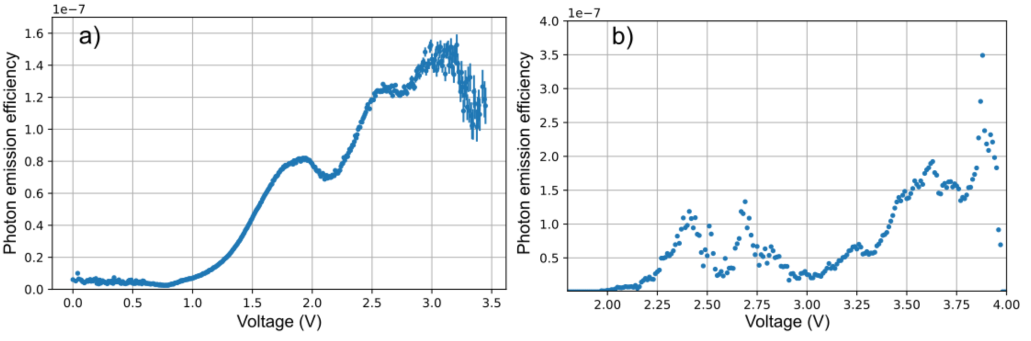

Figure 2.31.: *The average detected photon emission efficiency (here in a linear scale) versus the voltage dropped on the wide-gap junction in air is shown. In a) extracted from the measurement shown in Figure 2.28. The statistics features some well defined broad peaks. The detected photon counts below 1.1 V are probably due to background noise and an underestimation of the applied voltage on the junction due to current transients and a measurement overshoot in the TIA. In b) the same statistics extracted from a similar measurement with constant voltage excitation of a junction in air is shown. Because no lower voltage (dropped on the junction) was observed in the measurement, the curve starts at 2 V. Also in this case one distinguishes the presence of peaks in the average emission efficiency.*

For the sake of completeness, we performed the same analysis for the wide-gap gold junction in air under constant bias. Figure 2.31 shows the photon efficiency for two runs. Here the graphs feature well defined resonances. Such peaks are also present in Figure 2.30 but less visible due to the log scale in y-axis. The peaks are thus a generic feature regardless of the chosen excitation or junction environment. The number of resonances and their position in voltage are however not constant between runs. Their presence suggests the occurrence of preferred energy states stochastically distributed in energy.

2.7.2. Current change and light emission

The large spread in emission efficiencies observed between different runs in Figure 2.30 rises the question if there are other physical observables correlated with the photon generation process. For example, the high time resolution enabled using the active probe allows to investigate the relation between current change and photon emission, which will be presented in this section.

This is illustrated in Figure 2.32 a), where, for the same pulsed measurement

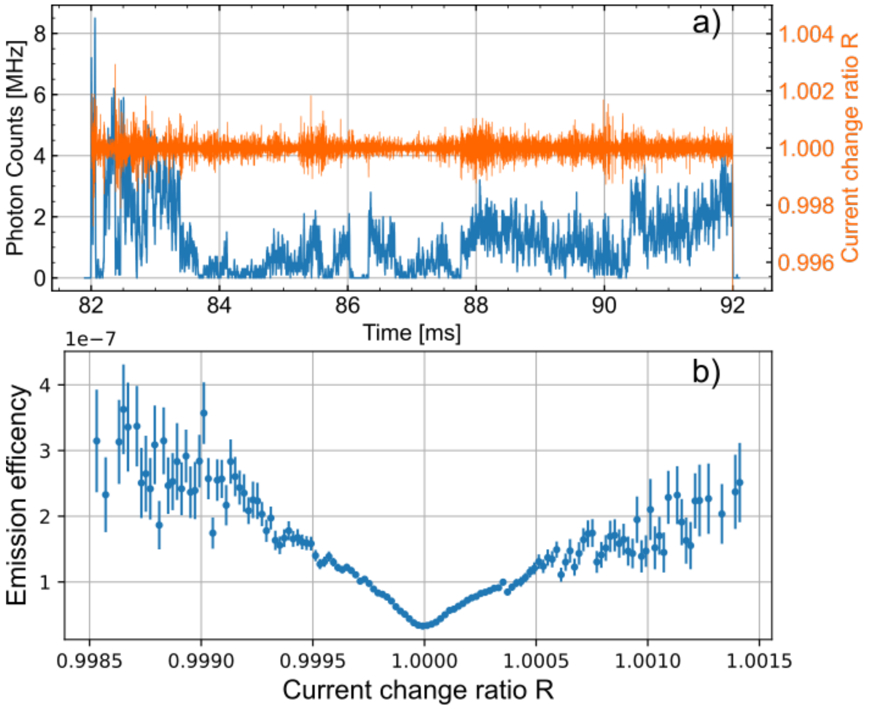

Figure 2.32.: *a) For the same measurement of figure 2.29, the photon counts (blue) and the normalized current change ratio R (orange) are shown for the third pulse. b) the average photon emission efficiency versus the normalized current change ratio R. One clearly observes a trend towards higher photon counts for larger changes in current.*

displayed in Figure 2.29, the detected photon counts (blue) and the normalized current change ratio $\mathrm{R(t)} = \frac{\mathrm{I}(t+\delta t)}{\mathrm{I}(t)}$ (red curve) are shown in time. In Figure 2.32 a), the correlation between the two signals barely stands out. In average over the whole measurement sequence we however observe a clear correlation between current change R and the photon emission efficiency. As seen in Figure 2.32 b), for larger current changes, or R further away from 1, the photon emission efficiency typically increases. To explain this relationship is slightly more challenging, I will try to provide here a hypothesis.

As mentioned in Sect. 2.3.1.3, trap-assisted tunneling is characterized by clear current fluctuations due to charge trapping of electrons and the subsequent closing of conduction paths. The relation between R and the photon emission hints therefore that charge trapping is associated to photon emission. This seems reasonable if we consider again the electroluminescence mechanism sketched in Figure 2.20: First an electron hops onto the excited state of a luminescent center. Therein the electron is trapped until its decay to the ground state, while emitting a photon, and subsequent hopping onto another state. The relation between charge trapping and photon emission appears thus naturally. This association between charge trapping, current change and photon emission will be further confirmed in the following section about photon blinking.

2.7.3. Photon blinking

During the measurements not only the current is varying and showing abrupt changes but so does the photon count rate. The presence of intermittent bright luminescent spikes in the time trace resembles to photon blinking dynamics observed in the photoluminescence of single or few emitters such as molecules and semiconductor quantum dots [108–112]. Here I will also analyze the time duration and distribution of these spikes to further gain insights on the junction's behavior.

In photon blinking the emitters under constant excitation intensity show a switching between periods of bright light emission and periods of dimmer light intensity, the so-called on and off states. This is typically materialized in the count rate occurrences as two well separated distributions [110], one for the bright and one for the dark state. However, the wide-gap gold junction show rather a broad distribution in the count rate histograms, as illustrated in Figure 2.33. This indicates a continuous distribution of grey states, which is due to a continuously varying emitter brightness with time [110] or the observation of several emitters with different brightnesses over the whole measurement. The fast decaying tail towards higher count rates, the straight decreasing line

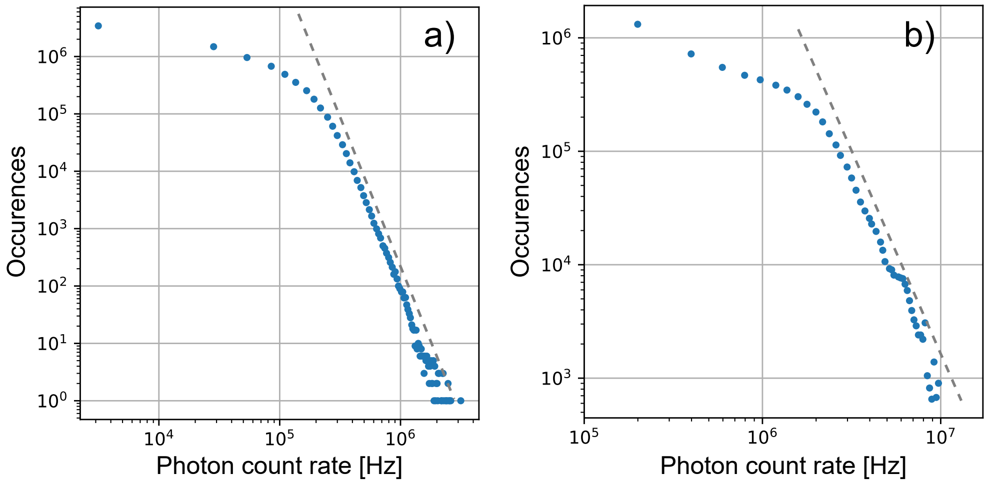

Figure 2.33.: *Distribution of detected photon count rates for the measurements of Figure 2.28 in a) and Figure 2.29 in b). The dashed lines are guides to the eye marking the asymptotic behavior.*

in log-log scale observed in the plots, is consistent with the bounded pareto principle [113]. This statistical distribution is typically observed in surface enhanced Raman spectroscopy of single quantum emitters [114–116], or during photobleaching processes [113] and is characteristic of rare but really intense events.

A second parameter to characterize the intensity blinking is the distribution of bright emission times and the dark times. The behavior of these distributions additionally characterize the internal dynamics of the emitter [110]. Typically for the photoluminescence of metal clusters a power law distribution as eq. 2.2 was observed [117–119]. This power law in blinking was reported consistently in literature also for other structures (typically quantum dots) [110, 111, 117, 118, 120–122], with exponents varying between -1 and -2.2 and is usually explained by charge trapping inhibiting the excitation or emission processes [111, 121, 123]. To distinguish between dark and bright states among a distribution of ”gray” states we manually choose a threshold value separating the two emission regimes. There are more refined ways of separating between bright and dark emission states, see for example [124]. Here we kept the analyses the simplest as possible. Once the bright and dark periods are known, one then calculates the duration of the bright emission (on time) and the dark emission (off time), and plots a

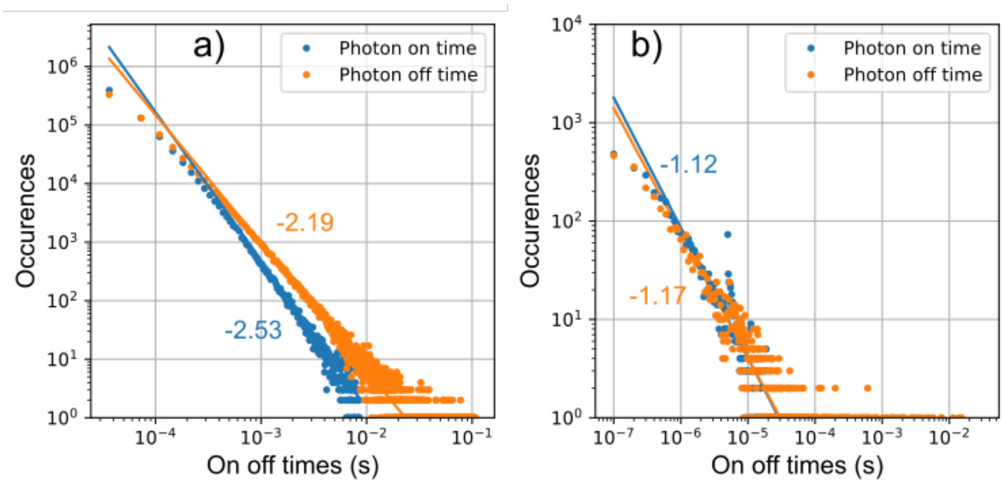

Figure 2.34.: *Occurrences of bright (labeled on) and dark (off) photon emission times for light emission from wide-gap gold junction in air (a) and embedded in* SiO_2 *(b). In a) the occurrences were obtained from the measurement of Figure 2.28 with a threshold of 1.2 times the average photon count rate. In b) the histogram extracted from the pulsed measurement of Figure 2.29 with a threshold of 5 times the average photon count rate. In both figures the fitted power law is shown (continuous line) together with its exponent* α.

histogram of the occurrence of all on and off times. This is shown in Figure 2.34, in a) for a continuous excitation of a junction in air, and in b) for a pulsed excitation of a junction covered by SiO_2.

For both on and off times, a linear decrease in the log-log plot of the occurrences is observed irrespective of the excitation and junction geometry. The number of occurrences N versus the time duration τ of on or off state obeys therefore a power law relationship of eq. 2.2:

$$N \propto \tau^{\alpha} \tag{2.2}$$

The continuous measurement is characterized by slightly different exponents of $\alpha = -2.5$ and -2.2 for the on resp. off times. The last values are quite similar to the power law of -2.28 extracted from the current fluctuation in Figure 2.13 of section 2.3.1.3. The pulsed measurement features much smaller power law exponents of about -1.1 and -1.2. It is difficult to establish whether the difference in the exponents is due to the dielectric environment or the excitation. It is also not clear to me how the luminescence mechanism and dynamics in particular

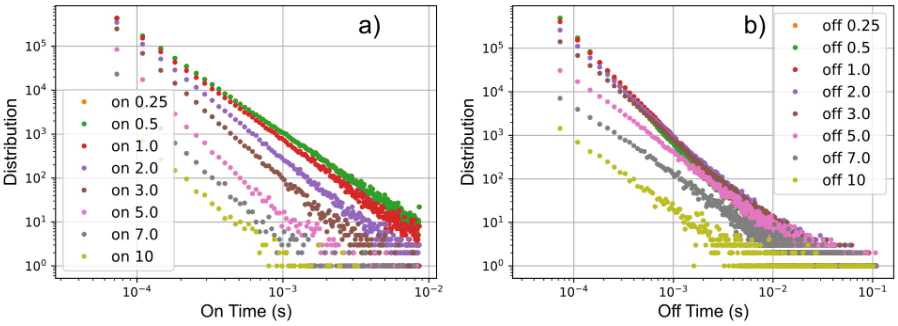

Figure 2.35.: *The dependence of the occurrences of bright and dark time durations on different thresholds extracted for the measurement of Figure 2.28. Clearly in a) for the on times and in b) for the off times one still observes linear slope in the log-log plot indicating a power law relationship for all the chosen thresholds (the legend indicates the threshold level in function of the photon average).*

influence the power law exponent.

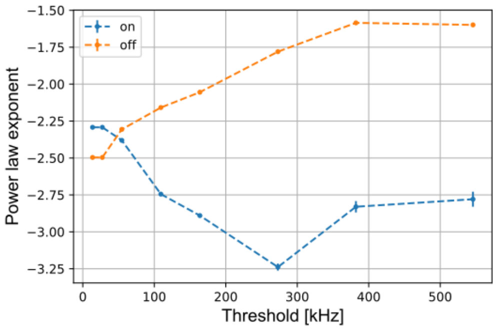

Figure 2.36.: *The evolution of the power law exponents of Fig. 2.35 in function of the threshold.*

The observation of this power law behavior in the occurrences of on and off times is observed for wide range of thresholds, as shown for the junction in air measurement in Figure 2.35 (a) and (b). The photon thresholds in (a) and (b) are indicated as a multiple of the mean photon count rate. The choice of threshold does affect the exponent of the power law, as shown in Fig. 2.36, where the fitted power law exponents vary between -1.5 and -3. The power law exponent is thus not fixed parameter qualifying the light emission as it varies with the chosen threshold [109]. It may be extracted more robustly with a more refined method. The observation of the power law itself is however robust.

The photon blinking links thus the photon emission again to the electroluminescence of discrete emitters, as is the case for quantum dots and single emitters, whose light emission is modulated by charge trapping and detrapping.

2.7.4. Photon autocorrelation

The fluctuations can be further analyzed using the photon autocorrelation [125]. Despite its apparent simplicity the photon autocorrelation is a quite powerful tool revealing the time dynamics of photon emitters [126], such as the diffusion of gold nanoparticles [127] or the binding rates of DNA in cells [128]. Determining the photon autocorrelation therefore allow us to investigate the dynamics of the wide gap gold junctions and will be the last analysis presented in this chapter. The (normalized) photon autocorrelation is defined as:

$$g_2(\tau) = \frac{< I(t+\tau)I(t) >}{< I(t+\tau) >< I(t) >} - 1 \tag{2.5}$$

where $I(t)$ is the detected photon count rate at time t and the brackets indicate averaging. The definition adapted here is typical for fluorescence correlation spectroscopy experiments [128], considering time delays between 100 ns to 1 s. The photon autocorrelation shall also be discussed in Chapter 5, but shorter time delays below 60 ns will be considered. There, a different convention of the autocorrelation will be adopted.

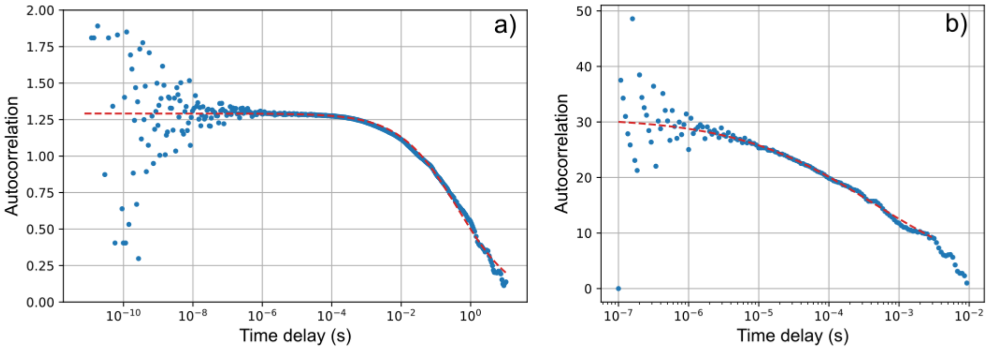

Figure 2.37.: *Normalized photon autocorrelation in a) for a wide-gap gold junction exposed in air with constant voltage excitation. The measurement in time is shown in Figure 2.28. In b) for a wide-gap gold junction embedded in* SiO_2 *with pulsed electrical excitation. The time trajectory is shown in Figure 2.29.*

The deduced photon autocorrelation curves are shown in Figure 2.37, in a) for the junction in air and in b) for the gap embedded in SiO_2.

The autocorrelation curve in a) is obtained by connecting the APD to the TCSPC module (Hydraharp 400, Picoquant), which attributes to each photon arrival with a time resolution of 1 ps.[4] From these timestamps the autocorrelation curve can then be deduced. For the pulsed measurement (shown in Figure 2.37 b) the time resolution of 10 ns was sufficient to calculate the photon autocorrelation directly from the oscilloscope time trace with a resolution below the dead time of the APD of 35 ns.

In Fig. 2.37 a), the photon autocorrelation of the junction in air shows an almost constant plateau for time delays between 10^{-6} s to 10^{-3} s, before decreasing to zero at larger time delays. The decrease to zero towards is expected as any correlation (or memory) within the same system will disappear after long enough time.

For the pulsed excitation (Fig. 2.37 b)) of the junction embedded in SiO_2 no constant plateau in the autocorrelation is observed, the autocorrelation decreases steadily since the shortest time delays (10^{-7} s) towards 0.

To fit the autocorrelation curves an anomalous diffusion model is chosen. A detailed overview of anomalous (sub-) diffusion is found in [129]. Among the various models presented which predict anomalous diffusion, the continuous time random walk assumes particle (electron) hopping between disordered traps having a continuous distribution of escape times. Anomalous diffusion seems therefore appropriate to fit the emission from the junctions, as we associated earlier electron transport and photon emission to charge hopping and trapping.

The anomalous diffusion model predicts an autocorrelation of:

$$g_2(\tau) = \frac{1}{N} \frac{1}{1 + \left(\frac{\tau}{\tau_a}\right)^{\beta}} \tag{2.6}$$

where N is the average number of detected emitters, τ_a the active time of emission and β is the diffusion exponent. For normal diffusion, seen in brownian motion, $\beta = 1$. If $\beta < 1$ one speaks about subdiffusion and if $\beta > 1$ about superdiffusion.

The fitted curves overlap quite nicely with the experimental data, as seen in Figure 2.37, with the extracted parameters shown in table 2.1.[5] Both measurements show subdiffusion with a similar anomalous diffusion parameter β around

---

[4] The detection setup for this measurement was actually slightly more complicated, instead of a single detector, two APDs and a beamsplitter were used. This implements a so called Hanbury Brown Twiss interferometer, see Chapter 5. It allows to avoid the dead time issue when using a single APD and measure the photon correlation down to zero time delay and was set-up to search (unsuccesfully) for antibunching of the light emission.

[5] For the anomalous diffusion fits I would like to thank Dr. A Leray for his input and help.

	N	τ_a	β
Fig. 2.28 Junction in air	0.77(1)	410(50) ms	0.52(4)
Fig. 2.29 Junction in SiO_2	0.0325(4)	0.42(3) ms	0.44(2)

Table 2.1.: *The fitted anomalous diffusion parameters of the autocorrelations shown in Figure 2.37. The brackets indicate the uncertainty in the last digit, i.e.* $0.77(1) = 0.77 \pm 0.01$.

0.5.

The average number N of active centers, although differing between both measurements, is in both cases below 1. It implies that (in average) less then one center is emitting at a time. The statistics and analyses shown above are thus not an average of many sources emitting at the same time, but a time integrated average over various emitters emitting at different times. This demonstrates a remarkable consistency with the previous analyses above such as the spectral peak wandering or the photon intermittency. Both discussions relate the observed features to the presence of one or few emitters.

From the average number of centers and the average photon detected photon count rate $\mathrm{I}_{\mathrm{det}}$ one can estimate the average emission rate of a single center γ_{em} as:

$$\gamma_{\mathrm{em}} = \frac{\mathrm{I}_{\mathrm{det}}}{N\eta_{\mathrm{coll}}} \tag{2.7}$$

where $\eta_{\mathrm{coll}} = 0.14$ is the estimated collection efficiency of our optical setup.[6] This gives an average waiting time between two photon emission events of the source of $\tau_{phot} = \gamma_{\mathrm{em}}^{-1}$ of 2.1 µs (63 ns) for the measurement of Fig. 2.28 (resp. Fig. 2.29). All these values are found in Table 2.2.

This waiting time gives an upper limit on the lifetime of the excited state in the luminescent centers τ_l (averaged over all emitters) as it is determined by the following relation [130, 131]:

$$\frac{1}{\tau_{phot}} = \gamma_{\mathrm{em}} = \mathrm{I}_{\mathrm{el}}\sigma_{\mathrm{hop}}\frac{\eta_{\mathrm{rad}}}{\tau_l} \tag{2.8}$$

---

[6] The collection efficiency η_{coll} is estimated as follows :

$$\eta_{\mathrm{coll}} = \mathrm{R}_{\mathrm{ph}} \cdot \mathrm{T}_{\mathrm{obj}} \cdot \Gamma_{\mathrm{APD}} = 0.5 \cdot 0.7 \cdot 0.4 = 0.14$$

where $\mathrm{R}_{\mathrm{ph}} = 0.5$ is the estimated fraction of photons emitted into the objective, $\mathrm{T}_{\mathrm{obj}} = 0.7$ is the mean transmittance of the objective and $\Gamma_{\mathrm{APD}} = 0.4$ is the mean detection efficiency of the APD.

where I_{el} is the electron current and σ_{hop} is the probability of single electron to hop on the luminescent center. Because a single electron cannot excite more then one luminescent center, one necessarily has that $I_{el}\sigma_{\text{hop}} < 1$. $\eta_{\text{rad}} \leq 1$ is the probability of the luminescent center to emit a photon into the far field.

The measurements performed do not allow to determine the remaining parameters σ_{hop}, η_{rad} and especially τ_l experimentally. In order to do so one would need to excite the junctions with a series short electrical pulses (about 1 ns or below) and construct a histogram of the photon arrivals with respect to these pulses, similar to a TCSPC lifetime measurements [132]. In photoluminesence experiments the reported lifetime of gold clusters [96] and silicon clusters [97] is given by a few ns, with a size dependent η_{rad} between 0.1 and 0.5 [96,98]. With these values one can estimate that an average of $I_{el}\sigma_{\text{ext}} \approx 0.001 - 0.2$ electrons are trapped into the excited state of a luminescent center when such is present. The anomalous diffusion model provides also another time scale τ_a, the (average) active emission time of an emitter. In photoluminescence experiments this is the time duration a single emitter remains inside both the excitation and detection volume. Similarly we can consider it here as the mean emission duration of an emitter, limited both by the diffusion of the emitter or the current path, allowing electrons to excite the emitter, and the stability of the emitter itself. τ_a is quite different between both measurements, see 2.1. For the junction in air we observe $\tau_d = 410\,\text{ms}$, whereas the junction in SiO$_2$ shows $\tau_d = 0.42\,\text{ms}$, a factor 1000 lower.

	Mean detected photon count rate I_{det}	Mean emitter count rate γ_{em}	Mean photon emission time τ_{phot}
Fig. 2.28 Junction in air	54 kHz	472 kHz	2.1 µs
Fig. 2.29 Junction in SiO$_2$	72 kHz	15.8 MHz	63 ns

Table 2.2.: *The extracted mean emission time of the luminescent center according to equation 2.7.*

The difference in τ_a between both measurements might be partially explained by the nature of the excitation. Whereas the junction in air under constant bias is all the time in a low resistance state and electrically stressed, the junction embedded in SiO$_2$ is excited by pulses (10 ms duration) and thus switches repeatedly between resistive states. The pulsed excitation seems to promote a faster diffusion dynamics of the conduction path than a constant excitation together with stable current.

Still for both measurements the active time of a single emitter τ_a is at least three order of magnitudes longer than the estimated photon emission time τ_{phot}. In average an emitter emits thus more than 1000 photons before it is no longer excited.

We note that the integration time of the spectra for junctions embedded in SiO_2 shown in Fig. 2.21 d) and 2.25 is about 4 order of magnitudes longer than τ_a. The spectra are thus a superposition off many emitters in time.

The integration time of the constant bias spectra of Figure 2.23 for wide-gap junctions in air is with 5 s only about ten times higher then the observed τ_a for the junctions in air, which allows to attribute the observed peaks to few (possibly even single) emitters. This is also supported by the narrower widths of these peaks, as already discussed in section 2.6. The consistency of peaks across successive spectra suggests that τ_a is mainly limited by current path variations, rather than the formation and disintegration of these luminescence centers. The disintegration of an emitter and the formation of a new luminescent defect or cluster should instead result in almost no spectral continuity, as one would expect a different emission peak for the newly created emitter. This is observed sometimes in the spectra of Figure 2.23[7] but seems to happen on a longer time period and thus does not limit τ_a.

This is further confirmed by the observation that, for both junctions in air and SiO_2, τ_a is in the same order as the observed upper limit of on and off time duration of the photon blinking seen in Figure 2.34.

Similar to the photon autocorrelation one can also extract a (normalized) cur-

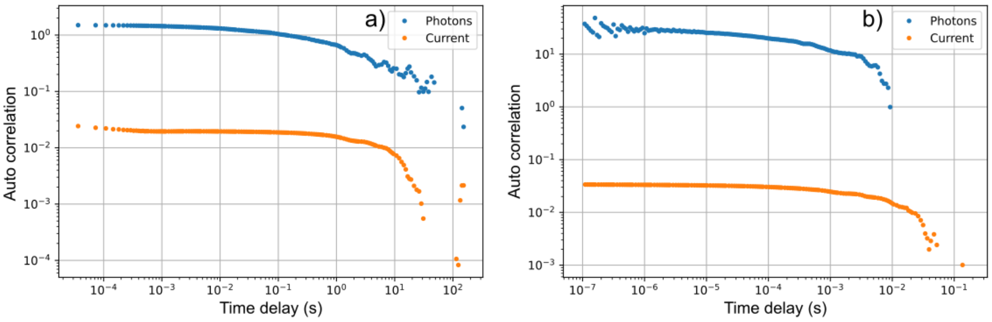

Figure 2.38.: *Photon and current autocorrelation for the same measurements as of Figure 2.37 a) and b).*

---

[7] For example between the red and green spectrum of Fig. 2.23 a)

rent autocorrelation from the measurements, as illustrated in Figure 2.38. This current autocorrelation can also be fitted by the anomalous diffusion model. Both the amplitude (lower) and characteristic time scale (longer) are different for current and light. The emitted radiation displays intrinsic dynamics not determined by the current transport. We understand this as the current conduction involves many trap states with possibly vastly different dynamics. Among all defects, only a fraction may be optically active.

2.8. Conclusion and outlook

This chapter presented and discussed the current transport and light emission from wide-gap gold junctions exposed to air and embedded in a deposited SiO_2 matrix. Both type of devices show light emission upon electrical activation from a diffraction limited gap located between two gold electrodes.

The observation of very similar behaviors for both type of devices strongly suggests a common operation principle. Switching between a high resistance state and a low resistance state is consistently associated with the emission of visible photons. This switching is explained as the passage from Fowler-Nordheim tunneling to trap assisted electron tunneling allowed by the creation of localized electron trap states in the dielectric. These trap states are either coming from intrinsic and newly created SiO_2 defects or the migration of gold ions and clusters into the dielectric. The electron transport through trap assisted tunneling is demonstrated by analyzing current fluctuations.

Experiments such as the emitted spectra or photon time trajectories clearly indicate that light is emitted either by the electroluminescence of SiO_2 defects or gold clusters. The detected photon emission efficiencies are in the order of 10^{-6} photons per electron.

Statistical analysis of the light revealed also a correlation between light emission and current changes, attributed to the excitation mechanism of the luminescent emitters. The detected photon blinking and the photon autocorrelation indicated further a contribution of few single emitters. In particular from the photon autocorrelation further properties of the emitters could be studied, such as the average emission rate γ_{em} and the active time of an emissive center τ_a. For example γ_{em} provides an upper limit of the (averaged) luminescent lifetimes of 2.1 µs (63 ns) in air (resp. in SiO_2). These are compatible with the lifetimes of silicon and gold clusters reported in the literature of a few ns.

To distinguish whether gold nanoclusters or silicon clusters in SiO_2 is the dominant contribution is difficult since their emission wavelength coincides and the expected dynamics and behavior are quite similar. In light of the gold diffusion clearly observed by SEM images in Figure 2.14 I tend to consider light emission by gold clusters as the most probable contribution. There is however no strong evidence from the presented measurements as both species have very similar emission characteristics.

In order to resolve this question more advanced characterization techniques such as TEM or XPS may help. The XPS however lacks the necessary spatial resolution (limited to ~10 µm) and the TEM would require a specific sample preparation, which was beyond the possibilities (time) of this thesis work.

Although in our measurements we have done more than just scratch the surface of the emission phenomenon in wide-gap gold junctions, much more can be done. Is it possible to stabilize the spectral emission and to increase the active time τ_a? Between different measurements a wide range of emission efficiencies in Figure 2.30 have been observed, although applying the same voltage and the same current. Could this be controlled to achieve consistently higher efficiencies? How fast can the light emission by the wide-gap gold junction be modulated?

Further experiments on these junctions are thus needed. Instead of using constant DC bias one could also try using a high frequency AC electrical excitation to drive the junctions. This may lead to an increased photon efficiency, as shown in [133] for the electroluminescence of silver nanoclusters. Similarly photon correlation Fourier spectroscopy [134] could extend the autocorrelation measurements, potentially revealing even more about the dynamics of the emission process.

In addition different dielectric matrices and electrode materials could be investigated to study and enhance the light emission. This has been partially adressed in this thesis work and will be shown in the next chapter, where the light emission from silver-platinum gaps is presented.

Chapter 3.

Light emission in silver-platinum memristors

The silver-platinum memristive devices studied in this chapter are almost identical to the wide-gap gold junctions of the previous chapter. The junctions consist of two metallic electrodes (silver and platinum) separated by a gap and embedded in SiO_2, as shown in Figure 3.1. Like the gold junctions, these structures show resistance switching and hysteresis with the application of a bias. This resistive switching is even more reliable for the silver-platinum junctions [41, 78] so that these devices are used as memristive circuit elements[1] to potentially provide integrated and down scaled functionalities such as ultra compact digital memories [136], energy efficient logical operations [135] or neuromorphic computing [137, 138].

This chapter presents the light emission of these memristive devices. This gives an additional access to study the physics of such junctions and adds to these devices a new functionality [139], while keeping the compact size and the same fabrication effort.

The results presented here were obtained in a collaborative effort with Bojun Cheng and Till Zellweger from the Institute of electromagnetic fields at ETH Zurich, who provided the sample. The electro-optical experiments were carried out in Dijon.

---

[1] "Memristive devices are electrical resistance switches that can retain a state of internal resistance based on the history of applied voltage and current", quoted from [135].

Device fabrication and structure

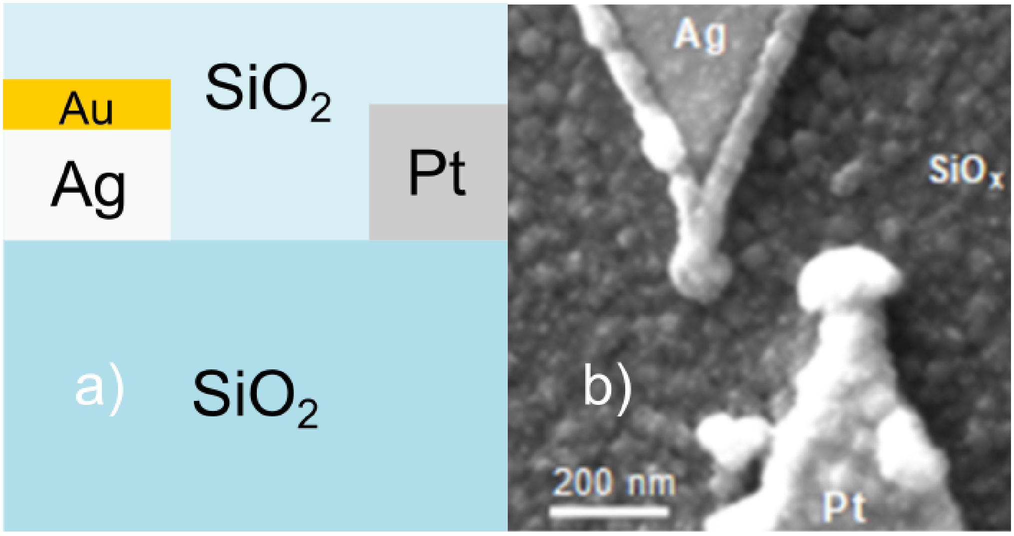

Figure 3.1.: *In a), sketch showing the profile of the silver-platinum memristor structure. In b) SEM image of a silver-platinum memristive device.*

The structure of a typical device is sketched in Figure 3.1 a). The devices are fabricated on top of standard glass cover slips, by first depositing a silver layer covering the entire substrate (30 nm with 1nm chromium adhesion layer) and a small gold layer (15 nm) to protect the silver from oxidation. By using e-beam lithography, an etch mask is patterned and the silver is then dry etched by argon ions. In a second step, platinum structures are deposited (50 nm thickness, 3 nm chromium as adhesion layer) by another e-beam lithography step and a lift-off procedure. Finally everything is embedded into 60 nm amorphous SiO_2 obtained by RF-sputtering. To access the electrodes with electrical probers, the SiO_2 on top of the electrodes is removed by dry etching with CHF_3. A more detailed description of the fabrication is found in [140, Chapter 5].

Like for the wide gap junctions of gold in SiO_2, the silver and platinum electrodes were designed to form an optical antenna with the intent of increasing light emission and extraction. A series of distances, shapes and sizes were explored, with designed gaps varying between in contact up to gap sizes of 60 nm. Due to alignment issues in the second step of e-beam lithography, a lateral shift occurred between the two electrodes, shown in Figure 3.1 b).

3.1. Memristive behavior

The structures show a qualitatively similar current behavior to the wide-gap gold junctions in section 2.3, this is illustrated in Figure 3.2. At the beginning of each voltage sweep, the device is initially in a high resistance state and then switches to a lower resistance state after a threshold voltage. This is a so-called volatile state as the device does not remain in the high conductive state after turning off the applied voltage. In the non-volatile state the device keeps its conductive state even after the bias is removed. In order to pass from a volatile state to a non-volatile state different voltage sequences can be applied, depending on the memristor structure [138].

The resistance switching of silver-platinum devices can be attributed to two voltage driven effects: the migration of silver ions leading to a silver filament

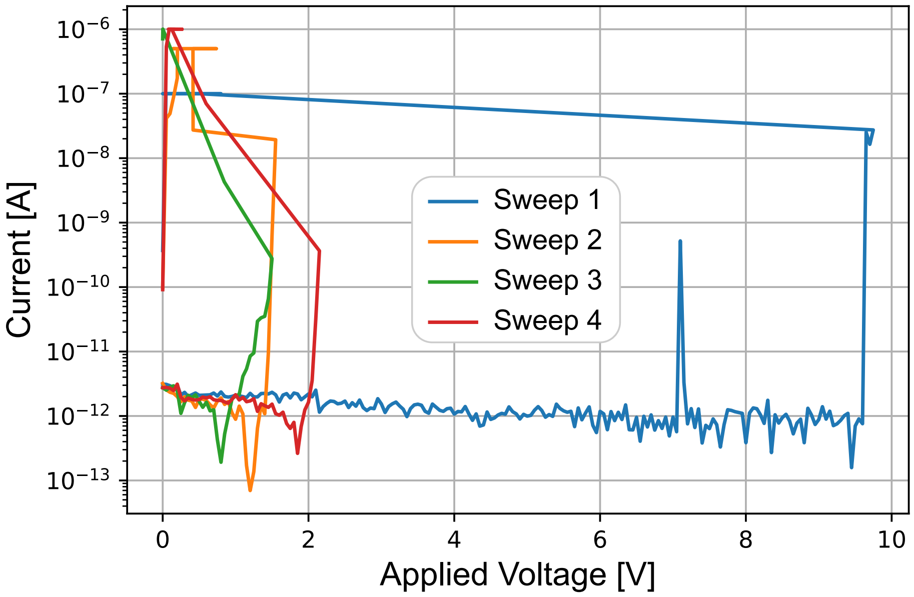

Figure 3.2.: *Four voltage sweeps of silver-platinum memristor, with positive voltage applied to the silver electrode (forward polarity) showing the activation of the dielectric and the hysteresis behavior typical of a memristor. The compliance current was increased from 100 nA (sweep 1), to 500 nA (sweep 2) up to 1 µA.*

growth [79, 140–142] and the creation of oxygen defects in the SiO_2 matrix as already discussed in 2.3. The two mechanisms of resistive switching, metallic filament growth and accumulation of oxygen defects, are likely to be present at the same time, as observed in [143], and interact with each other [79], for example by providing nucleation sites for silver ions at oxygen vacancies [80].

The first mechanism will be briefly described here. The application of a positive electrical potential leads to the creation of positively charged silver ions (Ag^+) at the silver electrode through an oxidation reaction [77, 140]:

$$\mathrm{Ag} \rightleftharpoons \mathrm{Ag}^+ + \mathrm{e}^- \tag{3.1}$$

Due to the electrical field between the silver and the platinum electrodes, these silver ions are driven towards the platinum electrode at negative potential. At the platinum electrode, the silver ions reduce back to silver atoms. This results into a growth of a silver filament from the platinum electrode towards the silver electrode, this growth is facilitated by SiO_2 defects and voids [80, 141]. The filament growth leads to an increased conductivity of the device. For small filaments, i.e. in a volatile device, the structure is not thermodynamically stable without an electrical field and dissolves when the applied voltage is turned off.

For a positive potential on the platinum electrode on a pristine device one might expect to observe a similar platinum filament formation. The filament growth is however expected to be more dominant and faster for silver. First, the oxidation potential of silver (0.8 V) is considerably lower than for platinum (1.2 V) [77]. Second, silver ions have a higher ion mobility and therefore diffuse more easily into SiO_2 than platinum ions [79]. Thus, filament growth is expected to be more important for a positive voltage on the silver electrode, which I will label as ”forward bias” in the following. Indeed, the silver filament growth has been already observed and studied using TEM imaging in [141], whereas I am not aware of any platinum filament growth reported in the scientific literature.

The second mechanism contributing to the observed resistance switching, is the same mechanism of dielectric breakdown of SiO_2 presented in Chapter 2.3.1. The applied bias and electrical current lead to the creation of oxygen vacancies and defects [64] inside the SiO_2. These defects provide an additional conduction paths for electrons between the two electrodes [65], as the electrons can tunnel from defect to defect reaching the opposite electrode. This mechanism is independent of the polarity of the applied voltage.

The polarity of the voltage on the electrodes thus selects the desired conduction mechanism: whereas for forward bias both conduction mechanism, silver filament and SiO_2 defect trap assisted tunneling participate in the current transport, in the case of reverse polarity only the SiO_2 defect mechanism should be present. This can be exploited to identify the contribution of each mechanism as will be seen throughout the measurements below.

3.2. Electrical light emission

Like the wide-gap gold junctions, the memristive devices radiate light from the gap region between both electrodes when driven by an external voltage. This is shown in Figure 3.3, where the image is integrated over a full voltage sweep. Light emission is observed both for forward and reverse polarity of the applied voltage, and was the first objective of our collaborative effort with Bojun Cheng and Till Zellweger from the Institute of electromagnetic fields at ETH Zurich. In the follow up experiments and analyses presented here we will thus characterize and explain the emitted radiation in greater detail.

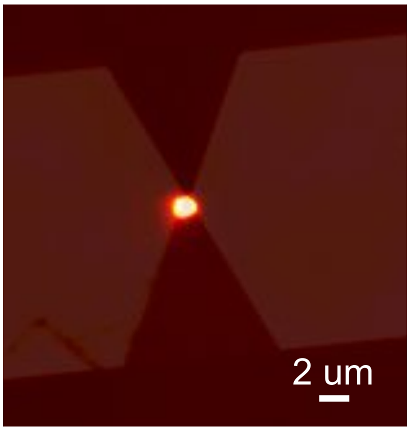

Figure 3.3.: *Superposed bright field image in false color scale showing the light emission from a silver-platinum memristor during a voltage sweep.*

3.2.1. Spectra

Both for forward and reversed applied voltages the observed spectra are emitted into a broad spectral range between 500 nm up to the detection limit at 1000 nm. This is illustrated in Figure 3.4, displaying a spectrum acquired during a voltage sweep with reversed bias and a spectrum acquired with forward bias under pulsed excitation. This spectral range is similar to the one observed in the wide-gap gold junctions of Chapter 2.6. It seems therefore reasonable to attribute the light also to the electroluminescence from centers in the memristors and ignore other mechanism such as light emission by inelastic tunneling. Although not explicitly discussed anymore, this assumption is further confirmed by the measurements and analyses discussed below. In the memristive devices, besides luminescent silicon clusters embedded in SiO_2, already considered in the wide-gap gold junctions, silver nanoclusters [144] (instead of gold clusters) are potentially contributing luminescent sources (in the case of forward polarity).

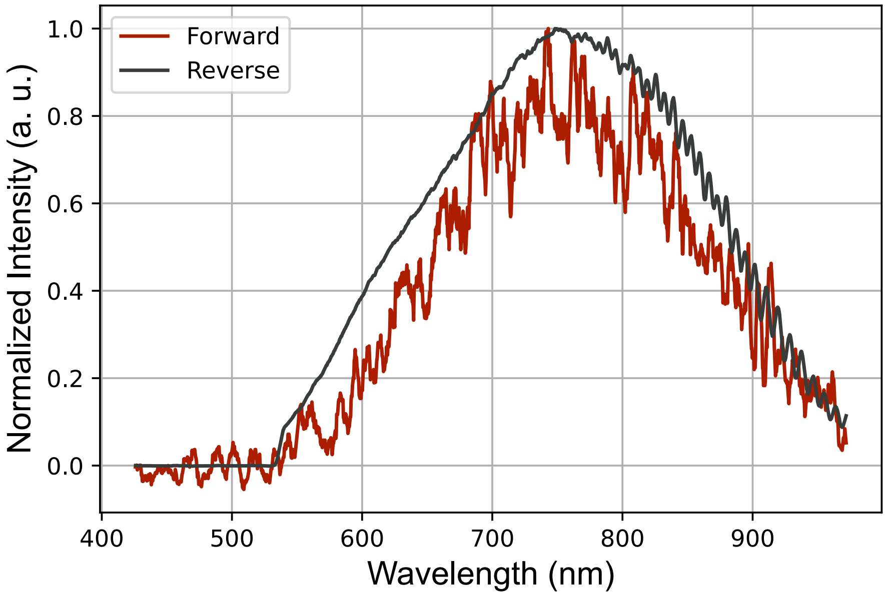

Figure 3.4.: *Spectrum of the emitted light under forward (red, 5 V on 80 5 ms pulses with 30 ms repetition rate) resp. reverse (black, voltage sweep up to 10 V) applied electrical bias for two different memristors.*

The observation of similar spectra for both polarities suggests a dominant contribution of the SiO_2 luminescent centers.
Considering the shifty spectra of the previous chapter and the marked differences between spectra acquired during voltage sweeps (Fig. 2.21 d)) or during pulsed voltage excitation (Fig. 2.25), one might argue that the comparison between the two spectra in Figure 3.4 is not justified. However, the spectra of the silver-platinum memristors are significantly more stable and display an almost identical spectral shape for the same device over multiple excitation cycles. This is seen in Figure 3.5 in several spectra emitted by four different devices. The normalized spectra within each device (each subfigure) show a remarkable overlap (except for Fig. 3.4 c), where a slight between different runs is observed).
Despite a different electrical excitation (voltage sweep versus pulses), the spectra of Figure 3.5 a) and b) stemming from two devices having the same electrode design show very similar (normalized) emission spectra. This seems to confirm the influence of the electrodes shaping of the emission spectra.

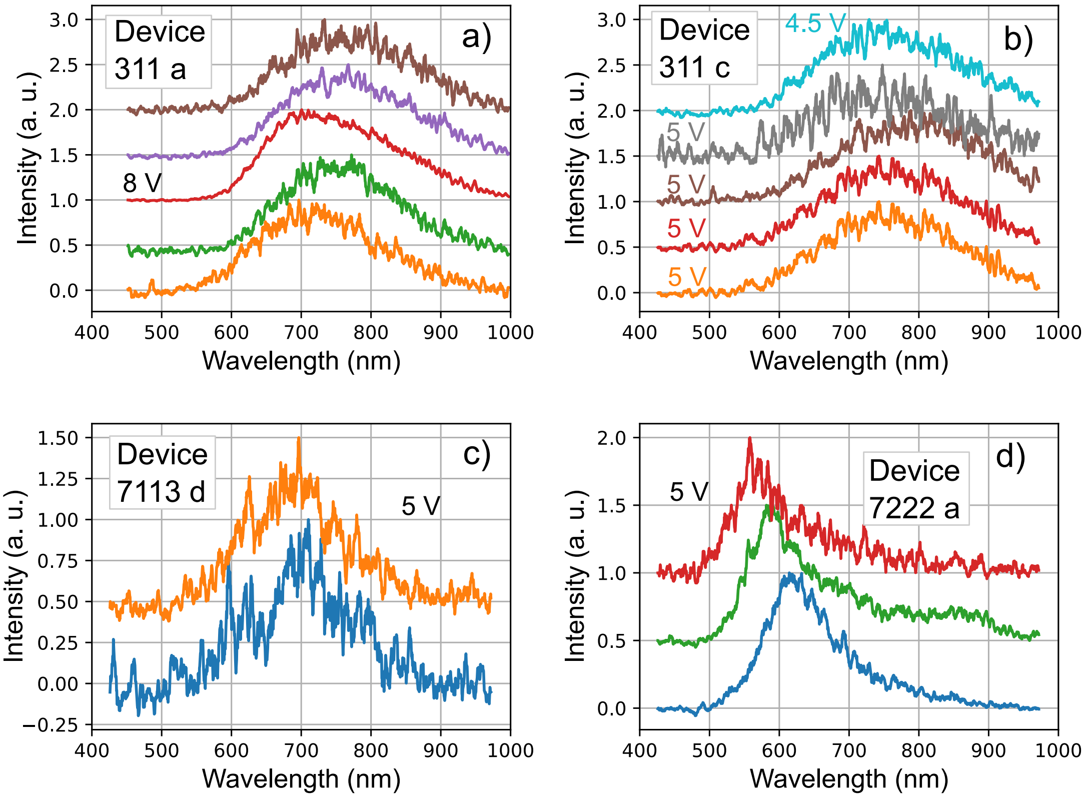

Figure 3.5.: *Series of normalized spectra taken for four different devices under forward bias. The devices 311 a and 311 c shown resp. in a) and b) have the same electrode design parameters. One spectrum of 311 c is shown in Figure 3.4. The spectra of a) were integrated over voltage sweeps reaching 8 V. In b), c) and d) all the spectra where acquired from a series of 5 ms pulses of 5 V (except for the blue curve in b) where the voltage was 4.5 V). In all the measurements* $1.25\,\mathrm{M\Omega}$ *resistance introduced by the ultrafast current probe was in series with the junctions.*

For comparison the simulated antenna enhancement for device 311 c (Figure 3.5 b)) is shown in Figure 3.6. The antenna has a resonance peak around 700 nm, which is at slightly shorter wavelengths than the resonance peak measured in Figure 3.5 a) and b) around 770 nm.

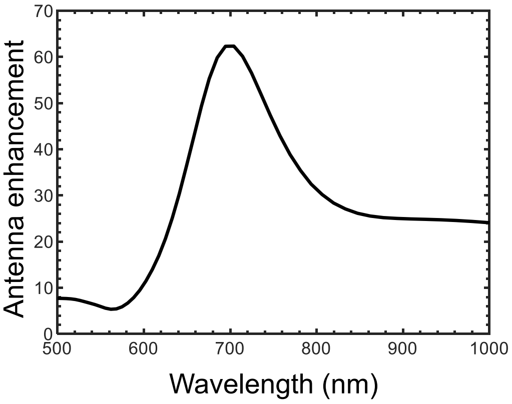

Figure 3.6.: *Simulated antenna enhancement and spectral shaping of the memristor electrodes for the structures of Figure 3.5 a) and b). Reprinted from [102] (licensed under CC BY 4.0).*

In the spectra we observe already some similarities and differences between the light emission of silver-platinum memristors and the wide gap gold junctions. Although both devices emit in the same wavelength range, the memristive devices show a greater spectral stability (even though the amplitude varies between different runs). Since our initial research motivation was to look for light emission from a memristive device, almost all of the experiments were performed in forward bias conditions. This is slightly unfortunate as it prevents us to compare both excitation modes in the time resolved measurements.

3.2.2. Light emission in time

Both the images and spectra provide only a time averaged view of the light emission, as their acquisition is integrated over an entire excitation cycle. This does not allow the characterization of the dynamics of the photon radiation. In this section the dynamics will thus be studied using high resolution time traces. These dynamics show some significant differences compared to the wide-gap gold junctions of Chapter 2.

In particular, the observation of current in a low resistance state does not lead consistently to light emission, but also other parameters (besides the applied voltage) seem to condition photon emission, as illustrated in Figure 3.7. The figure shows the photon emission (blue) during a voltage sweep (gray). Clearly the photon counts are not continuous but feature some few bright periods followed by times with no light emission at all.

Such behavior cannot be explained only by the voltage dropped on the junc-

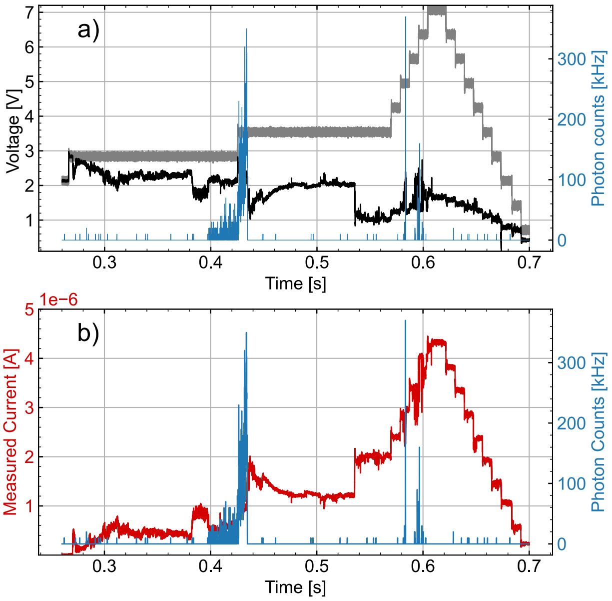

Figure 3.7.: *Light emission detected during a voltage sweep applied on memristor. In a), the gray curve shows the output bias of the SMU, applied onto the memristive device in series with the active probe having a resistance of* 1.25 MΩ*. The voltage dropped on the memristor itself is shown in black. The measured current is shown in red in b). The blue curves on both graphs show the detected photon counts. The light emission is clearly not continuous. There are only few bright moments during which the device emits light.*

tion[2] shown in black in Fig. 3.7, as photon emission is observed at 2 V around 0.4 s but not at 0.3 s or at 0.5 s where the voltage has the same magnitude. For the short burst around 0.6 s in Figure 3.7 the photon emission rather seems to coincide with periods of larger current fluctuations.

A more reliable light emission can be obtained by using a pulsed voltage excitation, as illustrated in Figure 3.8. The figure shows the first six voltage pulses (of a total of 60 pulses) with 5 V, 5 ms duration and 40 Hz repetition rate (gray curve). The measured current is shown in red, the estimated voltage dropped on the junction is shown in black. Each of the first six pulses results in photon

---

[2] All the current measurements were performed with a high speed probe having a resistance of 1.25 MΩ, acting as voltage divider of the SMU output voltage V_{out}. The voltage applied on the junction V_{appl} is thus estimated as $V_{appl} = V_{out} - I \cdot 1.25\,M\Omega$, where I is the measured current.

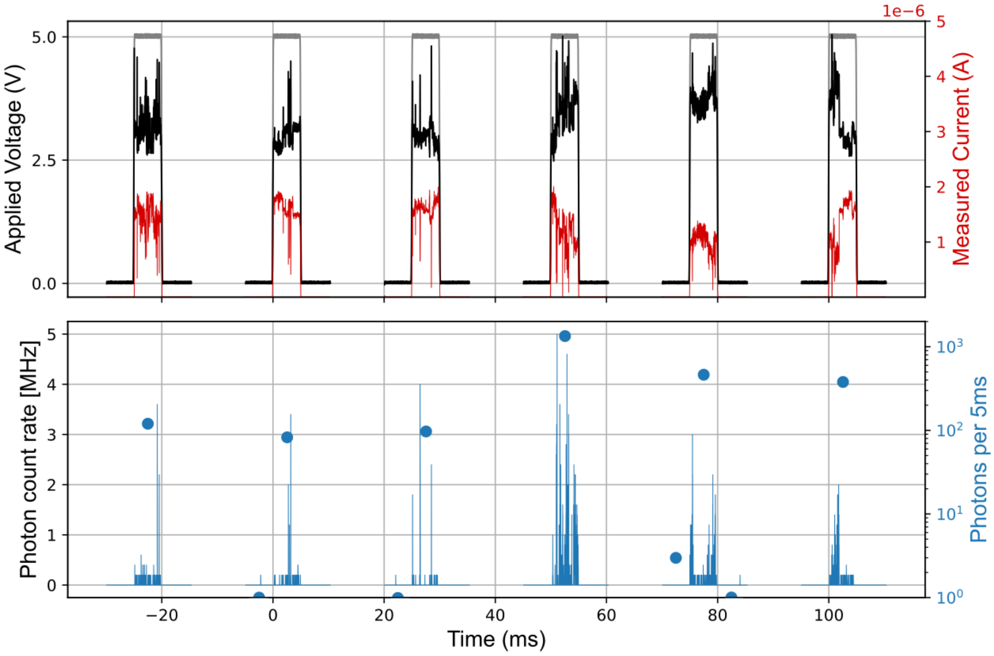

Figure 3.8.: *Pulsed excitation of a memristor with* 60 × 5 *V pulses, of 5 ms duration and 25 ms repetition period, here the first six pulses are shown. The voltage pulse is shown in gray, the voltage dropped on the memristor is shown in black (forward polarity), the measured current in orange. The lower graph shows the detected photon counts, which are binned over* 5 µs*. The blue circles display (in a logarithmic scale) the integrated photon counts over 5 ms, allowing more easily to differentiate between light emission and dark noise form the APD.*

emission (lower graph). Initially the light emission during the pulses is rather bright but decreases after several pulses. This seems to indicate that light is radiated predominantly in the forming stages of the silver filament or when the filament is rather unstable.

However, even in the beginning the photon behavior appears quite unpredictable (as does the current). For further understanding the same statistical analyses previously performed in section 2.7 will be repeated in the following on the pulsed measurement. To allow for an easier comparison with the previous chapter the same order in the analyses is kept.

3.2.2.1. Photon emission efficiency in function of the applied voltage

Although the light emission displays erratic behavior in time, showing widely different photon counts for the same applied voltages, the (detected) average photon emission efficiency in function of the applied voltage is still an interesting measure to understand the emission mechanism, as the voltage limits the energy states which electrons can explore.
The analysis is thus shown in Figure 3.9, each curve representing one third of the measurement (20 pulses). This subdivision is necessary due to the long term emission drop in the pulsed measurement, the choice of three parts is somehow arbitrary: instead of 3 parts one could also choose to divide the measurement more finely in 5 or 10 parts.
The efficiency drop is confirmed in Fig. 3.9, as clearly the first 20 pulses (blue curve) show a consistently higher emission efficiency, than the other two parts of the measurement. The efficiency values up to 10^{-6} photons/electrons are in a similar range as observed in the wide gap gold junctions.
All three curves show more than an order of magnitude increase of the emission

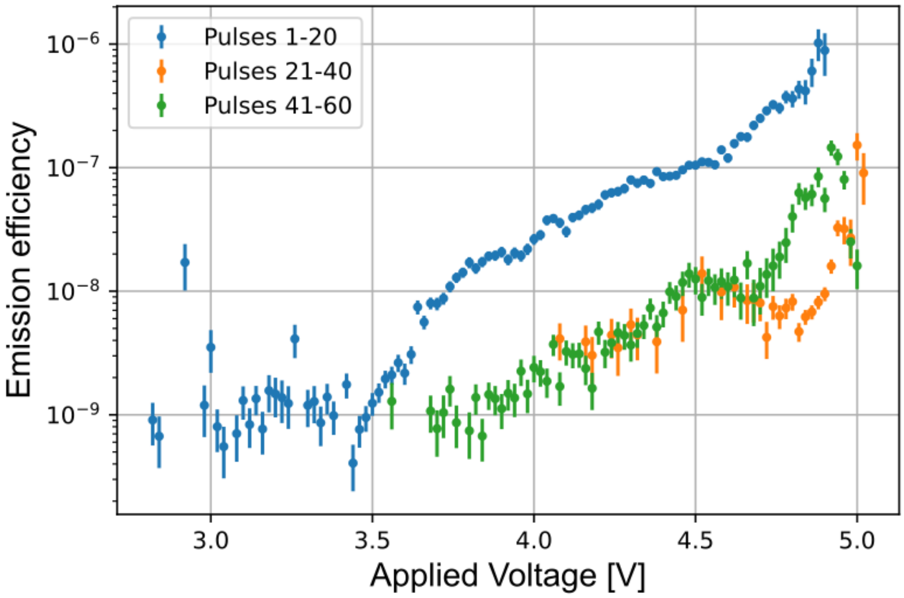

Figure 3.9.: *The mean extracted photon emission efficiency, photons emitted per electron, in function of applied bias for the first, second and last 20 pulses of the pulsed measurement of Figure 3.8. The y-axis is plotted in a logarithmic scale.*

efficiency towards higher voltage in the range of 4 V and 5 V. The onset of the photon efficiency rise starts however around 3.5 V applied to the junction. Below 2.7 V no photons event are detected. This is a considerably higher voltage V and therefore potential electron energy eV than the emitted photon energy observed in the spectra of Figure 3.5. In all the experiments performed on silver-platinum memristive devices no photon emission was detected for voltages below 2 V. The energy difference between the excess energy of the electrons and emitted photons suggests an important inelastic contribution to the radiation process for the silver-platinum memristors. This is in contrast to the wide-gap gold junctions who show light emission for voltages coinciding with the detection limit of the APD at 1.1 eV. This may indicate that different luminescent centers contribute are involved in the electroluminescence of the gold and silver-platinum junctions. Alternatively, the voltage onset observed in the memristive device may just be a coincidence due to experimental settings such as the resistance in series, as potentially only a certain conductance value or device configuration could allow light emission. This would however require further experimental studies, which we did not carry out so far.

3.2.2.2. Current change and light emission

If one looks carefully with smaller time resolution into a single pulse of Figure 3.10 one notices a striking overlap between short and bright photon peaks and current jumps. This is shown in the upper plot of Figure 3.10. Such examples are seen at 50 ms or at 51 ms.

It is even clearer when looking at the normalized current change ratio $\mathrm{R_t} = \mathrm{I_t}/\mathrm{I_{t-\delta t}}$ shown in the lower plot in orange. One observes a consistent overlap between R, deviating from 1, and light emission bursts.

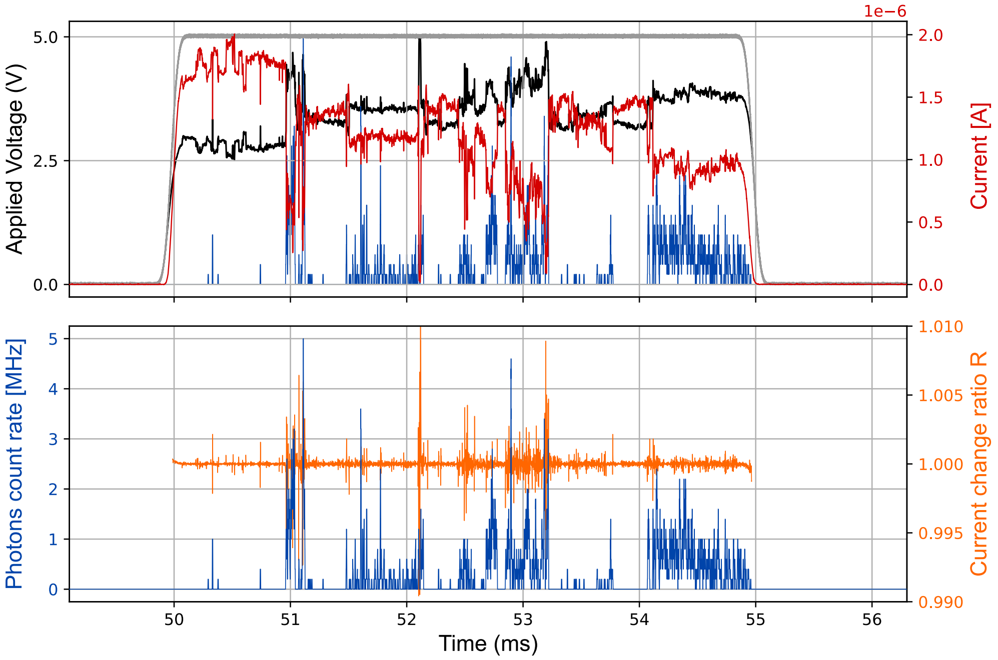

Figure 3.10.: *Details of a single pulse showing the relationship between light emission and current change. In the upper plot, the pulse voltage (gray), the voltage on the memristor (black), the measured current (orange) and the detected photon counts (blue) are shown. The lower plot displays the photon count rates (blue) and the current change ratio R (red). The scale of the photon counts in the upper graph (not shown) is the same as in the lower graph.*

This correlation is also confirmed by the average emission efficiency versus the current change ratio R, displayed in Figure 3.11. The further R deviates from 1, the higher (in average) the photon count rate. The link between current change and light emission was already observed in section 2.7.2 for the wide gap gold junctions, where the current variation was attributed to charge trapping resulting into a conductance path change. This applies also for the silver-platinum memristors and confirms thus the luminescent origin of the emission.

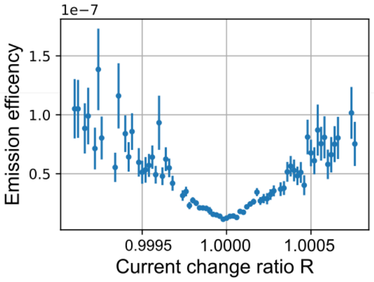

Figure 3.11.: *The average photon emission efficiency versus current change R.*

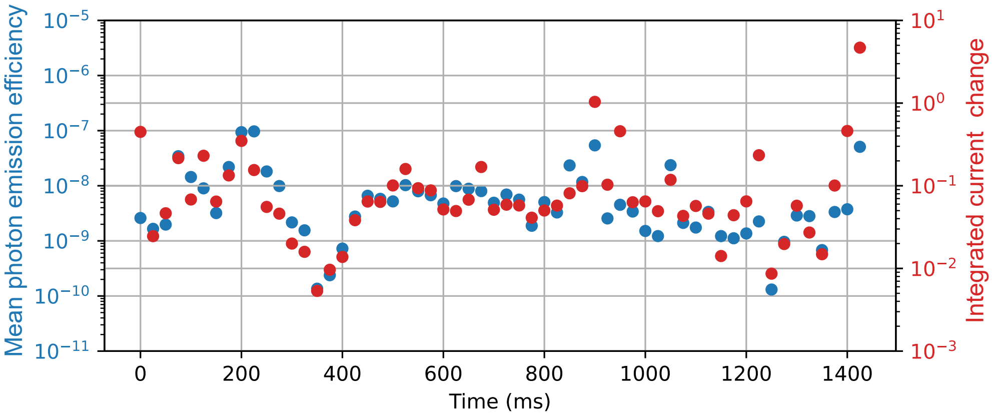

Figure 3.12.: *The figure shows the mean photon yield (blue) and the integrated normalized current variance (red) in logarithmic scale for each pulse of the measurement shown in Figure 3.8. Both curves follow a similar trend over time.*

The importance of current fluctuations and charge trapping for the light emission is particularly highlighted when looking at the averages over all single pulses. This is shown in Figure 3.12, displaying mean photon emission efficiency per pulse and the total integrated current variance (red dots) over each pulse.[3] Strikingly, even without taking into account the voltage dependence on the emission efficiency, one clearly observes that both curves are correlated, showing a higher mean photon yield for pulses with more current variation and vice-versa.

Since photon emission is only possible when luminescent centers are excited by electrons, one can thus conclude that the excitation of these luminescent centers occurs predominantly when the conduction path shows some instabilities. This also would explain the decrease of light emission after many pulses in Figure 3.9 as a result of a stabilization of the conduction path over time. Such stabilization is reasonably associated with the growth of the silver filament, which appears therefore to be detrimental to light emission.

---

[3] The current variance is given by $[\mathrm{R_t}-1]^2$ and is integrated over the whole pulse. We use the current variance instead of the current ratio $\mathrm{R_t}$, because $\mathrm{R_t}$ shows values both above and below 1 and would in average show almost no difference to a constant current pulse.

3.2.2.3. Photon and current blinking

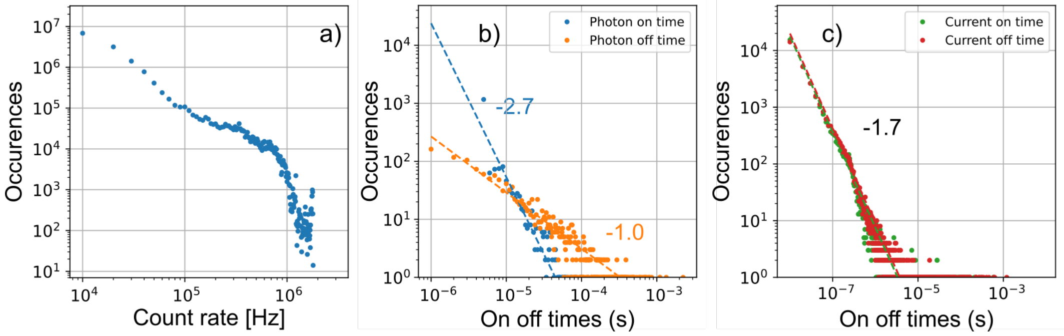

Figure 3.13.: *Photon blinking statistics in silver-platinum memristors. In a) the distribution of detected photon count rates. In b) the distribution of detected photon on and off times, together with the fitted power law (dashed line) and exponents. As a comparison in c) the current blinking with the fitted power law and exponent (-1.7).*

Photon blinking is (quite expectedly) also observed in the silver-platinum memristors, featuring similar characteristics as the wide gap gold junctions. This is summarized in Figure 3.13. In a) the occurences of detected photon count rates shows similarly a broad distribution of grey states, with a fast decaying tail. The shape is similar to what is observed in Figure 2.33 for the wide-gap gold junctions, except for an additional bump at low count rates. In Figure 3.13 b) the distribution of the on and off times for the photon counts are shown. The observation of a power law is in this case not so clear (especially for the off times) as the occurences span a smaller range. Still a power law can be fitted obtaining exponents of -1.0 for the off times and -2.7 for the on times. The former value is closer to what we observed for the wide-gap gold junctions embedded in SiO_2, whereas the latter resembles more the values observed in the measurements for the junctions in air. Blinking is also observed in the current, Figure 3.13 c), where both the on and off times show almost overlapping curves, with an almost identical power law exponent of about -1.7.

These power laws, both in current and photon count rates, although with different characteristic exponents, suggest again that both phenomena are related or modulated by electron trapping, as previously discussed for the wide-gap gold junctions in sections 2.3 and 2.7.3.

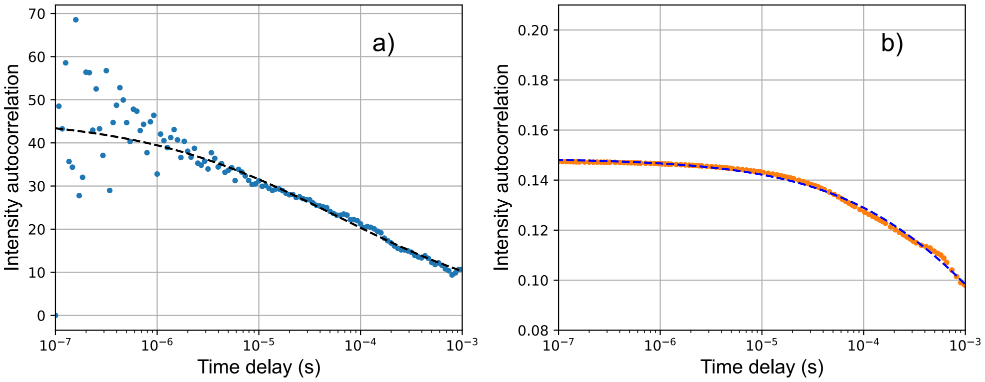

Figure 3.14.: *Photon and current autocorrelation of the measurement shown in Figure 3.8. a) displays the photon autocorrelation with the fitted anomalous difuusion model (dashed line). Similarly in b) the current autocorrelation and its fit are shown.*

	N	τ_a	α
Fig. 3.14 a) Photons	0.022(1)	0.06(1) ms	0.44(2)
Fig. 3.14 b) Current	6.73(1)	3.6(1) ms	0.52(1)

Table 3.1.: *The fitted anomalous diffusion parameters of the autocorrelations shown in Figure 3.14.*

3.2.2.4. Autocorrelation

Inspired by the analysis presented in the previous chapter, the dynamics of light emission are investigated by the photon and current autocorrelation, shown in Figure 3.14 a) resp. b). Both curves can be fitted by the anomalous diffusion model of eq. 2.6. The fit parameters are found in Table 3.1. The anomalous diffusion parameter $\alpha = 0.44$ is similar to the ones inferred for the wide-gap gold junctions in table 2.1. From the plots one observes that the photon and current dynamics are again independent, with 60 times longer active time τ_a for the current than for the photon emission. For the photons the active time τ_a is a factor 7 shorter than observed for the wide-gap gold junctions in SiO_2 under the same excitation conditions. It seems thus that for silver to platinum memristive devices the electron paths to luminescent centers are less stable than for the gold junctions. This is probably due to the improved current switching

characteristics in the silver-platinum memristive devices.
Despite a shorter active emission time, at a given time t the average number of actively emitting centers N is almost the same. The spectra acquired (pulsed) in Figure 3.5 are thus an even greater average over many emitters as for the wide-gap gold junctions in SiO_2 explaining the observed spectral stability.

	Mean detected photon count rate I_{det}	Mean emitter count rate γ_{em}	Mean photon emission time τ_{phot}
Fig. 2.28 a)	15.4 kHz	5.0 MHz	200 ns

Table 3.2.: *The extracted average count-rate and mean emission time of the luminescent centers for the silver-platinum memristors.*

From the average number of emitters N present during the experiment and the mean photon count rate (averaged also over the periods, where no voltage is applied) the average emission rate γ_{em} of an emitter can be estimated. Using equation 2.7 one obtains $\gamma_{\mathrm{em}} = 5.0\,\mathrm{MHz}$ as shown in Table 3.2. This is about one third the emission rate of the wide-gap gold junctions embedded in SiO_2 (15.8 MHz) and gives an upper (average) lifetime limit of 200 ns. This is again compatible both with emission of embedded silicon clusters [97] or silver cluster lifetimes [145] of a few ns.
As the count rate of a single centers depends on too many variables, such as the antenna enhancement of the emission, which cannot extract from our experiments, I believe it is not reasonable to further dwell in the differences of the average emission rate of both structures from the presented measurements.

3.3. Photoluminescence studies of silver-platinum memristive devices

The luminescent species, silicon and silver nanoclusters, can also be optically excited. This allows potentially to further study some of their intrinsic characteristics, such as their lifetimes, and is presented in this section.

Excitation and detection The measurement setup for the photoluminescence experiments is sketched in Figure 3.15. To excite the photoluminescence a diode

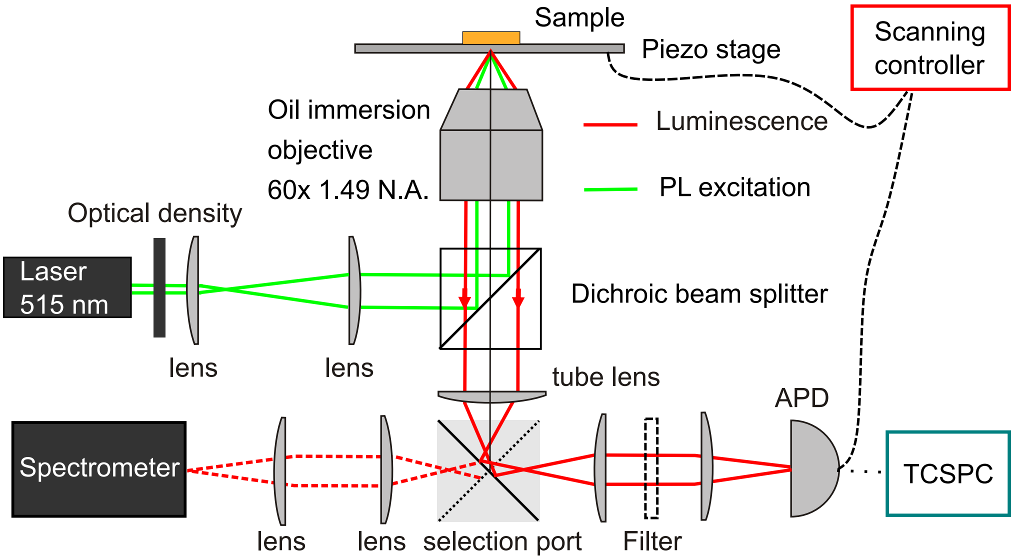

Figure 3.15.: *Sketch of the setup used to excite and measure the photoluminescence of the silver-platinum junctions. Light from a laser at 515 nm (green line) is sent into the inverted microscope, reflected by a dichoric beam splitter and focused by a high NA objective onto the sample. The luminescence is then collected by the same objective (red line) transmitted through the dichroic beam splitter and sent onto a spectrometer or an APD.*

laser emitting at 515 nm is used (Becker&Hickl BDL 515 SMC). This laser provides either continuous emission or short light pulses (about 85 ps duration and 20 MHz repetition rate). Its output power is controlled by an optical density. The laser beam is expanded by a pair of lenses, sent into an inverted microscope and focused onto the sample with a high NA oil immersion objective. The emitted photoluminescence is collected by the same objective and separated from the excitation by a dichroic beam splitter, which transmits only wavelengths longer than 550 nm. By choosing the desired output port, the light is sent to an APD, a camera or a spectrometer. The piezo-electric stage together with the APD (and a scanning controller) allows to perform confocal scans and spatially locate the origin of different luminescent species, as seen for example in Figure 3.16 a). Additional optical filters can be added in the APD's beam path to for example perform confocal scans or lifetime measurements in a desired wavelength range.

3.3.1. Pristine devices

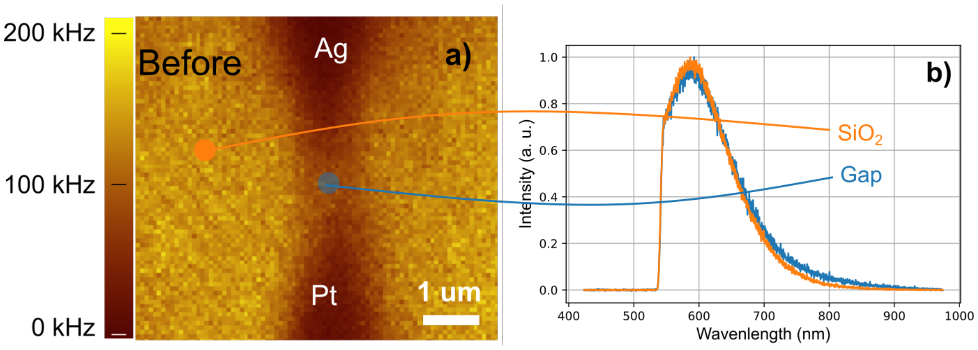

Figure 3.16.: *a) shows a photoluminescence confocal map of a pristine silver to platinum memristive device. b) The photoluminescence spectra normalized to their maxima acquired both in the gap (blue circle) and on SiO_2 background.*

Before any electrical activation of the memristive devices the brightest part of photoluminescence seen in the confocal scans comes from luminescent impurities of the sputtered SiO_2, as displayed in Figure 3.16 a). The dark shadows correspond to the metal electrodes, these act as a filter partially blocking the laser excitation and the transmission of the generated photoluminescence to the objective.

The measured spectra before the electrical activation of the device, Figure 3.16 b), show the same (normalized) shape both for the photoluminescence collected in the gap and on the sputtered SiO_2. The luminescence in the gap is thus emitted by the same native luminescent defects in the SiO_2 layer.

As SiO_2 is a widely used and studied material, there is a rich scientific literature about its luminescent defects, an overview of the reported defects can be found in [94, 146]. Nonetheless, the association of the photoluminescence peak from our measurements is not completely trivial. The main peak observed in our photoluminescence spectra around 600 nm (2 eV), has been attributed in the literature to non-bridging oxygen hole centers (NBOHC) [94, 97, 147]. Alternatively the luminescence can be attributed to oxygen deficiency centers [148] or silicon nano-clusters [97] inside SiO_2. Both emit in the observed spectral range.

XPS analysis

To determine the nature of the pristine luminescence defects we measured the composition of the thermally sputtered SiO_2 using X-ray photoelectron spectroscopy (XPS).

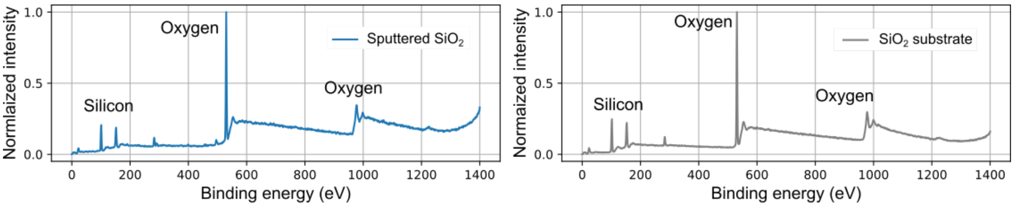

Figure 3.17.: *X-ray photoelectron spectroscopy measurements on sputtered* SiO_2 *(left) and the bare glass substrate (right). The deduced silicon to oxygen ratios are of 29.1 : 70.9 for the sputtered* SiO_2 *and of 33.6 : 66.4 for the glass substrate.*

These measurements reveal an excess of oxygen, see Figure 3.17. This suggests that the observed luminescence from the sputtered SiO_2 is due to NBOHC defects, and not oxygen deficiency centers or silicon nanoclusters, which are both oxygen vacancies.

3.3.2. Electrical stress

Forward bias polarity

After several voltage sweeps a new photoluminescent species appears in the center of the electrode gap, as seen in Figure 3.18. This species shows a complete new spectral feature around 875 nm wavelength. This peak is limited by the detection range of the spectrometer for long wavelengths. According to [94], silicon nano-clusters are the only luminescent defect centers of SiO_2 emitting in the spectral range. This is consistent with an oxygen vacancy creation [67, 149] during the SiO_2 breakdown discussed in 2.3.1.
Alternatively the new photoluminescence features could be explained by few atom silver clusters [150]. These clusters feature an emission spectrum over the whole visible range, depending on their size and structure [106, 150]. Because of the dominant SiO_2 contribution at 600 nm, one may detect only contributions of silver clusters emitting in the range of 700 nm to 1000 nm.

Reverse bias polarity

To further clarify the origin of the defects we performed the same photoluminescence experiments also for devices activated with reversed polarity. Also in this

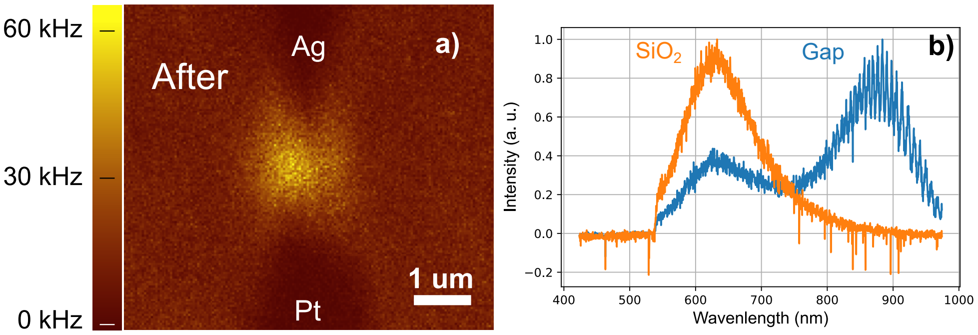

Figure 3.18.: *In a) photoluminescence confocal map taken after electrical activation (forward applied bias) of the same device shown in Figure 3.16. The difference of background count rates between a) and Figure 3.16 a) is due to a different excitation power (1 µW versus 300 nW) and a partial bleaching of the SiO_2 luminescence over time and repeated scans. In b) the photoluminescence (normalized) spectra taken again in the gap (blue circle) and on SiO_2 background after the voltage was applied on the device.*

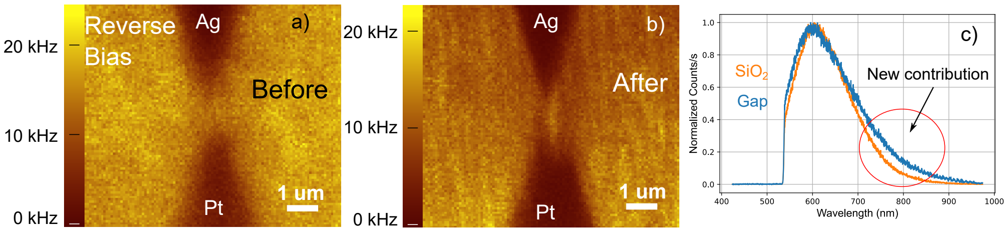

Figure 3.19.: *In a) and b) photoluminescence confocal maps reps. before and after electrical activation of the same device with reverse applied bias obtained using the same laser power of 300 nW. In c) photoluminescence spectra after the electrical activation of the gap.*

case a new luminescent species appears in the gap, see Figure 3.19 after electrical stressing the device. Although not as prominent as seen in the forward polarity, the new species features also a shoulder of increased photoluminescence between 750 nm to 900 nm. We associate thus both luminescent species observed under forward and reverse applied electrical stress to newly created silicon clusters in the SiO_2 matrix. The same luminescent centers are also involved in the electroluminescence of section 3.2.

Lifetimes

To characterize the photoluminescent species further we also looked at their lifetimes. To do measure these, we excite the sample with short laser pulses (85 ps, 20 MHz repetition rate, average power of 300 nW) and connect the APD to the time correlated single photon counting (TCSPC) module, shown in Figure 3.15. The results are displayed in Figure 3.20 a) and b). To select light emitted from the newly created species we additionally filtered the emitted light at the gap by inserting an optical filter centered at 850 nm with a width of 50 nm. The lifetime curves of Fig. 3.20 were obtained on a single device stressed under forward bias. For devices activated with reverse bias the curves are however almost identical. The measured decay curves were fitted by the convolution of a double exponential decay

$$\mathrm{A}_1 \exp\left(-\frac{t}{\tau_1}\right) + \mathrm{A}_2 \exp\left(-\frac{t}{\tau_2}\right)$$

with the instrument response function. The fit of $\mathrm{A}_1, \mathrm{A}_2, \tau_1$ and τ_2 were kindly provided to us by Dr. Aymeric Leray. The obtained values are shown in Table 3.3.

The new luminescent species created by the electrical activation inside the gap shows clearly a longer lifetime in the second exponential decay of 9 ns for the full spectrum, and 8 ns for the filtered spectrum, 4-5 times longer than the

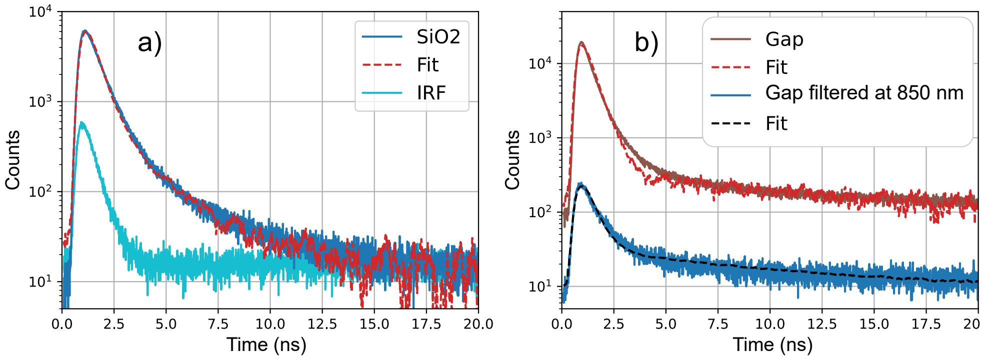

Figure 3.20.: *TCSPC-lifetime measurements of the observed photoluminescence. In a) the lifetime measurement (blue), its double exponential fit (red -dashed) convoluted with the instrument response function (IRF) and the IRF itself (cyan) are shown. In b) the lifetime measurement of the gap luminescence is shown: in blue obtained with 850 nm 50 nm bandwidth filter, in brown without any filter. The dashed lines (red, resp. black) plot again the fitted double exponential decay (convoluted again with the IRF).*

SiO_2	Gap (full spectrum)	Gap (850 nm)
$A_1 = 0.81$, $\tau_1 = 0.19\,\mathrm{ns}$	$A_1 = 0.89$, $\tau_1 = 0.08\,\mathrm{ns}$	$A_1 = 0.55$, $\tau_1 = 0.19\,\mathrm{ns}$
$A_2 = 0.16$, $\tau_2 = 1.94\,\mathrm{ns}$	$A_2 = 0.11$, $\tau_2 = 9.16\,\mathrm{ns}$	$A_2 = 0.45$, $\tau_2 = 7.93\,\mathrm{ns}$

Table 3.3.: *The extracted fit parameters for the measurements of Figure 3.20.*

2 ns measured for the luminescent defects in SiO_2. The spectral filtering clearly increases the weight of the longer decay component, it is therefore more than reasonable to associate the longer decay component to the newly created species in the gap.

The lifetimes of the native SiO_2 luminescent centers of 0.19 ns and 1.94 ns are magnitudes of shorter then what is reported in literature of 15 µs for NBOHC [94, 148] and 200 ns for oxygen deficiency centers [148]. This might be due to a different measurement technique looking for longer lifetimes and probing therefore only long-lived triplet states, as shown in [151] for silver nanoclusters embedded in glass.

The reported lifetimes of silicon nanoclusters [97] (1 ns up to 28 ns) are consistent with our measured lifetimes and supports therefore our identification of the electrically-induced luminescent defects with silicon nanoclusters.

3.4. Conclusion

This chapter presented the light emission of silver-platinum memristive devices. By their structure these devices are similar to the wide-gap gold junctions studied in the preceding chapter, this reflects in a similar current and photon generation behavior.

These memristive devices, as the gold junctions, show under electrical stress a history dependent switching from a high resistance state to low resistance state. For a positive (forward) voltage on the silver electrode, the switching is due to a combination of silver filament growth and the creation of SiO_2 defects leading to a higher junction conductance, whereas for a negative (reverse) voltage on the silver electrode only the latter mechanism contributes.

Under both forward and reverse electrical voltage the memristive junctions emit light featuring a similar spectral range and shape for both polarities, similar also to the wide-gap gold junctions. Because of this symmetry under the polarity of the bias, we attribute the electricaly generated light to the electroluminescence of defects in the SiO_2, more in particular silicon clusters. The spectra are once again shaped by the resonances induced by the electrodes.

The dynamic behavior of the light emission in the memristive junctions (forward bias) however reveals quite marked differences with the wide-gap gold junctions. The photon emission is not continuous but rather features bright emission periods correlated with current fluctuations separated by periods with no photon radiation. This is attributed to the possibility of electrons to access luminescent centers when the electron conduction involves also the SiO_2 defects and the current is unstable. Also the voltage required to generate photons are consistently higher than the 1.1 V required for the wide gap gold junctions, which suggests that different luminescent centers for the gold and the silver-platinum junction are at play.

The creation of the luminescent centers involved in the electrical light emission was also confirmed in photoluminescence experiments. Once again the independence on the voltage polarity and their spectral characteristics leads to identify these centers as silicon nanoclusters embedded in SiO_2. Further the lifetimes of these new species of a few ns is consistent with the values of silicon clusters reported in literature.

From the discussion of this chapter it seems that the growth and electron conduction through a connected silver filament is detrimental to light emission. Paradoxically, when further increasing the filament growth light emission is still observed, although with different characteristics. This will be discussed in chapter 6 studying the behavior of silver to silver junctions embedded in PMMA.

Chapter 4.

Overbias light emission in electromigrated gold constrictions

When the gaps are almost closed, a new light emission mechanism may be observed, the so called overbias photon emission. This mechanism distinguishes itself fundamentally from the previously discussed mechanism of inelastic electron tunneling and electroluminescence as photons with energies greater than the standard limit of inelastic tunneling (eq. 2.3) are emitted. This limit corresponds to the maximum kinetic energy of a single electron. Overbias emission is thus a multi-electron process and shows generally a nonlinear dependence in the current [40, 43].
This overbias emission is obtained here in gaps created by electromigration of small gold constrictions [40]. This source will be presented first before to review the different hypotheses of overbias photon radiation.

4.1. Electromigrated gold constrictions

4.1.1. Small gaps to observe overbias light emission

Since the overbias emission depends nonlinearly on the current flowing through the gap, it is not surprising that this regime is typically observed in junctions with rather high current densities and a conductance close to the quantum of conductance $\mathrm{G}_0 = 7.75 \times 10^{-5}\,\mathrm{S}$ [40, 42, 43]. A conductance of G_0 indicates the presence of conductive bridge between both electrodes with the thinnest part being one atom thick [152]. In the following of our discussion I will discuss the measured conductance in units of G_0.
To obtain planar gaps with such a conductance is not straightforward. The fabrication of metallic connections of few (less than 10) atoms thickness or small gap sizes below 1 nm is not achievable by using solely traditional clean

room fabrication techniques such as e-beam lithography or focused ion beam milling [153, 154]. These techniques are typically limited to some feature sizes of a few nm. Fabricating junctions with a conductance close to G_0 therefore requires additional fabrication steps.

One solution to access the overbias emission regime is to approach, put in contact and retract an electrically contacted metallic tip on a metallic substrate [155–157], as is done in the STM community. While retracting the tip, the measured conductance transitions continuously from above G_0 to values below G_0. By properly controlling the retraction one can attain the desired junction conductance value [157].

A conceptually similar approach is implemented in mechanical break junctions, where a substrate with a thin metal constriction on top is bent mechanically in such a way to stretch the gold until the deformation leads to the opening of a small metal gap [158, 159]. In this process a gap forms and the junction conductance transitions from conductances above G_0 to below G_0. By releasing the mechanical stress on the substrate, the newly created gap typically closes, and the device can be recycled several times.

However, using a tip or relying on the mechanical deformation of a substrate is hardly practical for applications having several devices (with possible different orientations) on a single chip. Through the electrical current induced mass migration (electromigration) [160, 161] in small metallic constrictions small gaps can be fabricated [40, 162].

These electromigrated constrictions will be discussed here in the following.

4.1.2. Sample fabrication

The gold constrictions are fabricated following the procedure explained in section 2.1, typically with 2 nm of titanium and 25 nm of gold. A typical constriction is shown in Figure 4.1

The focus of the electron beam fabrication is to make the central constriction as small as possible. This insures in my experience an easier and better electromigration process. The size of the constriction is reflected in the total resistance, the smaller the constriction the higher the resistance. Typical initial resistances (for the whole circuit, including the contact electrodes and tungsten tips) achieved in were in the order of 200 Ω.

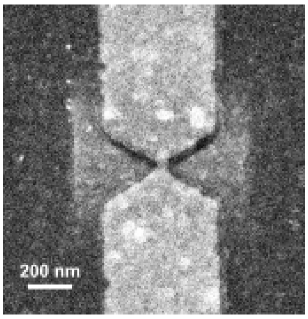

Figure 4.1.: *SEM image of a fabricated gold constriction.*

4.1.3. Electromigration

Electromigration is the mechanical deformation of conductors induced by an electrical current, which is essentially caused by electrons scattering with impurities inside the lattice [160,163]. This scattering results in a momentum transfer to the lattice and a subsequent dislocation of impurities, which leads to a deformation of the conductor and finally its rupture. This is a well-known issue for electrical interconnects of integrated circuits [160,163,164].

However when monitored carefully, electromigration can be used to create gaps with sub-nm separations [40,81,162].

In my case, the electromigration is performed with the sample already installed on an inverted microscope. The constriction under study is connected to a voltage source and the trans-impedance amplifier (TIA) measures the current.

For the controlled electromigration of the constriction a DC voltage (typically up to 3 V) plus a small AC component is applied [165]

$$V = V_b + V_{AC} \cos(\omega t)$$

The AC component of the voltage, with an amplitude of about 10 mV and a frequency around 4 kHz, allows to monitor the dynamic resistance of the constriction through a Lock-in measurement (Lock-in UHFLI/HF2LI Zurich instruments) of the corresponding AC part of the current. In parallel also the DC-current flowing through the junction is monitored.

Gap creation by electromigration To create small gaps with a resistance close to $1/\mathrm{G}_0 = \frac{h}{2e^2} = 12.9 \cdot 10^3\ \Omega$, the constriction should break at low voltages, ideally below 1 V. This limits the power dissipated at the constriction, leading otherwise to a catastrophic failure of the constriction and large gaps.

To localize the gap formation a thin constriction within the structures is fabricated, see Figure 4.1. A higher resistance typically facilitates a controlled electromigration process. This is probably due to several factors. First, a higher resistance of the constriction implies a thinner constriction. Therefore less material needs to be removed through the electromigration. Second, as there is a residual contact resistance to the constriction acting as a passive voltage divider, for a fresh device the applied voltage is only partially dropped on the constriction. For lower constriction resistances one needs therefore to apply a higher voltage to initiate the electromigration. High voltages are however quite critical as the constriction can suddenly break. This is due to a self reinforcing cycle: once material from the constriction is removed, the resistance of the constriction

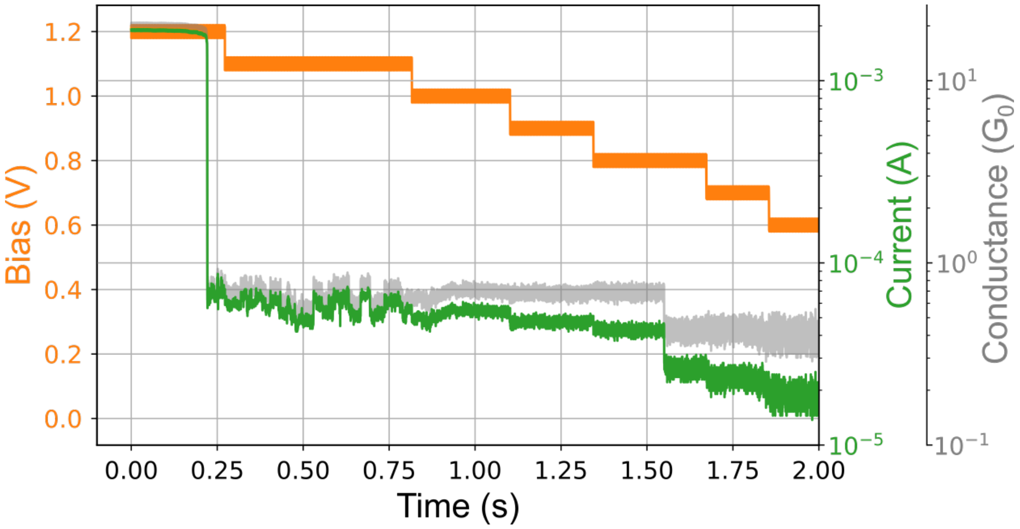

Figure 4.2.: *The final stages of the electromigration process of a small gold constriction resulting in the opening of a gap is shown. In orange the applied bias, in green the measured current (in a log scale), in gray the resulting conductance (in units of* G_0*). At time 0.24 s the current drops one order of magnitude due to the gap creation inside the constriction.*

increases and consequently the fraction of power dropped on the constriction. This leads to an even faster resistance increase which again increases the power dropped by the electrons on even thinner constriction and so forth.

The migration process is started by increasing the DC bias until the measured dynamic conductance decreases (typically between 2 to 3 V). Especially at high applied biases the DC bias needs to be reduced rather quickly for relative small resistance increases.

The initial objective of the electromigration process is to lower the applied voltage while still observing electromigration of the constriction, seen in a conductance decrease. This is usually the most critical and longest step in the electromigration process. Especially at the beginning of the electromigration, the conductance behavior of the constriction is not predictable. Typically, the power dissipated at the constriction leads to a local temperature increase which decreases its conductance. Sometimes however, a increase of the conductance is observed instead. This increase might be caused by water desorption or by an induced thermal annealing of the constriction [165]. The latter step reduces grain boundaries and impurities in the metal resulting in a conductance increase.

Once the electromigration is stable and a constant increase of resistance at voltages around or below 1.5 V is observed, reaching low breaking voltages and creating small gaps is almost guaranteed.
An example of a formed tunnel junction by breaking a constriction is shown in Figure 4.2. Initially for an applied bias of 1.2 V (green curve) we observe current of 200 mA. Over time the current decreases slightly until around the time 0.24 s, were we observe suddenly a large jump in the current, which decreases to about 100 μA. The conductance (gray curve) decreases to about 0.7 G_0. The junction is thus in the tunneling regime. At the time 1.6 s we observe an additional conductance jump to about 0.5 G_0. This underlines how fragile such a tunnel junction exposed in air is.

4.1.4. Overbias photon emission

Concomitant with the creation of the gap light is emitted, as shown in Figure 4.3. This bright photon emission, occuring at voltages below 1.1 V down to 0.8 V, proofs that overbias emission is observed in the electromigrated gold constriction, as according to eq. 2.3, the applied voltage would only allow to

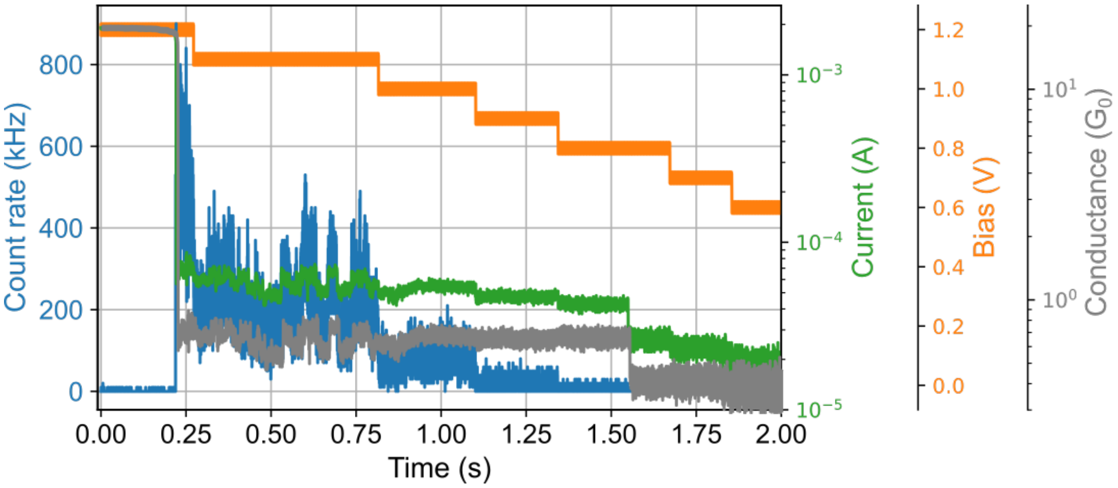

Figure 4.3.: *Photon emission during the electromigration of a gold constriction, for the same measurement shown in Figure 4.2. In blue the detected photon counts, in orange the applied bias, in green the measured current (log scale) and in gray the resulting conductance.*

emit photons having energies below the APD's detection range.
The detected photon count rates depend both on the applied voltage and the current, as is seen in at 0.27 s showing a concomitant voltage and photon count drop and in between 0.5 s and 0.75 s, where for a constant applied voltage, the measured current and photon counts increase and decrease together.
Although not observed in Figure 4.3, light emission from the constriction is also sometimes seen even before the opening of a gap [42], when the conductance equals a few G_0. This emission increases in intensity as the conductance approaches towards G_0.

Spectra

The overbias photon emission is reflected also clearly in spectra acquired for a constant applied electrical voltage, as shown in Figure 4.4.
The spectra of Figure 4.4 a) show a broad peak, with a fast increase starting around 700 nm, whereas for long wavelengths (950 nm) the detected photon counts decrease due to the efficiency cut-off of the detector. These spectra are

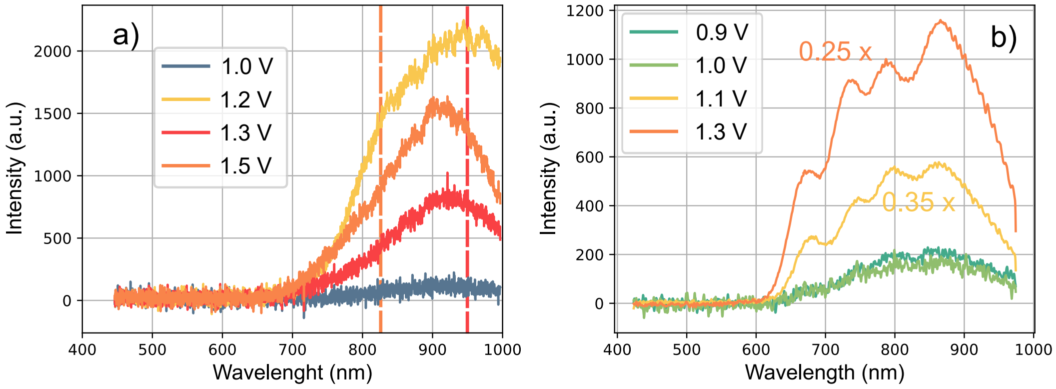

Figure 4.4.: *Two series of spectra from two different electromigrated constrictions. In a) for a thicker gold constriction (5 nm chromium and 50 nm of gold) in b) for a thinner one (2 nm of titanium and 25 nm of gold). Additionally in a) the standard limit of inelastic tunneling is indicated for 1.3 V (954 nm) and 1.5 V (826 nm) by dashed lines. For applied voltages of 1.2 V and below, the limit lays outside the spectral measurement window. For a better readability in b) the spectra acquired at a constant voltage of 1.1 V and 1.3 V have been downscaled by a factor of 0.35 resp. 0.25.*

obtained from an electromigrated constrictions with slightly thicker metal layers (5 nm chromium, 50 nm of gold). Except for the spectrum at 1.2 V, the light intensity increases with higher applied voltage and seems to slightly blue-shift. To deduce a dependence is however difficult as the junction modified its conductance during the spectral acquisition, such a study is found in [40] confirming the previously mentioned trends.
In Figure 4.4 b) (for a junction with 2 nm of titanium and 25 nm of gold) similar spectral characteristics are observed, a broadband spectrum with a rise in photon counts around 600 nm spanning the whole range until the detection efficiency drop at long wavelengths. Additionally one distinguishes the presence of 4 overlapping peaks. Similarly, spectra taken at higher voltages show consistently a higher photon emission. The presence of multiple peaks in the overbias emission has also been observed in [157,166,167]. In [166] this presence was attributed to plasmon resonances of the junctions. These peaks were shown to be absent when using a thicker chromium adhesion layer, attributing this lack of peaks to the plasmon damping of the chromium adhesion layer. Still the similarity with the electroluminescent spectra of the wide-gap junctions in Figure 2.23 c) is quite surprising. This could indicate that these peaks may be originated by electronic transitions, as for example in small gold clusters possibly created during the electromigration process.

4.2. The origin of overbias light emission

Hypotheses explaining the emission mechanism found in scientific literature can be regrouped into two categories: light emission by or involving an out of equilibrium hot electron bath [40, 42, 55, 168] or coherent multi-electron inelastic tunneling [43,156,169]. In the following these will be discussed in greater detail.

4.2.1. Thermal radiation by an out of equilibrium hot electron distribution

Already in 1988 overbias emission observed in discontinuous gold films was explained by thermal radiation [55]. Because each gap has an electrical resistance R_{gap}, by applying a bias V an electrical power of $\frac{V^2}{R_{\text{gap}}}$ is dissipated in the junction. This power is carried by electrons tunneling from the source electrode into the drain electrode.
As most of the electrons tunnel elastically through the gap, the electrons flowing

into the drain electrode have an excess energy of eV compared to the initial local equilibrium distribution of electrons. The electron-electron scattering between these energetic electrons and the electrons present in the drain, leads to a local redistribution of the electron energies, creating a more energetic electron distribution or a hot electron bath. Usually this electron bath dissipates its energy through electron phonon scattering to the lattice leading to a general increase of the local (lattice) temperature but without any photon emission detectable in the visible. When the dimensions of the drain electrode are small (below 100 nm), electron-phonon scattering is however reduced, this allows to reach higher temperatures of the electron bath whose energy is partially released as light [40, 42].

Hot electron distribution

As the interactions and energy transfer among electrons is faster (a few 100 fs) [170–173] than between electrons and phonons (about 1 ps) [174, 175], one can model the electron energy distribution as a thermal bath with its own electron temperature $\mathrm{T_e}$, which is in general different from the temperature of the phonon bath $\mathrm{T_{ph}}$. This is the so called two temperature model, widely used in the nonlinear photoluminescence of metals for ultrafast pulsed excitation, see also Chapter 5.

Such a two temperature model has also been developed in [40, 176] to explain overbias light emission as a thermal radiation from the hot electron bath. The main difference is that the model does not assume a temporal relaxation of the electron bath temperature, but a spatial relaxation of the hot electron temperature in the drain electrode.

To predict the electron temperature $\mathrm{T_e}$, the model further assumes that in electromigrated tunnel junctions the electron scattering at edges is predominant over electron phonon scattering, meaning that the electrode dimensions are smaller than the electron phonon interaction length (about 1.1 µm [175]). Such small structures have been observed on SEM images of such junctions [176]. The highest electron temperature predicted by the model is given by:

$$k_\mathrm{B}\mathrm{T_e} = \sqrt{(k_\mathrm{B}\mathrm{T_{ph}})^2 + \alpha IV} \simeq \sqrt{\alpha IV} \tag{4.1}$$

where $\mathrm{T_{ph}}$ is the lattice temperature, k_B the Boltzmann constant, I, V the current resp. the bias at the junction. In the approximation of equation 4.1 the lattice temperature is neglected, which is valid for high temperature differences. α is a parameter taking into account the interaction between electrons and the electronic thermal conductivity. A similar model has been derived in [177] and applied to light emission from electromigrated graphene tunnel junctions.

Light emission by a hot electron bath

As any object at finite temperature which interacts with light, a hot electron bath radiates light according to Kirchhoff's Law. Kirchhoff's law has been extended and shown to be valid also for nanoscale and nonequilibirum systems [178]. The thermally radiated light at a given frequency (and wavevector) $P_\mathrm{e}(\nu, T)$ is for all bodies proportional to their absorption at the same frequency $\alpha_\mathrm{abs}(\nu)$:

$$P_\mathrm{e}(\nu, T)\, d\nu = \alpha_\mathrm{abs}(\nu) \cdot B_\mathrm{P}(\nu, T)\, d\nu \tag{4.2}$$

with $0 \leq \alpha_\mathrm{abs}(\nu) \leq 1$ and $B_\mathrm{P}(\nu, T)$ is the universal (temperature dependent) proportionality function equal to Planck's law:

$$B_\mathrm{P}(\nu, T) = \frac{2h\nu^3}{c^2} \frac{1}{e^{\frac{h\nu}{k_\mathrm{B}T}} - 1} \tag{4.3}$$

The spectra of thermal blackbody radiation at different temperatures according to eq. 4.3 are plotted in Figure 4.5. For a better comparison with experiments the spectra have been multiplied by a (idealized) detection curve having an efficiency decrease for longer wavelengths which is shown in the inset. These spectra resemble to the overbias spectra of Fig. 4.4 a).

The frequency dependence of the absorption coefficient $\alpha_\mathrm{abs}(\nu)$ in equation 4.1 allows additionally to account for the spectral resonances observed in Fig. 4.4 b). These resonances can be either induced by electronic states coupling to light (e.g. in molecules) or induced by local optical resonances (plasmonic gold nanoparticles).

As the electron temperature according to equation 4.1 does not depend on the applied voltage alone but also on the electron current, the same spectra can be obtained for different applied voltage and overbias photon are predicted. Using this model in [40], typical electron temperatures between 1000 K to 2000 K were fitted to the observed overbias spectra.

Additionally the model predicts a power law behavior of the detected photon counts $I_\mathrm{p}(\nu, T_\mathrm{e})$ at frequency ν in function of the applied electrical power as [40]:

$$\log(I_\mathrm{p}(\nu, T_\mathrm{e})) = \log(D(\nu)) - \frac{h\nu}{\sqrt{\alpha IV}} \tag{4.4}$$

where $D(\nu)$ is a prefactor taking all the temperature independent spectral components into account. This $\sqrt{IV}$ dependence has been observed several times in

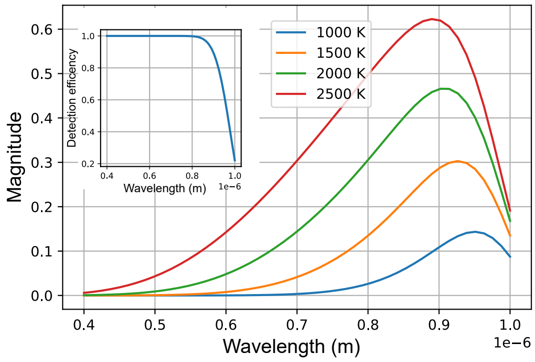

Figure 4.5.: *Blackbody spectra at different temperatures according equation 4.3 multiplied with an idealized detection efficiency showing an efficiency drop at long wavelenghts (shown in the inset). For an easier visibility of all spectra in the same graph, the spectra have been normalized by their spectral intensity at 1100 nm, this normalization ensures that the spectral intensity is higher for higher temperatures.*

electromigrated constrictions [40, 166, 167].

From the Stefan-Boltzmann law of thermal radiation, the total radiated power emitted by the junction should follow a quadratic dependence on the electrical power dropped on the junction (neglecting spectral resonances):

$$P = \sigma^* T_{\mathrm{e}}^4 \simeq \sigma^* \left(\alpha I V\right)^2 \tag{4.5}$$

where σ^* is a modified Stefan Boltzmann constant taking into account the finite area and a mean absorption coefficient α_{abs}. Such a quadratic dependence has been observed in overbias STM emission spectra for constant applied voltage but varying current intensities in [179].

One may naively consider that thermal radiation might be a slowly modulable process. The thermal temperature decay of hot electrons is however fast in the order of only a few ps [180, 181], allowing potentially up to THz modulation speeds of the light source.

4.2.1.1. Light emission from inelastic tunneling or plasmon decay into a hot electron bath

Two slightly different approaches from the direct thermal radiation of the hot electron bath have been proposed [168, 179]. In [179] inelastic tunneling into the hot electron bath is considered. The energetic distribution of hot electrons leads to a thermal broadening of the strict inelastic tunneling limit allowing thus a partial overbias emission of the inelastic tunneling process. It is to be noted that in [179] the deduced electron temperature difference is quite weak, typically below 60 K, and the detected overbias emission fraction is spectrally quite small. In [168] among other models to explain overbias light emission, inelastic electron tunneling exciting a surface plasmon, decaying into electron-hole pairs whose recombination leads to light emission is proposed. As in the previous case, because of the hot electron bath distribution, the electron hole pair decay can lead to light emission having greater energy then the tunneling electron itself.

4.2.2. Coherent multi-electron inelastic tunneling

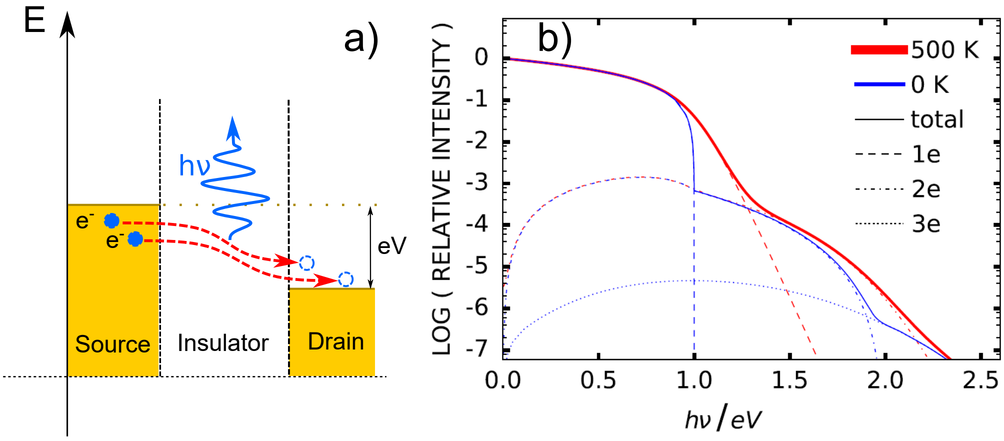

Figure 4.6.: *In a) sketch of a coherent two electron inelastic tunneling process, showing two electrons tunneling from the source to drain electrode whilst emitting a single photon. In b) plot of the theoretical predicted photon emission rates for inelastic electron tunneling at* 0 K *and* 500 K *with the contribution of single and multiple electron tunneling shown in dashed lines. Figure b) reprinted from [43] © 2017 by the American Physical Society.*

The other approach to explain overbias light emission is to invoke coherent multi electron interactions in the tunneling process [43, 169, 182]. As illustrated in Figure 4.6 a), in this hypothesis two electron tunneling together emit a single photon. Since the available energy to create a photon is now doubled, the quantum cut-off for the emitted photons is pushed to $2\,eV$, i.e. twice the cut-off for single inelastic tunneling. By considering N electrons interacting and emitting a single photon the limit is pushed to $N\, eV$.

As for second or third harmonic generation process in optics, the creation of a single photon from the interaction of two or three photons, the photon emission by coherent multiple electron tunneling is proportional to a power law of the current, which reflects the number of electrons involved; i.e. for two electron inelastic tunneling the emitted photon count rates I_{ph} is proportional to the square of the electric current I_{e} [43, 169]:

$$I_{\mathrm{ph}} \propto I_{\mathrm{e}}^2$$

This would naturally explain the observed quadratic power law observed in [179] for the overbias photon emission.

The predicted spectrum (without any resonances) of the photon emission involving single and multiple electron emission processes is sketched in Figure 4.6 in a semi logarithmic plot. At low temperatures (0 K) the model shows a sharp transition between single electron inelastic tunneling and two-electron inelastic light emission. Around the standard limit of inelastic tunneling $\frac{h\nu}{eV} = 1$, one observes a sharp drop in photon count by two order of magnitudes as the two electron emission process is the only left for photon emission. At higher temperatures these sharp transitions at $\frac{h\nu}{eV} = 1,\ 2,\ \ldots$ are smoothed due to thermal broadening.

Such kinks in the spectra indeed have been observed in [43] for the overbias emission for a STM controlled silver tip on top of a smooth silver surface in ultrahigh vacuum cooled at 6 K.

Additionally, in [156] the observed power law dependence $\propto (IV)^{-0.5}$ of equation 4.4 for light detected at a given wavelength has been reproduced by invoking coherent multi-electron inelastic tunneling model with the three electron interaction.

4.2.3. Photon correlation measurement of overbias emission

Both hypotheses, the incandescence from a hot electron bath and the coherent two electron tunneling, can explain all the experimental observations so far. The origin of the overbias light emission remains thus debated.

Whereas overbias emission obtained using STM tips tends to be explained by multi-electron processes, overbias emission obtained in electromigrated constrictions is typically explained by hot electron emission. The overbias emission in the two structures might be indeed different since the two experimental systems are not the same. For the hot electron emission model small drain electrode

dimensions are required to decouple the electron and phonon bath sufficiently and allow high electron bath temperatures. These small feature size might be naturally obtained in the electromigration process, not however for the STM tips, which show overbias emission by the multi-electron process instead.
Still, one would like to experimentally differentiate between both emission mechanism for the overbias emission in the electromigrated gold tunnel junctions, as both theories explain the spectral and photon emission properties observed in experiments and presented so far.
To attempt such an experimental distinction one objective of this thesis was to measure the second order photon correlation of the overbias emitted light as will be detailed in 5.2.2. This goal finally results to be too ambitious for the present thesis work.

4.3. Conclusion

This chapter discussed a new light emission mechanism in small gap junctions: the overbias photon emission. This regime requires rather large current densities typical to small gaps, with a junction conductance close to the quantum of conductance G_0. Among other devices and configurations, such conductances are achieved in carefully electromigrated gold constrictions. The fabrication of these devices were presented in greater detail together with their overbias photon emission.
In the second part two possible mechanism of the overbias radiation were discussed: the creation of a hot electron distribution in the drain electrode, emitting light by thermal radiation, or coherent multi-electron interactions in the tunneling process shifting leading to overbias photon emission. Both hypotheses are able to explain the so far reported experimental observations.
The desire to distinguish in between both hypotheses motivates the photon correlation measurements of the next chapter.

Chapter 5.

Photon correlation measurement of the nonlinear photoluminescence generated in metals

In this chapter my photon correlation measurements on the nonlinear photoluminescence in small metallic structures are presented. These measurements are intended as an intermediate step to further investigate the overbias emission of electromigrated tunnel junctions of chapter 4. As mentioned therein, measuring the photon statistics of the overbias emission might help to distinguish between the different overbias hypotheses (thermal radiation or two-electron tunneling). The choice of first studying the photon correlation of upconverted photons released by metals instead of the overbias emission from gold nanowires is motivated by experimental constraints. Both the nonlinear photoluminescence and the overbias emission share many similarities and can both be explained by a hot electron radiation. Compared to the overbias photon emission of electromigrated nanowires, the nonlinear photoluminescence of metals is both more stable and brighter, allowing therefore to measure for longer time, while the required integration time is shorter. Because I first sought to understand the intricacies of photon correlation measurements, it seemed reasonable to start with an easier version of the measurement.

The main results of this chapter are published in [44]. Here I will discuss some aspects of the photon correlation measurements in greater detail.

5.1. Photoluminescence in metals

Before discussing the photon correlation measurements, I will present the photoluminescence of metals in greater detail.

When we usually think about light impinging on metals, we typically think about reflection if we consider large flat surfaces or scattering for small particles.

Nonetheless metals show also photoluminescence, and emit photons in a broad spectral range. These photons have typically a lower energy than the incoming photons (downconversion), however at sufficient excitation powers photons at higher energies are also observed (upconversion).

5.1.1. Optical setup

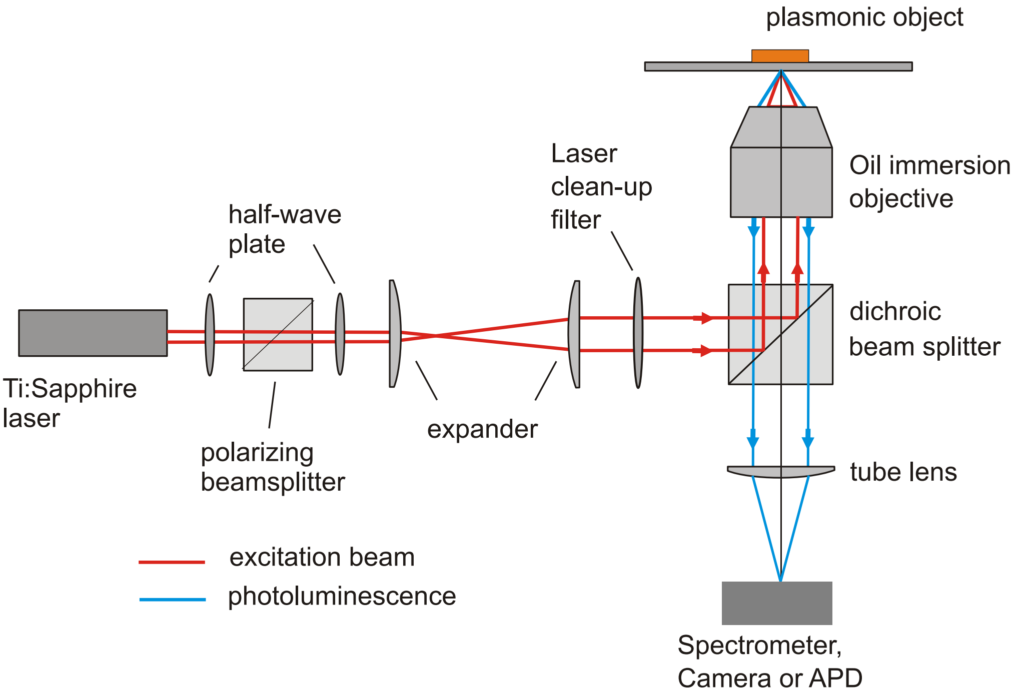

Figure 5.1.: *Sketch of the setup used for the photoluminescence measurements. The red lines indicate the path the excitation beam, the blue lines indicate the collection path of the emitted photoluminescence.*

The setup to excite the photoluminescence in metallic structures, is sketched in Figure 5.1. It resembles quite to the one shown in Fig 3.15 used for the confocal PL scans in Chapter 3. The main difference is that, to also excite the upconverted photoluminescence, a nonlinear ultra short pulsed Ti:Sapphire laser (Chameleon, Coherent, Inc., 180 fs pulse width, 80 MHz repetition rate) with tunable wavelength range is used. In all the measurements presented in this chapter an operating wavelength of 808 nm was chosen. At this wavelength the laser provides the highest power output. To control the power sent on the structures, the laser beam is sent through a half waveplate and a polarization beam splitter. A second half waveplate allows to tune the polarization of the beam independently.

The laser beam is expanded by two lenses in a telescope configuration, to overfill the objective and obtain a diffraction limited excitation spot, and then filtered by a narrowband spectral line-filter at 808 nm (Chroma, Inc.) to remove residual laser luminescence. The beam is then sent to the entry of an inverted microscope (Eclipse, Nikon). Inside the microscope the beam is reflected by a dichroic splitter and focused through an high NA immersion Oil objective (100x, 1.49 numerical aperture, Nikon) onto the sample.

The emitted photoluminescence is collected by using the same objective and transmitted through the dichroic beam splitter. The dichroic, however, transmits only light at wavelengths shorter than 700 nm. To detect light at longer wavelengths the dichroic beam splitter is replaced by 50/50 beam splitter (Thorlabs) and two notch filters at 808 nm (2 nm width, Chroma, Inc.) are inserted into the beam path.

The collected luminescence is then sent to various instruments (camera, spectrometer or APD) or onto the photon correlation measurement setup shown below in Figure 5.8.

Again the combination of a piezo stage and an APD allows to perform confocal scans of the sample and position the excitation beam on a particular nanoparticle or a local emission hotspot.

Spectra

The luminescence of metals is observed in different geometries, material qualities, and is shaped by optical resonances. Such a variety of structures is investigated in the photon correlation measurements. To illustrate the photoluminescence of metals, here (only) the spectrum of a thin layer (2 nm titanium, 25 nm of gold) is shown, see Figure 5.2. The thin layer is excited at 808 nm with an input power of $1.37\,\mathrm{MW\,cm^{-2}}$ and integrated over 30 s. The spectrum shows both the upconverted (for wavelenghts shorter 808 nm) and the downconverted (wavelenghts longer 808 nm) part of the photoluminescence spectrum. In this case a 50/50 beam splitter in combination with two notch filters is used to capture the spectrum also at long wavelengths.The spectrum features an increase of intensity towards longer wavelengths until it decreases at 900 nm limited by the detection efficiency. Still the intensity of down converted photons is higher than of the upconverted photons. The yellow part of the spectrum is

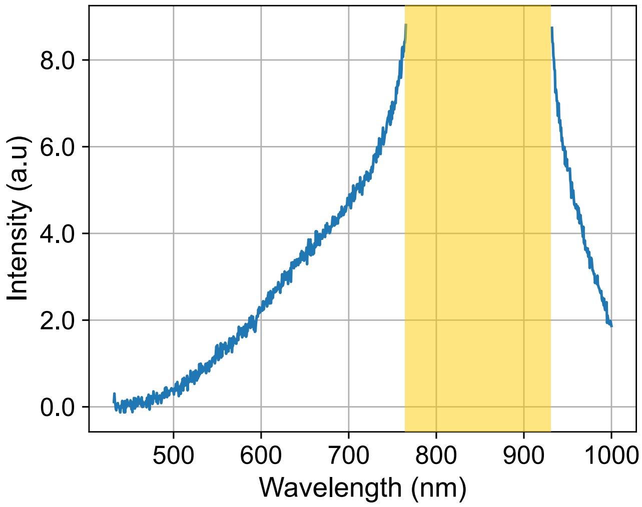

Figure 5.2.: *The figure shows the photoluminescence spectrum of a thin thermally evaporated gold film. The yellow part of the spectrum is removed due photoluminescence contribution coming from the glass substrate.*

removed due to background photoluminescence of the glass substrate [183] whose origin is not entirely clear to me (but most likely due to raman scattering or photoluminescence). In the next sections I will discuss the different mechanism of the down- and up-converted luminescence.

5.1.2. Mechanism of the linear photoluminescence in metals

To explain the linear photoluminescence (down converted photons) different approaches exist. These are sketched in Figure 5.3 and presented in the following paragraphs.

Interband transitions The first observation of luminescence in gold and copper in [184] was explained by electronic interband transitions [185]. In this model, Figure 5.3 (a), an incoming photon is absorbed inside the metal by promoting an electron from the energetically lower lying d-band to the conduction band. This leaves a hole (an electron vacancy) inside the d-band (indicated by (1) in the Figure). The hole can then be filled by an electron transitioning from the conduction band to the d-band (2), which at the same time releases a photon (at lower energy).

In gold, the interband transitions between the d-band and the conduction band have however a gap of 1.8 eV (688 nm) and 2.3 eV (540 nm) [100,185], this mechanism can therefore not account for the luminescence excited with photons of 1.53 eV (808 nm) energy.

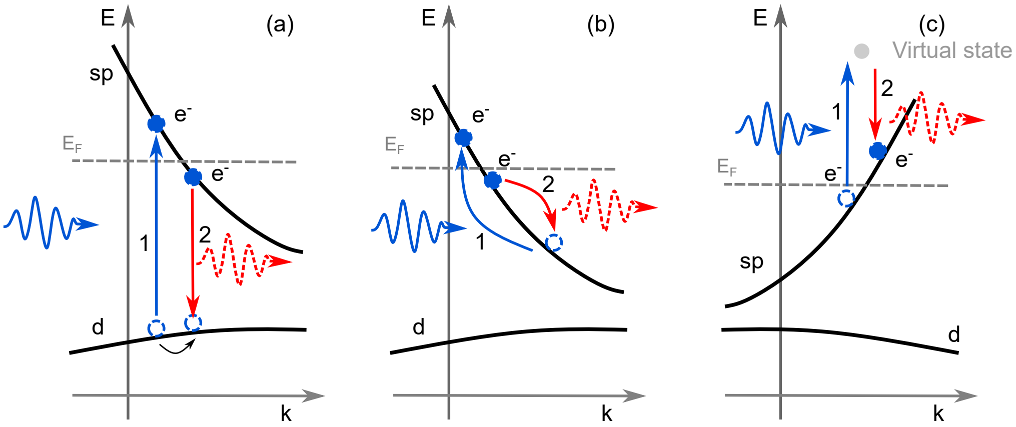

Figure 5.3.: *The different emission mechanism for linear photoluminescence in gold, in (a) interband transitions, (b) intraband transitions and in (c) electronic raman or inelastic light scattering, are shown. In all three figures the the energy (E) dispersion in function of the electron momentum (k) for both the conduction band and the d-band are sketched. The Fermi energy of the metal is shown in gray dashed line. The blue arrow represents the incoming photon, the red (dashed) arrow the emitted photon.*

Intraband transitions Also in [186] the photon energies (at 780 nm) of the excitation beam are below the interband gap energy and still linear photoluminescence is observed. Therein the luminescence was attributed to intraband transitions, sketched in Figure 5.3 (b).

The mechanism is quite similar to the interband transitions. In a first step an electron absorbs an incoming photon and is promoted to higher energy, the transition occurs within the same conduction band (no energy gap). Then a second electron (still from the same band) fills the hole by emitting a photon. Usually transitions within the same band are forbidden due to the momentum mismatch between the different states. This momentum mismatch cannot be provided by a free propagating photon[1], yet in this case the tight confinement and large field gradients of the plasmon modes allow to overcome this mismatch [187].

Electron Raman scattering Inelastic light scattering or electron Raman scattering (usually found as ERS in the literature) is also invoked to explain the observed photoluminescence, sketched in Figure 5.3 (c). In electronic raman scattering, electrons in the conduction band absorb incoming photons to transition to a virtual electronic state, as in common non-resonant Raman or Rayleigh scattering. The electron in the virtual state then transitions to an unoccupied higher lying electron state in the conduction band accompanied by the emission of a photon. The momentum mismatch is again provided by the localization of the photon mode. In [188], the comparison between theoretical calculations and dark field scattering spectra was used to support this claim.

5.1.3. Origin of the nonlinear photoluminescence in metals

Let us now discuss the origin of the upconverted photons. As different hypotheses are advanced for the linear photoluminescence (considering only one photon absorption processes), it is not surprising that also several mechanisms are proposed to explain the origin of the up converted photons.

Two photon absorption interband light emission The first observations of up converted photons from metals were explained by a two photon absorption and subsequent interband emission process [189]. This accounts for the creation of an electron hole in the d-band although incoming photons may have energies less than the interband gap. The observed quadratic power dependence in [186, 189, 190] of the nonlinear photoluminescence indeed seems to confirm that a two photon absorption process with consequent light emission is at play.

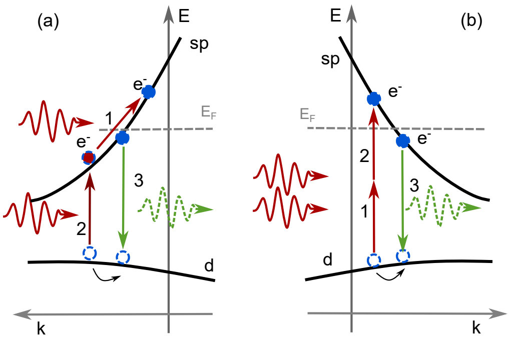

Figure 5.4.: *Sketch of the incoherent (a) and coherent (b) two photon absorption and subsequent interband luminescence.*

---

[1] Compared to the electron momentum, the photon momentum is negligibly small, allowing only vertical transitions in the E-k diagram of Figure 5.3

Two possible absorption pathways (coherent and incoherent) are considered [191, 192]. These are illustrated in Figure 5.4 a) and b). In the incoherent two photon absorption process (a) an electron in the conduction band lying below Fermi energy is excited by an incoming photon to a state above Fermi energy (an intraband transition), leaving a hole in the conduction band (1). This hole is then filled by a transition of a electron from the d-band absorbing a second incoming photon (2). The lifetime of the hole in the conduction band is estimated to be about 1 ps [190]. In the coherent absorption process (Fig. 5.4 b)), an electron in the d-band absorbs two photons (1,2) at the same time and transitions immediately to a state in the conduction band above the Fermi energy. In both cases a hole is left in the d-band, which can be filled with an electron from the conduction band (3) leading to emission of photon (green dashed).
The polarization dependence of the excitation beam for the nonlinear photoluminescence in gold nanorods [191, 192] and on the pulse duration of the excitation beam [190] favor the incoherent two photon absorption process. According to the theoretical calculations in [192] for laser pulses shorter than 50 fs, the coherent absorption should become dominant instead.

Non-quadratic and non-integer power law behavior The dependence of the up converted photoluminescence in function of optical excitation power is however not always quadratic. In [193] using short laser pulses (below 100 fs) and high laser intensities a power to the fourth dependence has been reported. This was subsequently explained as a four photon absorption process. Also non-integer power exponent have been observed, such as 1.9 in [194], and 3.6 and 4.7 in [195]. In [181] the observed power exponent could be tuned from below 2 until beyond 7, challenging thus the simple two (or multi) photon absorption model.

The photoluminescence intensity in function of the excitation becomes even more surprising if one considers the behavior of individual wavelengths and not of the whole photoluminescence spectrum, as shown in Figure 5.5. This measurement was obtained by successively increasing the power excitation and acquiring a spectrum on the same thin gold film as for Figure 5.2.
Although at each wavelength the radiated intensity I_λ versus the excitation power I_{exc} obeys a power law $I_\lambda \propto I_{\mathrm{exc}}^{p(\lambda)}$, the exponent $p(\lambda)$ is wavelength dependent. As shown in Figure 5.5 b) in the up-converted part of the spectrum, p lays between 2 and 4 and increases with decreasing wavelength. On the contrary for wavelengths of the down-converted region, for wavelengths between 900 nm and longer, p is almost constant and close to 1, indicating indeed a linear photoluminescence mechanism as presented above.

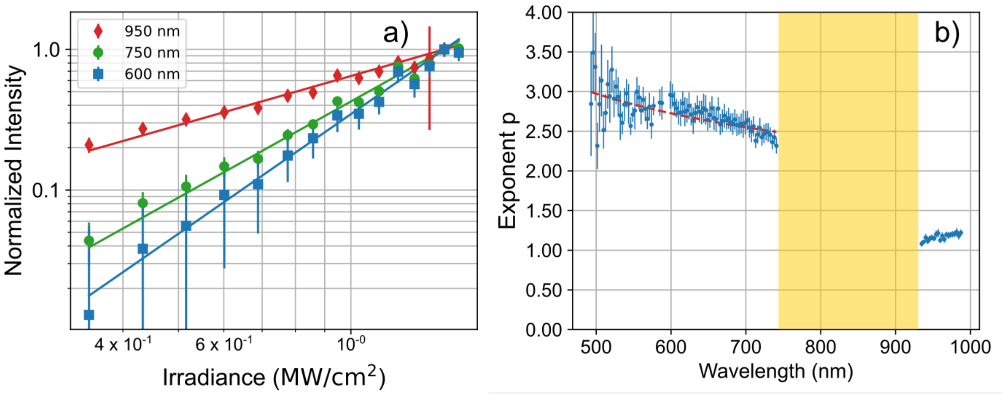

Figure 5.5.: *In (a) the normalized detected photon intensity in function of the beam excitation is shown for three wavelengths, dots. Each data set is normalized by the second highest power. The straight line indicates the power law fit. In (b) the law exponents p for each wavelength are shown.*

Light emission from a hot electron bath The wavelength dependence of the power law exponent $p(\lambda)$ can be hardly explained by a multiphoton absorption process. Instead thermal radiation from an out of equilibrium hot electron bath is invoked [196–198] to account for the observed $p(\lambda)$.

When exciting the metal structures (gold, silver or similar) with the intense pulsed excitation (pulses shorter than 1 ps), part of the energy is absorbed by electrons in the metal. This creates electrons with an excess energy. These electrons then relax their energy due to scattering with other electrons and phonons. Since electron-electron scattering is faster than the electron-phonon coupling, for a short period of time a hot electron bath is created at an electron temperature T_e higher than the lattice temperature under pulsed excitation. The hot electron temperature eventually relaxes to the lattice temperature by electron phonon coupling [170, 171, 199–202].

The creation of the hot electron bath thus resembles quite the one already presented in section 4.2.1 with an electric excitation the overbias emission. This similarity also motivated the experimental study presented in this chapter. As in section 4.2.1, the hot electron bath radiates according to Kirchhoff's law of thermal radiation 4.2, which I write here in a slightly different, wavelength dependent form:

$$I(\lambda, T_\mathrm{e})\, d\lambda = \phi(\lambda)\frac{2\pi c}{\lambda^4}\frac{1}{e^{\frac{hc}{\lambda k_B T_\mathrm{e}}} - 1}\, d\lambda \tag{5.1}$$

with $I(\lambda, T_\mathrm{e})$ the spectral photon flux, c the speed of light, h the Planck's constant, k_B the Boltzmann constant. $\phi(\lambda)$ takes into account the emissivity of the material and possibly the detection efficiency at wavelength λ. Since, the electron bath is decoupled from the phonon bath, the electron temperature may reach values higher than the melting temperature of gold (1340 K [203]).
As in the approximation of equation 4.1, the electronic temperature is assumed here to obey a power law with respect to the excitation power I_exc [197, Appendix]:

$$T_\mathrm{e} = T_{\mathrm{e},0}\left(\frac{I_\mathrm{exc}}{I_0}\right)^{\frac{1}{a}} \tag{5.2}$$

where I_0 is some normalization coefficent, a the power exponent. For equation 4.1 a is thus equal to 2.
From the considerations above one can calculate the power law $p(\lambda)$ behavior as [196, 197]:

$$p(\lambda) = \frac{d\ln(I(\lambda, T_\mathrm{e}))}{d\ln(\frac{I_\mathrm{exc}}{I_0})} \simeq \frac{hc}{a\lambda k_B T_\mathrm{e}} \tag{5.3}$$

which reflects the power law trend for short wavelengths in Figure 5.5 (b). In [197], more elaborate calculations considering also inelastic light scattering for a hot electron bath or hot electron interband transitions, are presented. A further extension of the theory is also presented in [204].

By assuming a constant ϕ over the wavelength range of 600 nm to 730 nm, I fitted equation 5.2 directly onto the measured spectra. I assumed a constant ϕ for all spectra and used the electron temperature as fit parameter, this is shown in Figure 5.6 (a) for 5 different excitation powers. The fitted electron temperature in function of excitation power is shown in Figure 5.6 (b). As can be seen the temperatures are well fitted by a power law (black line) from which a value of $a = 3.4$ is extracted. This value is higher than $a = 2$, predicted for an electron gas at low temperatures [44, 197], but is consistent with the scientific literature, reporting even higher values of $a = 3.85$ and $a = 4$ in [196,198]. These higher values of the a exponent indicate that it is harder to heat the electron temperature to higher temperatures than what assumed so far. The discrepancy might be an indication that the low-temperature linear heat capacity of the electron gas is not anymore justified [205]. Additionally one could also consider a depleted absorption of electrons at higher excitation fluxes or the negligence

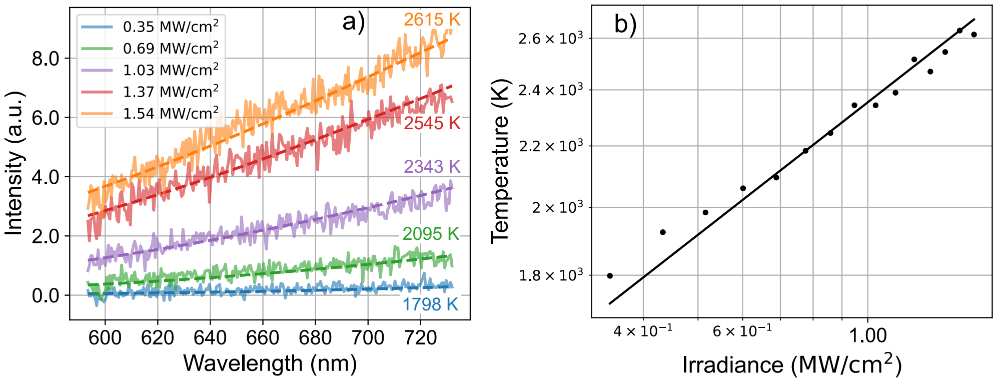

Figure 5.6.: *In (a) five spectra taken at different excitation powers are shown (solid lines). Each is spectrum is fitted with equation 5.1, dashed lines. In (b), fitted temperature in function of excitation power is plotted. The power law of equation 5.2 is shown as the line with* $a = 3.4$.

of the scattering mechanism contributing to an appreciable energy loss already in the first few fs. However, to the best of my knowledge, so far no hypothesis in the literature has been investigated or proposed.

Electron raman scattering of hot electrons Inelastic light scattering (or elastic raman scattering) together with a hot electron distribution can also account for the observed upvconverted part of the luminescence spectra [206]. This is sketched in Figure 5.7.

Due to the higher temperature, some electrons are found in energetically higher states in the conduction band. When such an electron absorbs a photon (1) and transitions to a virtual state, it may then decay to a lower lying electron state while emitting a photon (2). As the final electron energy is lower than its initial energy, the emitted photon (green dashed) has a higher energy than the excitation.

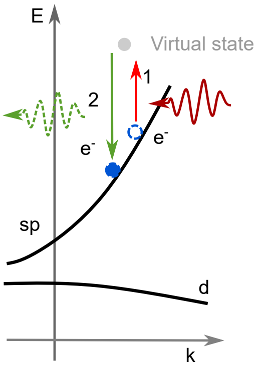

Figure 5.7.: *Inelastic light scattering resulting in the emission of an up converted photon.*

The main difference between inelastic light scattering and thermal emission is the time scale involved in the two processes, whereas the hot electron emission occurs as long as the electron bath is hot (in the order of 1 ps, [180, 181]), the inelastic light scattering has a intrinsic interaction time less 10 fs, and should occur only during pulsed excitation [188, 206]. Indeed for the linear photoluminescence both an ultrafast component (limited by the intrument response function of the experiment to 50 fs) and a slowly decaying contribution have been observed by upconversion measurement techniques [207]. One may could repeat this experiment also for the nonlinear photoluminescence to distinguish between the two contributions.

Relation to overbias light emission in tunnel junctions As it is clear from the discussion above, overbias light emission in electromigrated tunnel junctions and the nonlinear photoluminescence share many similarities. Both share a similar spectral emission range and nonlinear dependence in the emission and are explained by a similar hot electron emission hypothesis. This has been further exploited in [167], where the overbias emission was additionally excited with 785 nm CW laser. The increased photon yield by a factor of 1000 over the single electrical or laser excitation was explained within the hot electron model, as the nonlinearity of emission yield with the variation to the electron temperature.

5.2. Photon correlation measurements of the nonlinear photoluminescence in metals

This section will finally present the photon correlation measurements and elucidate their initial motivation. The discussion of the photon correlation in the following may appear to be quite detailed and long before presenting the results and interpretation of the measurements. Nonetheless I think it is interesting to present the relevant theoretical and experimental aspects (in particular the integration times) needed to perform such measurements.

5.2.1. The photon correlation

The normalized (second order) photon correlation of a (stationary) light source is defined as [208]:

$$g_2(\tau) = \frac{\langle \mathrm{I}(t)\mathrm{I}(t+\tau)\rangle}{\langle \mathrm{I}(t)\rangle\langle \mathrm{I}(t+\tau)\rangle} \tag{5.4}$$

where $\mathrm{I}(t)$ is the intensity of the light source at the instant t and the brackets indicate statistical averaging. It has already been encountered by the reader in the Chapters 2 and 3 where the intensity fluctuations in light emission from wide gap gold junctions and the silver memristors were characterized. There, the considered time delays ranged from roughly 100 ns up to some ms and seconds. For the photon autocorrelation discussed here I will only consider its behavior at almost zero time delay. At such short time delays the photon autocorrelation is not only an expression the emitter dynamics but is also intrinsically linked to emission process [208].

The photon correlation can also be expressed in function of the (single mode) photon creation $\hat{\mathbf{E}}_k^\dagger(t)$ and annihilation $\hat{\mathbf{E}}_k(t)$ operators:

$$g_2(\tau) = \frac{\langle\Phi|\sum_{k,j}^{N} \hat{\mathbf{E}}_k^\dagger(t)\hat{\mathbf{E}}_j^\dagger(t+\tau)\hat{\mathbf{E}}_j(t+\tau)\hat{\mathbf{E}}_k(t)|\Phi\rangle}{\langle\Phi|\sum_{k}^{N} \hat{\mathbf{E}}_k^\dagger(t)\hat{\mathbf{E}}_k(t)|\Phi\rangle \cdot \langle\Phi|\sum_{k}^{N} \hat{\mathbf{E}}_k^\dagger(t+\tau)\hat{\mathbf{E}}_k(t+\tau)|\Phi\rangle} \tag{5.5}$$

where Φ is the light state emitted by the source, the sum runs over all detected photon states N, in the case of continuous photon states the sums should be replaced by integrals. The photon correlation indicates the ratio of observed photon pairs spaced in time τ normalized by expected photon pairs with same time delay for independent photon arrival which is given by $\langle \mathrm{I}(t)\rangle\langle \mathrm{I}(t+\tau)\rangle$.

As mentioned in chapter 2 the limit of long time delays the photon correlation is equal to 1. There is no correlation between photons emitted at long time delays. One usually distinguish between three behaviors. In the following we will thus be only interested at the photon correlation at zero time delay.

The case of $g_2(0) < 1$ is referred to as antibunching. This signifies that it is less probable to observe two photons arriving at the same time than to observe a random coincidence of two uncorrelated photons at an arbitrary time delay. Antibunching is usually observed in the case of few photon emitters. For example a single photon emitter does not emit more than one photon at a time. It is therefore impossible to observe two photons at the same time and $g_2(0) = 0$.

$g_2(0) = 1$ is observed for coherent sources, such as most of the laser sources or light emitted by classical currents [209]. It implies that photon arrivals are completely independent one of each other. A transition in the photon correlation towards $g_2(0) = 1$ is observed in lasers at the passage from amplified spontaneous emission towards lasing [210].

The case of $g_2(0) > 1$ is called photon bunching. In this case the probability of observing two photons at the same time is higher then observing two times a photon independently, the photons ”are bunched” together. This is observed for light sources of many independent emitters, called chaotic light sources, and is a consequence of the photons being bosonic particles [211–214]. This applies for example to thermal emission, but also amplified spontaneous emission [208, 215] or to arc discharge lamps. For chaotic light sources there exists an upper limit of $g_2(0) = 2$ [208].

Photon bunching with values of $g_2(0) > 2$, can indicate an unusual correlation within the light such as photon pair emission. However for pseudo thermal light, schemes to increase the photon bunching beyond $g_2(0) > 2$ have also been demonstrated [216].

5.2.2. Photon statistics of overbias emission

At this point I will briefly discuss the predicted photon correlation for both overbias emission hypotheses (hot electron radiation and coherent multi-electron inelastic tunneling).

Photon statistics of thermal radiation Thermal radiation behaves as a chaotic source. The photon correlation observes thus $1 \leq g_2(0) \leq 2$. Whether this value is closer to 1 or 2 will be discussed further below.

Photon statistics of inelastic tunneling The light emission statistics emitted by fluctuating currents has been derived in [217]. Whereas generally it predicts photon bunching emission statistics, with ($g_2(0) \geq 1$), for light emission from metallic conductors with conductance values equal to G_0, photon antibunching ($g_2(0) \leq 1$) at specific photon energies [218] is predicted. Performing the photon correlation measurement at finite temperatures adds additional limits on the time resolution required to observe the predicted photon antibunching [219].

To add further challenges on the measurement, the photon counts (overbias and normal) at conductances equal to G_0 are expected to drop almost to zero [182]. This is explained [169, 182] by current fluctuation suppression due to the fermionic nature of electrons, which are at the origin of the antibunching statistics [218].

The experimentally measured photon statistic of inelastic electron tunneling shows even more surprising behavior. Instead of simple bunching, superbunching ($g_2(0) \geq 2$) and photon pair generation has been observed [220–222].

In [220], a two photon emission model has been proposed to explain the superbunching in inelastic tunneling. This model however still underestimates the amount of created photon pairs. A part from this, to the best of my knowledge no theoretical explanation for this superbunching in inelastic tunneling has

been provided. An approach may be found in [223,224], where resonant electron phonon interactions lead to avalanche electron transmission behavior.
Measuring for the overbias emission, a photon correlation outside standard photon bunching, i.e. $g_2(0) < 1$ or $g_2(0) > 2$, would clearly indicate a two electron emission process and discard the hot electron emission hypothesis. On the other hand observing $1 \leq g_2(0) \leq 2$ does not rule out a multi coherent inelastic electron tunneling as source of the observed overbias photon emission.

5.2.3. Chaotic sources

Since the nonlinear photoluminescence in metals results from many (emitters) electrons it is expected to behave as a chaotic source. In the following I will thus focus in more detail on the photon correlation behavior of chaotic sources. For chaotic sources one can show that the photon correlation obeys [208,212–214]:

$$g_2(\tau,\vec{x}) = 1 + |g_1(\tau,\vec{x})|^2 \cdot \frac{(1+P^2)}{2} \tag{5.6}$$

where I haven taken into account also the spatial separation dependence in the photon correlation, P is the total polarization of the detected light[2] and $g_1(\tau,\vec{x})$ is the first order coherence of the light, which as both a spatial ($\vec{x}$) and a temporal (τ) component.

5.2.4. The first order coherence of light

Because the bunching peak height of a chaotic sources depends essentially on its first order coherence, it is worth to spend a few sentences on it. The first order coherence of light determines the visibility of fringes in interference experiments and is defined as [208,214,225]:

$$g_1(\tau,\vec{x_0},\Delta\vec{x}) = \frac{\langle \mathbf{E}^*(t,\vec{x_0})\mathbf{E}(t+\tau,\vec{x_0}+\Delta\vec{x})\rangle}{\sqrt{\langle \mathbf{E}^*(t,\vec{x_0})\mathbf{E}(t,\vec{x_0})\rangle\langle \mathbf{E}^*(t+\tau,\vec{x_0}+\Delta\vec{x})\mathbf{E}(t+\tau,\vec{x_0}+\Delta\vec{x})\rangle}} \tag{5.7}$$

where $\mathbf{E}$ is either the complex field amplitude of the electric field or the electric field photon annihilation operator in a quantum optics view point.
From this definition of the first order coherence one can deduce that for zero time delay ($\tau = 0$) and perfect spatial overlay ($\Delta\vec{x} = \vec{0}$), $g_1(0,\vec{x_0},\vec{0}) = 1$ i.e. light always interferes with itself. This is a direct consequence of the superposition principle of electromagnetic waves. For long time delays or large spatial

---

[2] $P = 1$ for totally polarized light, $P = 0$ for totally unpolarized light.

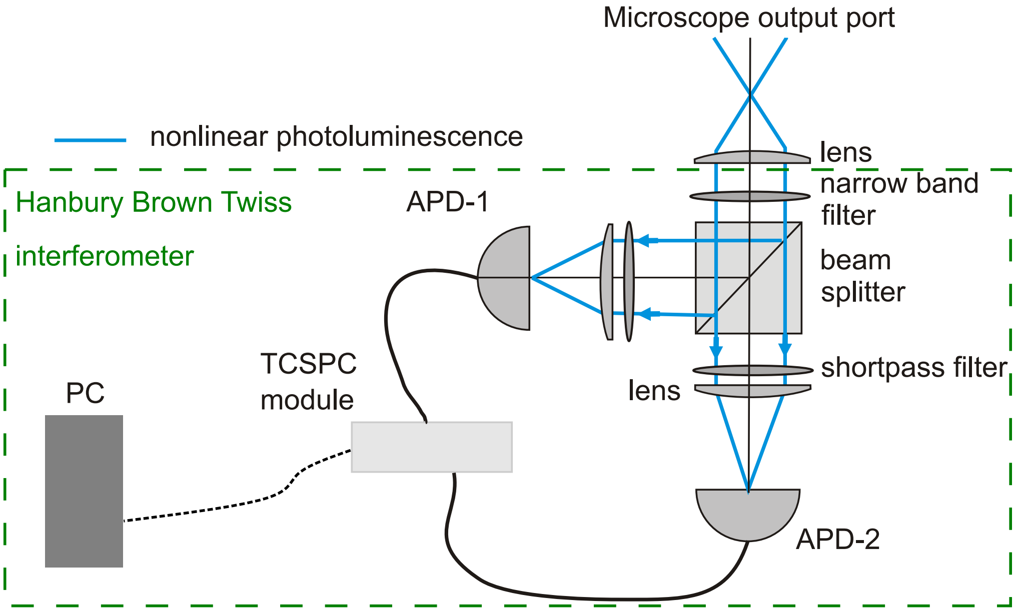

Figure 5.8.: *Sketch of the setup used to measure the photon correlation of the nonlinear photoluminescence of different metal structures. The excitation part of the nonlinear photoluminescence is shown in Figure 5.1. The collected photoluminescence is then sent onto a Hanbury Brown Twiss interferometer consisting of a 50/50 beam splitter and two avalanche photodiodes connected to a TCSPC module. All lenses after the tube lens have the same focal length. The narrow band filter is used to increase the coherence time of detected light. Two shortpass filters (cutoff wavelength 714 nm) are inserted to reduce background correlations due to the afterglow from both APDs [227].*

separations any coherence between light is lost and therefore $g_1 \to 0$. There typically exists a characteristic time τ_c (the coherence time) and length scale x_c (coherence length) over which (the modulus) the first order coherence decays.

Both the coherence time τ_c and the coherence length x_c can be altered by spectral (Wiener-Kinchin theorem) or spatial filtering (van-Cittert-Zernike theorem) [208, 226]. In particular the possibility to increase the coherence time by using narrow spectral filtering is exploited in my measurements, see section 5.2.5.

5.2.5. Photon correlation measurement setup

The first photon correlation experiments were performed in 1956 by Hanbury Brown and Twiss in 1956 [228]. Their setup to measure the photon correlation consisted of a 50/50 beam splitter and two photon detectors connected to a coincidence counter. This is today called a Hanbury Brown Twiss (HBT) interferometer and probably the most used setup to measure photon correlations. Modifications of this setup have tried to increase the time resolution of the detection [229] by using gated sum frequency generation or to increase the coherence time of the light source by narrow spectral filtering before the interferometer [226]. Spectral filtering increases the coherence time τ_c and therefore the bunching peak height, but the integration time T_o is at best unchanged.
A different approach was shown in [215], where a Michelson-Morley interferometer together with two photon absorption in a diode was used to measure the photon correlation. This allows time resolution of a few fs, much higher than what is achievable with any photodetector. However, the two photon absorption process is rather inefficient compared to single photon detectors such as avalanche photodiodes (APDs) and requires thus rather bright sources.

Setup After exciting and collecting the luminescence as explained above in Section 5.1.1 the light is then sent to a Hanbury Brown Twiss interferometer to measure the photon correlation, as shown in Figure 5.8.
First the nonlinear photoluminescence is spectrally filtered using a narrowband line filter (Melles Griot) centered at 632.8 nm with a spectral width of 4 nm. The light is then divided by a beam splitter and focused onto two APDs (Micro Photon Devices, PD 050 CTC), with 50 μm detection area, 30 ps time resolution and 77 ns dead time. For my measurements I reached typical count rates between $10^4 - 10^5$ Hz at each APD.

Both APDs are then connected to a time correlated single photon counting (TCSPC) module (Hydraharp 400, Picoquant), which for each detected photon event records its detection time to a file. These are then further processed in order to extract the photon correlation.
To avoid an afterglow contribution of the APDs to the photon correlation

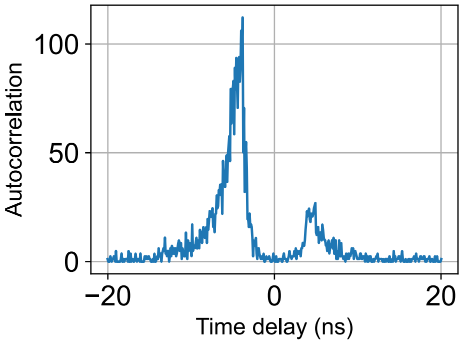

Figure 5.9.: *Normalized photon autocorrelation of background stray light featuring two characteristic afterglow peaks. Their presence is due to cross-talking of both APDs [227]. The peak height asymmetry is due to a higher count rates at one detector.*

histogram [227], as shown in Figure 5.9, a shortpass filter (Semrock, 714 nm) and a pinhole were inserted before each APD. Additionally I slighted tilted all elements and carefully shielded both APDs to reduce cross talking as much as possible.

5.2.6. Integration times and predicted bunching peak heights

If one considers zero time delay and perfect spatial overlap between the two detectors, one has that $g_1(0,0) = 1$. From equation 5.6 it seems thus that one measures $g_2(0) = 2$ (1.5 for unpolarized light) as long as one manages to precisely overlap spatially and temporally both detectors. But this does not take into account the finite time resolution τ_d (30 ps) and the nonzero detection area of $A_d = \pi \frac{50\,\mu\mathrm{m}^2}{4}$ in the measurements. Especially the time resolution of detectors is typically greater than the coherence time of the source (0.122 ps for the filtered light in my measurements).

For spectral narrow (intrinsic or filtered) chaotic sources [230, 231] the spatial and temporal characteristics of the source are independent, one can therefore write the measured photon bunching height, as product of spatial, temporal and polarization dependencies:

$$g_2(0) - 1 = C_{\text{polarization}} \cdot C_{\text{spatial}} \cdot C_{\text{temporal}} \tag{5.8}$$

For all factors it is that $0 \leq C_{\text{x}} \leq 1$, where C_{x} is either the polarization, spatial or temporal factor.

Polarization dependence From equation 5.6 it is clear that

$$C_{\text{polarization}} = \frac{1 + P^2}{2} \tag{5.9}$$

This has been verified experimentally in [231].

Spatial coherence factor

The spatial coherence factor is more complex to evaluate. One could calculate it with something similar to the following integral:

$$C_{\text{spatial}} = \frac{1}{A_{d1} A_{d2}} \int\limits_{A_{d1}} \int\limits_{A_{d2}} d\vec{x_1}\, d\vec{x_2} \cdot i_1(\vec{x_1}) i_2(\vec{x_2}) \cdot |g_1(0, \vec{x_1}, \vec{x_2} - \vec{x_1})|^2 \tag{5.10}$$

where i_1, i_2 are the (normalized)[3] intensities at detector 1 resp. 2.
I have however not done such calculation for the system as the spatial distribution generated by the excitation is generally quite complex due to emission enhancement at edges or discontinuities.
Nonetheless, one can make some rough estimates, by approximating equation 5.10 as

$$C_{\text{spatial}} \simeq \frac{\mathrm{A}_{\text{coh}}}{\mathrm{A}_{\text{det}}}$$

where A_{coh} is the size of the coherence area and A_{det} the detected source emission area with $\mathrm{A}_{\text{coh}} \leq \mathrm{A}_{\text{det}}$. This approximation can be derived considering a constant emission intensity over the detection areas $i_{1,2}$ and step like correlation function g_1 being equal to 1 inside the correlation distance and zero outside.
To estimate C_{spatial} I will thus look at the ratios between coherence length, emission size and detection area.
If one considers an idealized point spread function of the microsope [232] the excitation spot size is $0.6098\frac{\lambda}{NA} \simeq 330$ nm. The light emission spot should be even smaller since the nonlinear photoluminescence is a nonlinear process, featuring even smaller localized hot spots. For example, the luminescence of a gold nanoparticle of 60 nm diameter originates clearly from smaller area than the diffraction limited spot size. The coherence length for 632.8 nm is then $x_c = \frac{\lambda}{2 \cdot n} = \frac{623.8 \text{ nm}}{2 \cdot 1.53} \simeq 207$ nm, where $n = 1.53$ is the refractive index of the glass substrate and the oil. This is then magnified by a factor 100 and projected onto the APDs with 50 μm diameter of the detection area. Therefore the coherence area is a fraction of $(207 \text{ nm}/330 \text{ nm})^2 = 0.4$ of the excitation spot, and a fraction of $((207 \text{ nm} \cdot \mathrm{M})/25\ \mu\text{m})^2 = 0.64$ of the detector size, where $\mathrm{M} = 100$ is the microscope magnification.[4]
Assuming perfect detector alignment one would thus expect to have a spatial coherence factor of about $C_{\text{spatial}} = 0.64$ for a gold film and $C_{\text{spatial}} = 1$ for a subwavelength gold nano-particle.

---

[3] The normalization is such that

$$\frac{1}{A_{d1}} \int\limits_{A_{d1}} d\vec{x}\ i_1(\vec{x}) = 1$$

.

[4] The spatial correlation propagates in space by obeying the same wave equations as the light intensity [208]. Thus, like the diffraction limited spot also the coherence length is magnified.

Temporal dependence

Instead of the temporal coherence factor C_{temporal}, I derive here the total expected pair photon counts $C_{\text{tot}}(\tau_o)$. This has the advantage to also provide the expected integration times for the photon correlation measurements.

The expected photon pair counts C_{tot} for detectors with a finite time resolution can be calculated with the following formula [208, 233]:

$$\begin{aligned} C_{\text{tot}}(\tau_o) = \int_{\tau_o-\frac{\Delta\tau}{2}}^{\tau_o+\frac{\Delta\tau}{2}} d\tau \int_0^{T_o} dt \int_{-\infty}^{\infty} dt_1 \int_{-\infty}^{\infty} dt_2 \; I_1(t_1) I_2(t_2) \cdot \\ D_1(t_1 - t) \cdot D_2(t_2 + \tau - t) \cdot (1 + C|g_1(t_1 - t_2)|^2) \\ = C_r + C_b(\tau_o) \end{aligned} \tag{5.11}$$

where T_o is the total integration time, τ_o the mean time delay between the two detectors and $\Delta\tau$ is the bin width of the delay in the histogram. $I_1(t)$ and $I_2(t)$ are the count rates at detector 1 resp. 2 and $D_{1,2}(t)$ are their respective instrument response functions. $C = C_{\text{polarization}} \cdot C_{\text{spatial}}$ is a coherence factor taking into account the spatial and polarization resolution of the measurement as previously presented.

In the last equality I have split the total photon pair counts into a time delay independent contribution C_r, giving the random photon coincidences, and the additional photon pairs $C_b(\tau_o)$ due to the bunching of the source.

The detailed calculations are found in Appendix A. Table 5.1 shows the results expected for a continuous source and an exponentially decaying pulses with lifetime t_p and repetition rate f_{rep}.

From Table 5.1 one can deduce that, assuming the same mean count rates, there is a huge gain for pulsed sources both in bunching peak height by a factor $\frac{\tau_d\sqrt{\pi}}{\tau_p} \simeq 50$ and more important in integration time by a factor $\frac{\tau_d\sqrt{\pi}}{\tau_p^2 \cdot f_{\text{rep}}} \simeq 6 \cdot 10^5$, where I have inserted the values of the experimental setup: the detector time resolution is $\tau_d = 30$ ps, the repetition rate of the laser is $f_{\text{rep}} = 80$ MHz and the lifetime of the NPL is assumed to be $t_p = 1$ ps [180, 181]. This means that for an hour of a pulsed experiment one would need to integrate for about 65 years for a continuous source in order to obtain the same signal to noise ratio!

Additionally, I give in Appendix B some (approximate) formulas for the integration times and expected peak heights in function of the mean photon number per photon mode (or coherence volume $\text{V}_{\text{coh}} = \tau_{coh} \cdot \text{A}_{\text{coh}}$). From this one can also estimate the hypothetical hot electron temperature.

		Continuous source	Pulsed
Random coincidences	C_r	$I_1 \cdot I_2 \cdot \tau_d \cdot T_o$	$\bar{I}_1 \cdot \bar{I}_2 \cdot \frac{T_o}{f_\text{rep}}$
Bunching peak height	$g_2(0)-1 = \frac{C_b}{C_r}$	$C \cdot \frac{\tau_c}{2\tau_d} \cdot 0.96$	$C \cdot \sqrt{\pi} \cdot \frac{\tau_c}{2t_p}$
Signal to noise ratio	$\text{SNR} = \frac{C_b}{\sqrt{C_r}}$	$C \cdot \frac{\tau_c}{2\tau_d} \cdot 0.96 \cdot \sqrt{I_1 I_2 \tau_d T_o}$	$C \cdot \sqrt{\pi} \cdot \frac{\tau_c}{2\tau_p} \sqrt{\bar{I}_1 \cdot \bar{I}_2 \cdot \frac{T_o}{f_\text{rep}}}$
Integration time	T_o	$\frac{\text{SNR}^2}{0.92 \cdot C^2} \cdot \frac{4 \cdot \tau_d}{I_1 \cdot I_2 \cdot \tau_c^2}$	$\frac{\text{SNR}^2}{\pi \cdot C^2} \cdot \frac{4 \cdot \tau_p^2 \cdot f_\text{rep}}{\bar{I}_1 \cdot \bar{I}_2 \cdot \tau_c^2}$

Table 5.1.: *Theoretical expectations of photon pair count rates, bunching peak height and integration time for pulsed and continuous chaotic sources.* I_1 *resp.* $\bar{I}_1$ *are the count rates detected by the detector and except for the first line* $t_d, t_p << t_c$ *is assumed.*

5.2.7. Experimental results

Photon bunching in a thin gold film

After this long build-up, I will finally present the result of the measurements. Here for the nonlinear luminescence of a thin gold film (2 nm titanium and 25 nm of gold). The luminescence is excited at 808 nm, with an average intensity of $4\,\text{MW}\,\text{cm}^{-2}$ at a local hotspot (typically an edge or roughness of the film). The luminescence is then filtered at 628 nm and sent to both APDs, with typical count rates of $10^4 - 10^5$ at each detector.

Data treatment

In the measurement each detected photon emitted from the photoluminescence is recorded as a timestamp. From these timestamps I then construct a histogram of all time delays between successive photon pairs. This is done with a home-made python script. For each photon event registered by the first detector (APD 1), the program considers the closest photon event registered by the second detector (APD 2), and then calculates the time delay between both events. The histogram then counts how many times each (positive or negative) time delay has been observed within 1 ps time resolution. Such a histogram is shown in

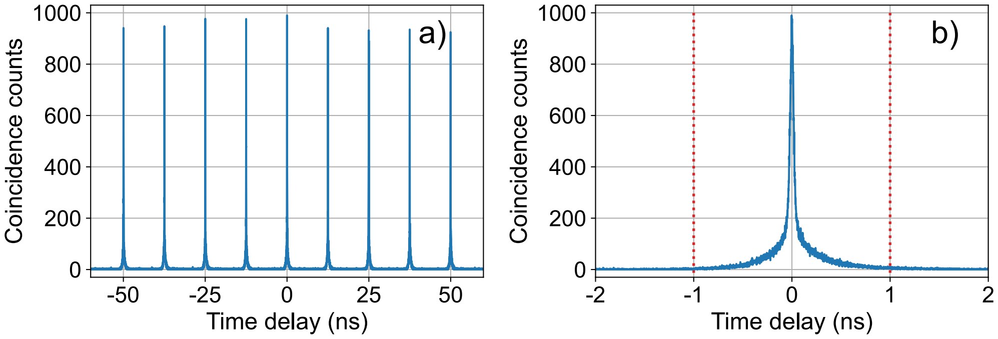

Figure 5.10.: *The figure shows a raw photon correlation histogram for a measurement on a thin gold film integrated for 1 h, the count rate was between* $10^4 - 10^5$ *Hz. In a) for time delays between -55 to 55 ns in b) a zoom into the central peak. The dashed red lines mark the integration limits.*

Figure 5.10 for the nonlinear photoluminescence of a thin gold film.

For time delays shorter than dead time of the APDs (77 ns), this is equivalent to calculating the full photon correlation, since it is not possible to have a second photon detected within the dead time of the APD.[5]

In the histogram of Figure 5.10 one observes series of discrete peaks spaced by the repetition period T_{rep} of the laser. This is due to the periodically pulsed excitation and therefore periodically pulsed emission of the nonlinear photoluminescence. Every photon is emitted only during a small pulse duration. Therefore the time delay between two photons of the photon pairs can be only a multiple $n = 0, 1, 2, -1, -2, ...$ of the pulse period $n \cdot T_{\text{per}}$.

The shape of these peaks is a convolution of the excitation pulse, the luminescence dynamics of the light source and the instrument response functions with time resolution τ_{det} of the detectors. Since in my case the excitation pulse duration is 180 fs and the decay time of the source is about τ_p ~1 ps (according to [181]), which are both considerably shorter than the time resolution of the APDs (20 ps), the observed pulse shape is only determined by the instrument response functions of the APDs.

To extract the photon correlation histogram I integrate then over each peak with limits of 1 ns, shown in red in Figure 5.10 b).

The final result after all the data treatment is shown in Figure 5.11. One

---

[5] To extent the range of time delays beyond the dead time to twice the dead time of the APDs one would need to take into account not only the closest but also the second closest photons event, and so on.

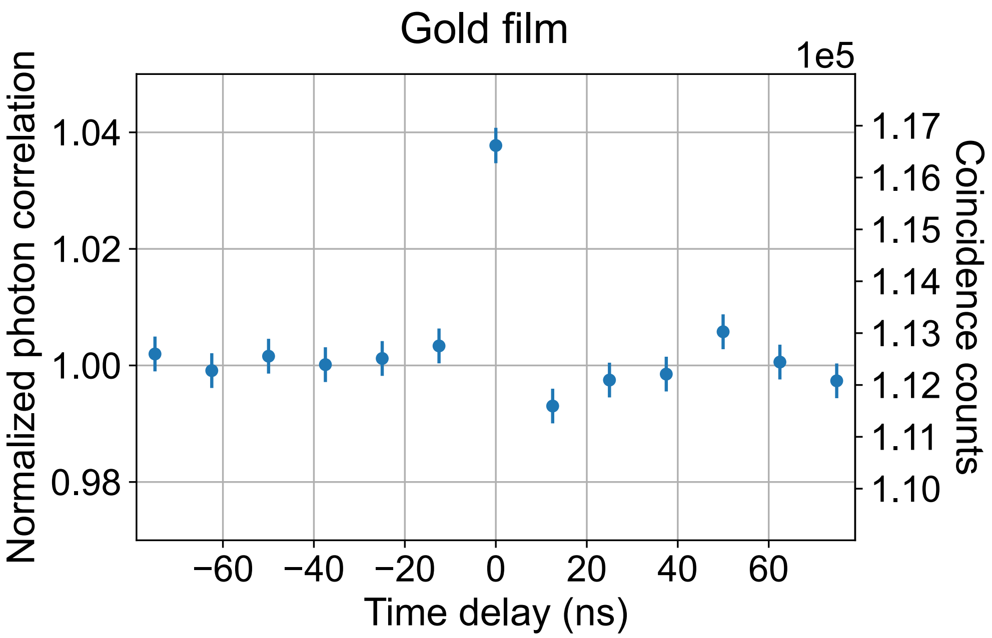

Figure 5.11.: *The photon correlation histogram for the same measurement as in Figure 5.10. The extracted photon bunching peak value is* $g_2(0) = 1.038 \pm 0.004$.

observes a clear bunching peak at zero time delay with $g_2(0) = 1.038 \pm 0.004$, achieving thus the goal of measuring the photon correlation of the nonlinear photoluminescence.

Comparison with theory

To further gain insight into the measurement one can compare the observed photon bunching with the theoretical predictions of Table 5.1 by inserting the parameters of the experiment. Due to the line filter the coherence time is $\tau_c = 0.122$ ps, by assuming a lifetime of $\tau_p = 1$ ps, which is the mean experimentally determined lifetime of a hot electron gas [180,181], one expects to observe a bunching peak of $g_2(0) = 1 + 0.10 \cdot C$. Since the detected light is unpolarized[6] this gives a spatial coherence factor about $C_{\text{spatial}} = 0.76$, which is in agreement with the

---

[6] This is an assumption, as I did not measure the polarization during the photon correlation measurements. In subsequent measurements, by taking polarized confocal nonlinear photoluminescence maps, I was however unable to observe a significant polarization of the emitted light.

estimation of in section 5.2.6. Inversely one can give also an upper limit on the life time. From $C_{\text{spatial}} \leq 1$ it follows that $\sqrt{\pi} \cdot \frac{\tau_c}{2t_p} \geq 0.076$, this gives an upper limit to the lifetime of the source of $t_p = 1.4$ ps.

If instead of emission by a hot electron gas one considers inelastic light scattering by a hot electron gas the above predictions change slightly. The lifetime of the hot electron gas is replaced by the pulse duration of the excitation of 180 fs. Assuming Gaussian pulses one then obtains a bunching peak of $g_2(0) = 1 + 0.32 \cdot C$ according to equation A.12 shown in the appendix. Within this model I therefore obtain a spatial coherence factor of $C_{\text{spatial}} = 0.24$. If I had an independent experimental approach of determining the spatial coherence factor one could thus distinguish between two emission hypotheses.

With the expressions of Table 5.1, one can also calculate the expected integration time T_o for the measurement of Figure 5.11. Inserting $f_{\text{rep}} = 80$ MHz, $\bar{I}_{1,2} = 5 \cdot 10^4$ Hz and SNR $= 0.038/0.004 = 9.5$ one obtains a predicted integration time about 40 min. This is just a bit shorter than the actual integration time of 1 h and shows thus a good overlap between theoretical predictions of Table 5.1 and the experiment.

Photon bunching in different structures

Besides the thin gold film, I measured also the photon correlation of other metallic structures, such as a silver film, monocrystalline flakes and gold nanoparticle (60 nm) showing a broad plasmonic resonance. Their luminescence response and spectra (except for the silver film) are shown in figure 5.12. Both the gold film and the gold flake show similar spectra, whereas the spectrum of the gold particle is clearly modulated by its plasmonic resonance. This resonance is also seen in the dark field scattering spectra (gray curves) of similar particles. One observes also a general emission enhancement of the nonlinear photoluminescence at the edges for both the film and the gold flake. This is typically attributed to a plasmonic enhancement and a better free space coupling of the emission at the edges.

The results of the photon correlation measurements are shown in Figure 5.13. All samples show clear bunching peaks with similar bunching peak heights. The bunching peak is of 1.045 ± 0.016 for the gold nanoparticle, of 1.037 ± 0.007 for the silver film and of 1.070 ± 0.004 for the monocrystalline gold flake.

I also display in Figure 5.13, the photon correlation measurement for the second harmonic generated with a nonlinear β-barium borate (BBO) crystal and observe a value of $g_2(0) = 1.00014 \pm 3 \cdot 10^{-5}$. This low value is expected for a coherent laser excitation [208, 234] and assures that the measured bunching peaks

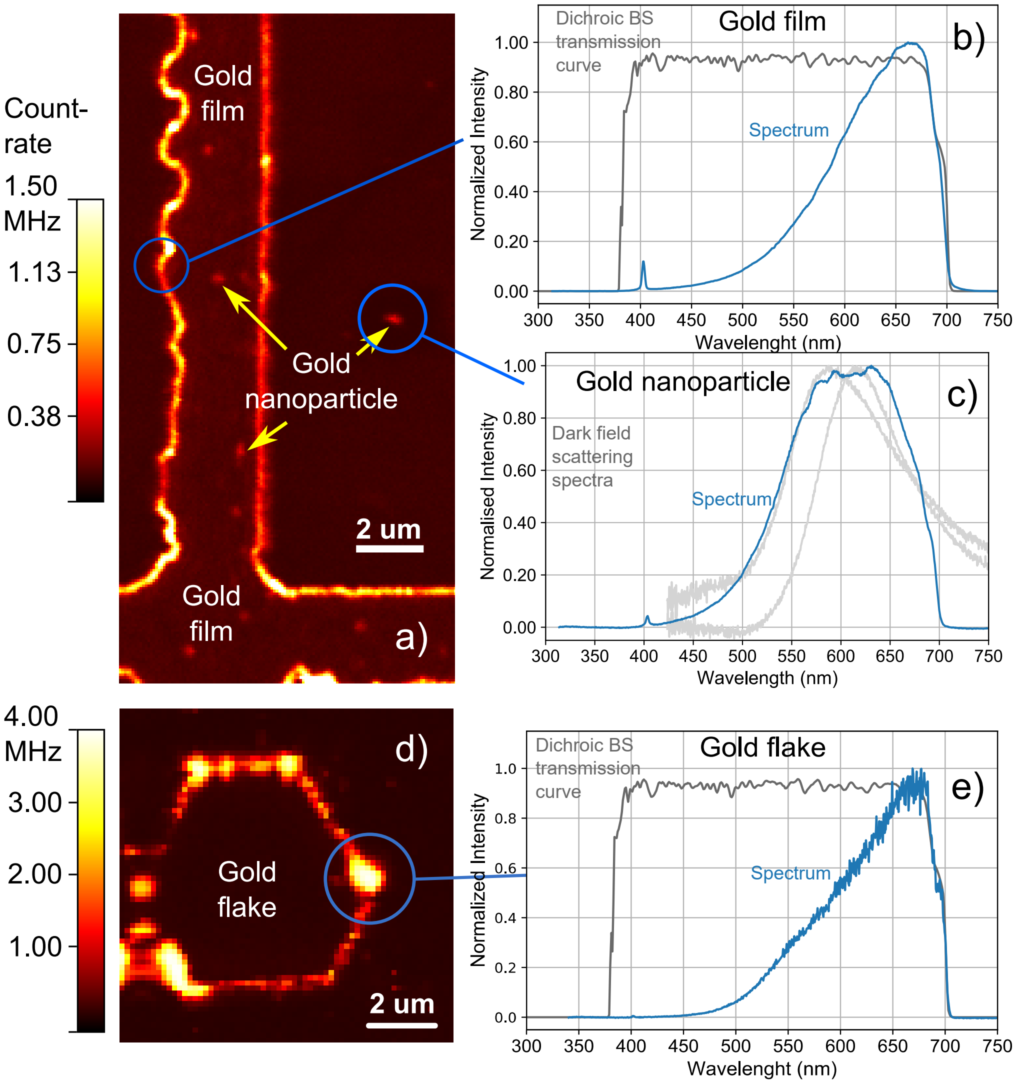

Figure 5.12.: *Confocal scans and NPL spectra of two gold samples. In (a) a confocal scan of a sample with gold nanoparticles deposited on a glass coverslip with UV-lithography prepared marks, consisting of 2 nm titanium and 25 nm of gold. In (b) and (c) the spectra of resp. the edge of the thin gold film and the gold nanoparticle indicated in (a). In (d) a confocal map of a gold flake, with its spectrum shown in (e). Reprinted with permission from [44] © The Optical Society.*

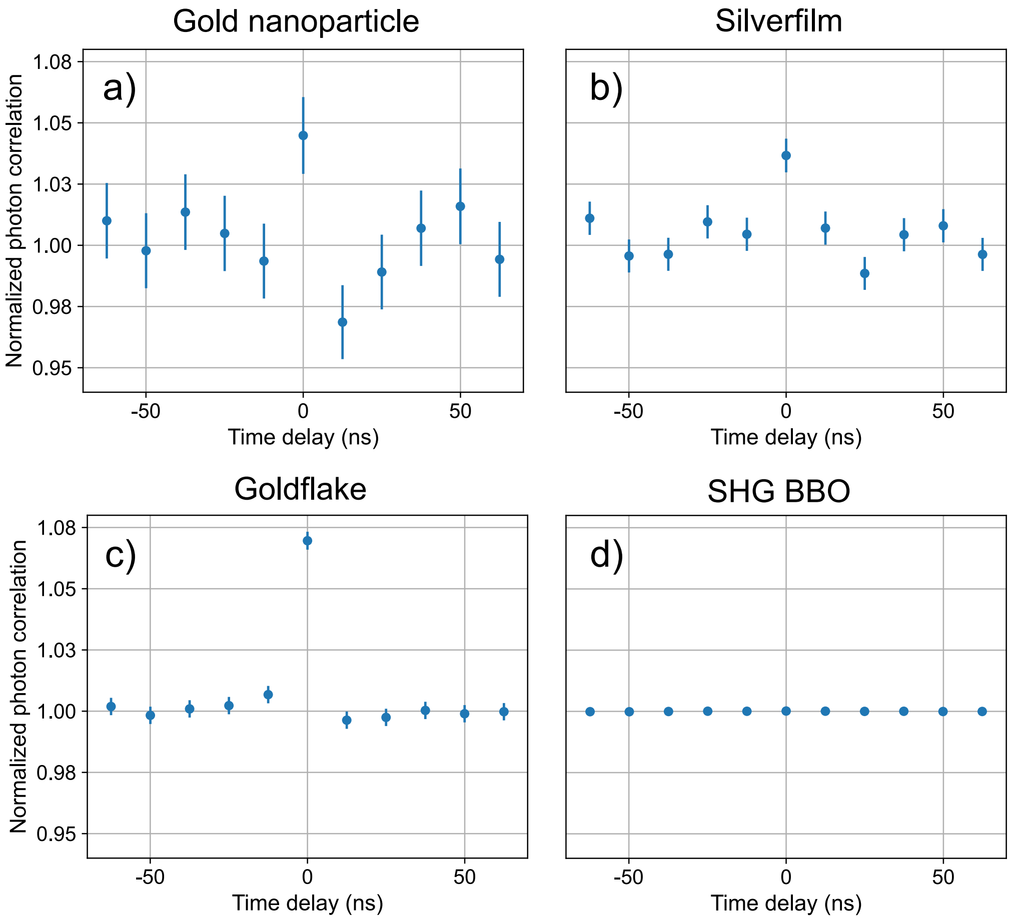

Figure 5.13.: *Measured photon correlations for (a) a gold nanoparticle of 60 nm diameter, (b) a rough silver film, (c) a monocrystalline gold flake. (d) As a sanity check the photon correlation for the second harmonic generated by a phase-matched nonlinear β-barium borate (BBO) crystal.*

are not artifacts due to the data treatment or other unwanted contributions. Although the most challenging to measure, the most interesting result is the photon bunching observed in the gold nanoparticle as one expects to have spatial coherence factor of $C_{\text{spatial}} = 1$. From the bunching peak height of 1.045 ± 0.016 one thus deduces a lifetime of $\tau_p = 1.2 \pm 0.4$ ps, which in the order of the lifetimes reported in [180, 181]. This estimation is about ten higher than expected 180 fs duration expected for inelastic light scattering. This seems therefore to confirm the thermal emission mechanism. I have however neglected here background contributions which lower the peak height and therefore lead to an increased lifetime in the calculations.

The origin of the different bunching peak heights between gold nanoparticle, flake, film and silver is not fully clear to me. It may be due to different hot electron lifetimes which depend upon the excitation power and resonances [180], other factors may be background light and dark counts, or slight misalignment of both APDs leading to a lower spatial coherence factor C_{spatial}.

Predictions for electromigrated tunnel junctions

As seen above, the predictions of the formulas of Table 5.1 fit well with the actual experiments. I will therefore estimate here also the integration times and bunching peak heights if measuring the overbias emission from electromigrated tunnel junctions of Chapter 4.1 instead. Assuming the same coherence time of 0.122 ps, achieved in my measurements with the nonlinear photoluminescence, and using the same detectors with time resolution of 30 ps the expected bunching peak height is $g_2(0) = 1 + C \cdot \frac{\tau_c}{2\tau_d} = 1 + C \cdot 0.0013$, as the overbias emission is a continuous source. Thus, even in the best case, with completely polarized emission and full spatial coherence, the expected bunching peak height is a factor 10 lower with what was achieved experimentally for the nonlinear photoluminescence.

The integration time necessary to observe the photon bunching with a signal to noise ratio SNR = 3 is in such a case assuming count rates (including spectral filtering) at each APD of 10^5 Hz equal to $T_\text{o} = 7.89 \cdot 10^6$ s $\approx$ 90 days. If one would achieve count rates of 10^6 Hz, the integration time would reduce to 21 h. The assumed count rates are however higher than anything I could achieve for the electromigrated gold nanowires. Therefore I decided to not pursue further the photon correlation experiments.

To perform photon correlation measurements with the electromigrated junctions strategies to enhance their lifetime and brightness need to be found. A possible solution might be to embed gaps within optical dielectric resonators with narrow resonances. Instead of filtering the light during its propagation and loosing valuable photons for the photon correlation measurement, due to the Purcell effect [235] most of the photons should be emitted into well-defined optical resonances featuring long coherence times. According to Table 5.1 this would allow a reduction of integration time depending quadratically on the resonance linewidth.

5.3. Conclusion

To summarize, this chapter presented the photon correlation measurements and the observation of photon bunching of the nonlinear photoluminescence in metals. The nonlinear photoluminescence features similar light emission characteristics as the overbias regime of the electromigrated tunnel junctions of Chapter 1. Compared to the overbias photon emission, the nonlinear photoluminescence has several advantages: it is brighter and more stable, and is intrinsically pulsed featuring short lifetimes of about 1 ps. These factors allow us experimentally to observe the photon correlation for the nonlinear photoluminescence, but makes quite challenging to do same for the overbias emission, according to the theoretical predictions.

The bunching peak heights in my measurements are well explained with the theoretical formulas of Table 5.1, indicating a luminescence lifetime about 1 ps previously reported in literature. This suggests that the nonlinear photoluminescence is emitted by a hot electron bath rather than by inelastic light scattering.

Chapter 6.

Different light emission regimes in a single silver junction

The last experimental chapter presents a single device showing all different light emission mechanism (electroluminescence, inelastic tunneling and overbias light emission) encountered so far in this thesis. This device consists of two silver electrodes on top of a glass cover slip separated by a gap and covered by a layer of polymethylmethacrylate (PMMA). Depending on the silver filament growth different emission mechanism are observed.

The filament is reflected in the conductance of the junction. As mentioned in Chapter 4 a pivotal conductance value is the quantum of conductance $G_0 = 7.75 \times 10^{-5}\,\mathrm{S}$. This conductance indicates the presence of a full continuous filament bridging both electrodes with the thinnest part being one atom thick [152]. The measured conductance is thus displayed again in units of G_0.

The samples were kindly provided by our collaborators from ETH Zurich.

6.1. Silver gap junctions

The results presented in this chapter are obtained from two samples. For both we observe light emission for small currents (below 1 µA) and overbias photon emission, i.e photons with higher energy than the standard limit of inelastic tunneling of eq. 2.3. Neither of the samples features a complete set of experimental data, so that experiments from both samples are presented here.

The silver structures were patterned using the same procedure as explained in Chapter 3. First a thin layer of silver (3 nm of chromium and 40 nm of silver and 60 nm of gold for the first sample, 1 nm chromium, 50 nm of silver for the second sample) is deposited on top of a clean glass covers slip. In the next step electron beam lithography is used to define a mask, which allows to etch the silver layer and to obtain the desired structures. Finally on top of the silver a layer of PMMA is spin coated. The electrodes can be accessed by scratching the

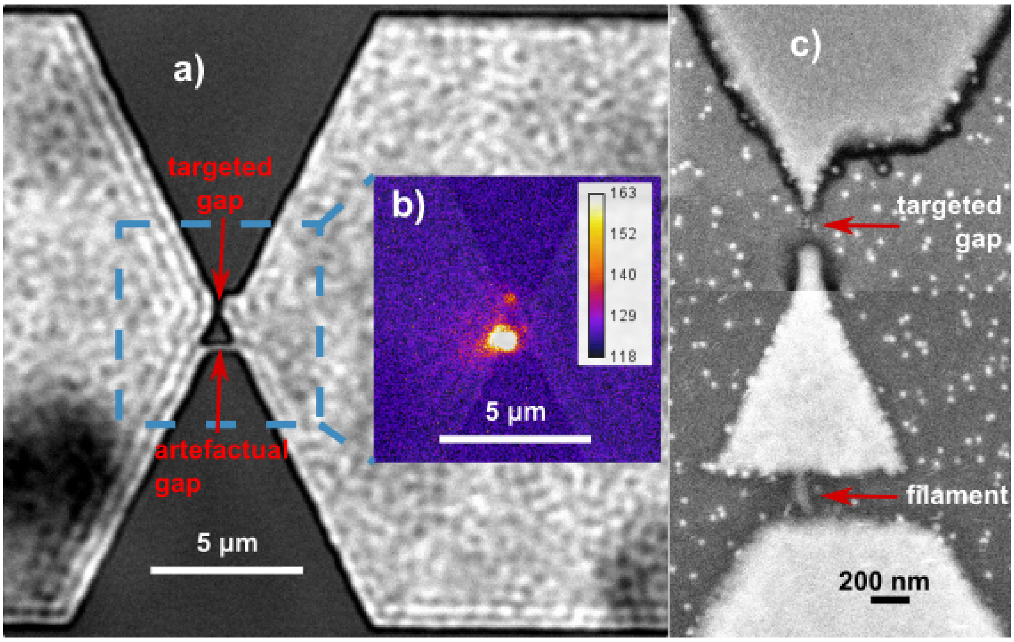

Figure 6.1.: *a) shows a bright field microscope image of a misaligned silver junction with two gaps. b) displays the light emission obtained during a voltage sweep on the junction superimposed on a bright field image of the device. The device emits photons from both gaps. The post activation SEM images show the presence of a grown filament in the lower large gap c).*

PMMA layer with the tungsten tips of the electrical probes.

The design of the silver structures is similar to the memristive devices of Chapter 3. Additionally in the first sample (having the extra 60 nm gold layer) an artefactual shift between e-beam lithography patterning of the gaps and electrodes occurred. This caused an extra 200 nm gap in the devices. This gap is seen optically under a microscope as shown in Figure 6.1 (a). To our surprise, this additional gap does not hinder the function of these devices. The floating potential of the silver triangle in between the two gaps acts as bipolar electrode, as discussed in [79]. The triangle results to be a lower potential than the positive electrode (drain) but at higher potential than the source electrode, allowing current conduction and filament growth in both gaps through the same mechanism of silver ion reduction and oxidation mentioned in Chapter 3.1. A grown filament is clearly visible in post-activation SEM images in the lower gap, Figure 6.1 (c). In the upper gap this filament has probably been destroyed in subsequent measurements. Light can be emitted from both gaps as evidenced in Figure 6.1 (b).

6.2. Light emission and filament growth

The presentation of the experimental results poses a small dilemma. One could either privilege an experimental continuity in the type of excitation used, first voltage sweeps and then pulsed excitation, or a thematic continuity, starting from the smallest gap conductances and increasing towards the quantum of conductance. Both have their merits and drawbacks, here I will chose to follow thematic continuity in the conductances of the junctions.

6.2.1. Wide gap light emission regime

For each pristine device, the electroforming of the silver filament is initiated by performing few voltage sweeps at low compliance currents. Such a sweep is shown in Figure 6.2, obtained on a device having two gaps. After some short current spikes (shown in green in Fig. 6.2 b)), together with photon emission, the compliance current is reached at time -13 s, with the SMU reducing its output voltage below 100 mV for the rest of the bias sweep as the compliance current limit at 5 µA is reached. This is a result of the silver filament growth, reaching a gap conductance G_{gap} near G_0. This high conductance is established in a sudden jump of several order of magnitudes as indicated in Figure 6.2. It implies also a transition in the current transport regime passing from electron hopping between localized trap sites of the two previous chapters to direct tunneling if ($G_{gap} < G_0$) or even a ballistic transport regime if ($G_{gap} \geq G_0$).
Before reaching the compliance limit, the junction shows only a few bursts accompanied by photon emission. During the current and photon spikes the conductance stays between 10^{-4} G_0 and 10^{-2} G_0. As these bursts are quite few and short it is challenging to characterize the emission phenomenon in greater depth, as done in the previous two chapters. The discontinuous light bursts however remind more the light emission observed in the silver-platinum memristors than the light characteristics of the wide-gap gold junctions. This is also seen in the lack of photon counts in the first current spikes around -18 s. For the silver-platinum memristive devices the applied voltage of 2 V is too low for photon emission, whereas in the gold junctions light at is such a voltage is expected.

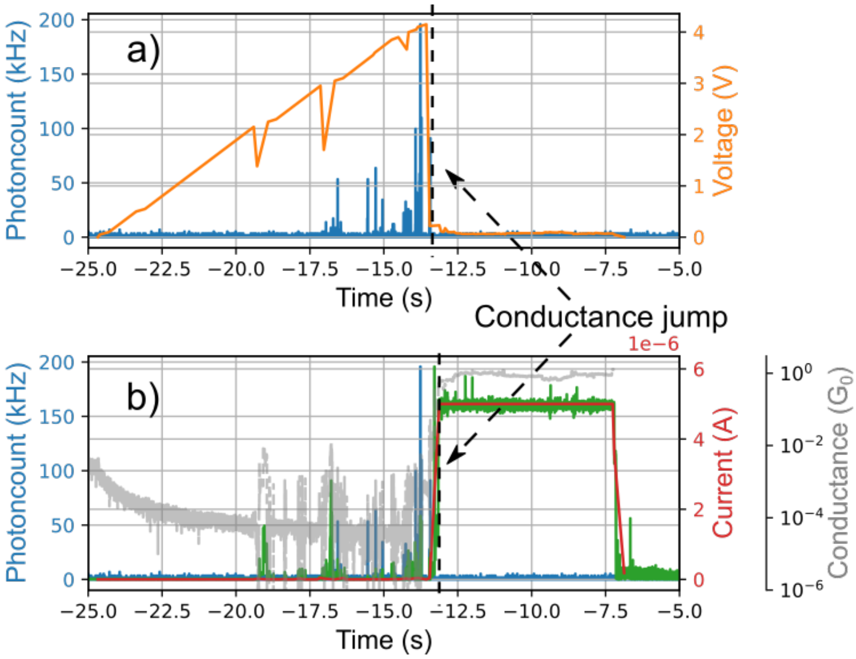

Figure 6.2.: *Voltage sweep and light emission time traces for silver junctions embedded in PMMA at relatively low current. In a), the measured photon counts (blue) and the applied bias (orange) are shown. b) displays alongside the photon counts (blue), the measured current by the SMU (red) and by the TIA (green). The background gray curve shows the junction's conductance (in logarithmic scale) and is displayed in multiples of the quantum of conductance* $G_0 = 7.75 \times 10^{-5}\,\mathrm{S}$. *The initial decrease observed in the conductance is an artifact due to the background current noise of the TIA.*

6.2.2. Light emission by inelastic electron tunneling

In an attempt to limit the filament growth and keep the gap conductance low, while still applying voltages high enough to detect light, we excite the silver to silver junctions with short voltage pulses. Before applying the pulses, several voltage sweeps with a low compliance current (typically 20 nA) are performed. This initiates the filament growth which is subsequently controlled through voltage pulses. The initial width of the voltage pulses is about 10 ms. Quite, rapidly shorter pulse widths of 20 µs are reached while still observing current and light. One such run is shown in Figure 6.3.

The faster junction dynamics, allowing to apply a factor 50 shorter pulses,

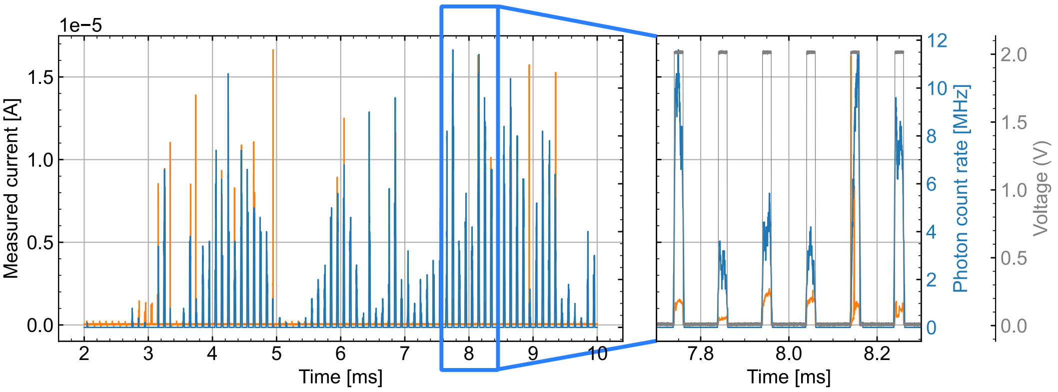

Figure 6.3.: *Pulsed excitation of the silver to silver gaps in PMMA with 100 pulses of* 2 V, 20 µs *duration and 10 kHz repetition rate. The detected photon counts are shown in blue, the measured current is shown in orange and the voltage pulses in gray (on the right only). On the left the full measurement is displayed, whereas the right plot shows a zoom onto a few pulses.*

compared to the wide-gap gold junctions and the silver-platinum memristors, is explained by several factors. Contrary to the the memristive devices (Fig. 3.8) and the wide gap gold junctions in SiO_2 (Fig. 2.29), the current was not measured using the active probe with an input resistance of 1.25 MΩ, but with the TIA having an input resistance of only 100 Ω. This allows on one hand faster electric dynamics[1] and on the other hand higher currents and a larger filament growth without worrying about the voltage drop on the resistance in series on the junction. Secondly the filament growth in the PMMA junctions seems intrinsically faster than for silver or gold in SiO_2. Still fast switching (pulse duration 20 ns) for silver filaments embedded in SiO_2 are possible as shown in [41] in measurements having a 100 kΩ resistance in series.

The light emission in Figure 6.3 is observed almost consistently in every pulse even though the applied voltage is only 2 V. This stable light emission during pulsed excitation permits the acquisition of spectra, shown in Figure 6.4.

To check the consistency of the emission spectra, the acquisition for each voltage was repeated several times. Whereas the magnitude between different runs (at the same applied voltage) changes, the shape and in particular the low wavelength cut-off stay unchanged. The spectral shape and lower wavelength limit however change between spectra acquired with different voltages. In particular,

---

[1] Considering the RC limit in electric circuits.

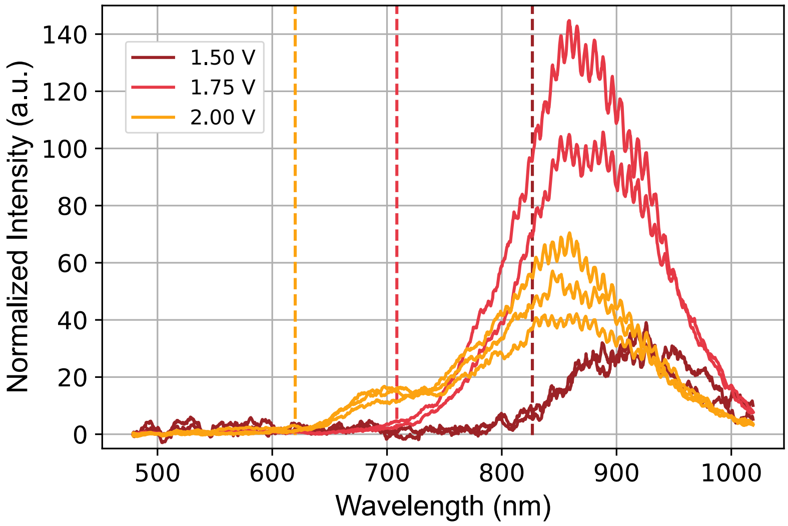

Figure 6.4.: *Spectra taken during a pulsed excitation (500 pulses,* 20 µs *pulsee duration, 10 kHz repetition rate) of the silver gaps in PMMA for different applied biases. The spectra shift with applied bias, and emission is observed until the quantum limit of inelastic tunneling (dashed lines). For a better visibility, all the spectra acquired with 1.5 V pulses have been multiplied by a factor 5.*

the lower wavelength limit follows remarkably well the quantum cut-off of inelastic tunneling for the applied voltage, with $h\nu \leq eV$ (equation 2.3), indicated in the plot with dashed lines. This strongly suggests that light is emitted by inelastic electron tunneling.
It seems thus that by pushing the silver filament grow further and therefore reaching a higher conductance of the gap[2], the emission mechanism transitions from electroluminescence emitted by luminescent charge traps as discussed in the two previous chapters to inelastic electron tunneling. The light should be emitted in the gap between the positive electrode and the filament growing from the opposite electrode.

---

[2] The conductance of the gap for currents of 2 µA and 10 µA is about $1.3 \cdot 10^{-2} G_0$ resp. $6.5 \cdot 10^{-2} G_0$.

6.2.3. Overbias emission

When the conductance of the gap is increased even further, reaching values near the quantum of conductance, the light emission characteristics of the silver gap change yet another time. In this case photon energies $h\nu > eV$ greater than the standard limit of inelastic tunneling (eq. 2.3) are detected, the junction features thus overbias photon emission, as discussed in Chapter 4.

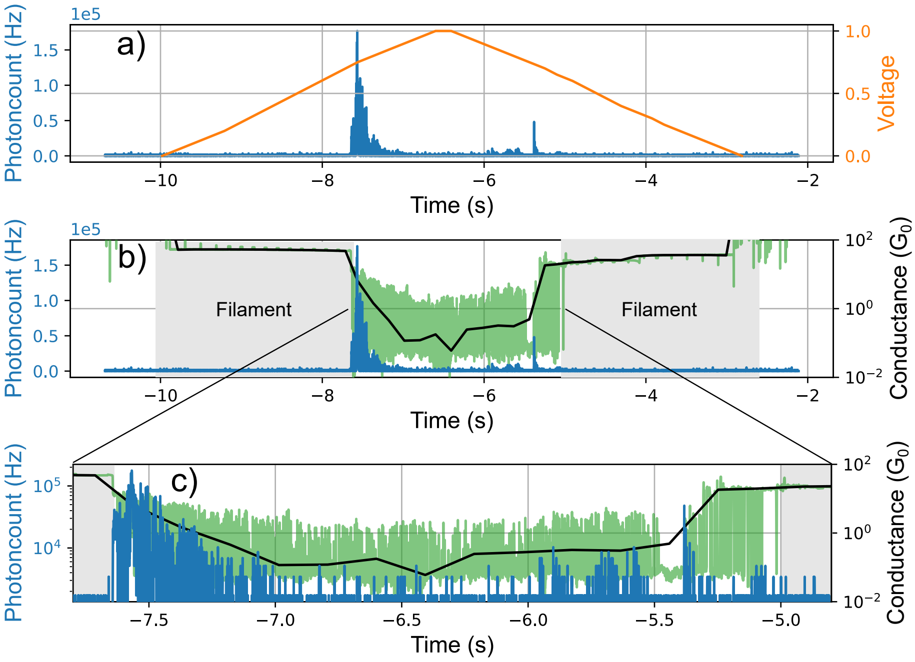

Figure 6.5.: *Overbias photon emission observed in voltage sweeps for silver in PMMA. The photon counts are shown in blue. In a) the applied bias is shown in orange, whereas b) displays the conductance of the device (black using the current measurement from the SMU and green from the TIA), c) features a zoom of b) with the photon counts plotted in a logarithmic scale. The device starts with stable filament connecting both electrodes (gray area in b)). Once sufficient electrical power is dropped on the filament, the latter is partially destroyed (starting at -7.8 s) and photon emission is observed. As can be seen the maximum applied bias is 1 V, this is below the detection limit of the APD, all the photons are thus emitted in the overbias regime. On the backwards sweep the filament forms again.*

This conductance regime can be reached by simply continuing the initial voltage sweeps but allowing successively higher compliance currents. This typically leads to the formation of a continuous silver filament between both electrodes. The filament can however be also broken again by the current flowing through the filament, see Chapter 4.
Such a case is shown in Figure 6.5. Initially the junction shows a grown filament resulting in a high conductance of the junction (gray area Fig. 6.5 b)). During the voltage sweep the filament decreases, leading to a decreased conductance and finally the opening of a gap, at this point the conductance obeys $G_{gap} \leq G_0$. While the conductance is close to G_0 light is detected. Since the applied voltage is below 1.1 V, all the detected photons are emitted into the overbias regime.
The overbias emission regime manifest itself even more clearly in spectra, as shown in Figure 6.6. The spectrum was acquired during a voltage sweep, shown in Fig. 6.6 a). Although, the maximum applied voltage is below 1.5 V, a good fraction of the photons are emitted at shorter wavelengths (left to the dashed line in Fig. 6.6 b)) than expected for the cut-off of inelastic tunneling. Besides violating this cut-off, the spectrum shows a broad distribution with two wide peaks which are probably due to plasmonic resonances of the electrodes and the silver filament, and the efficiency cut-off of the setup.

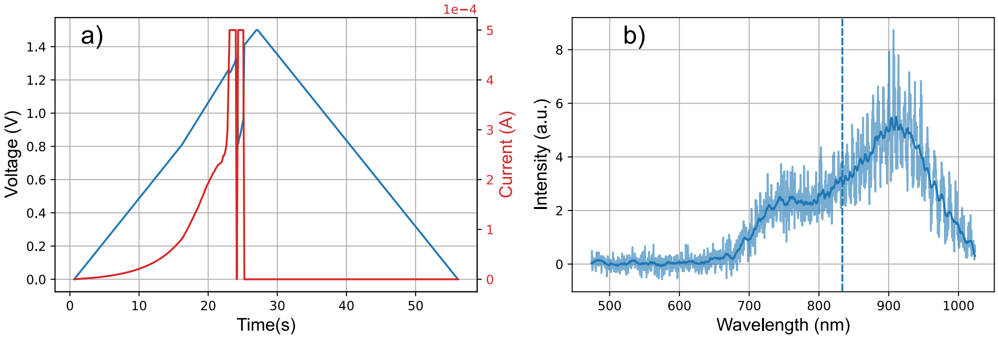

Figure 6.6.: *Photon emission spectrum showing the overbias emission during a bias sweep for silver in PMMA. In a) the voltage sweep with a compliance current of* 500 µA. *In b) the recorded spectrum during the sweep, in pale blue the raw data, the thicker line indicates shows a running average over 25 points. The dashed line indicates the standard quantum limit of inelastic electron tunneling at 1.5 V.*

6.3. Conclusion

Depending on the growth of the silver filament, characterized by different conductance values, different light emission regimes are observed. This is quite analogous to scanning tunneling microscopy luminescence (STML) where the gap conductance is varied by changing the tip height [155]. Here this is achieved for a single planar on chip device, as sketched in Figure 6.7.

At the beginning, with little silver filament growth and a conductance range between $10^{-4}\,G_0$ and $10^{-2}\,G_0$, light is emitted through electroluminescence of luminescent centers, as already reported. By further growth of the silver filament and conductances above $10^{-2}\,G_0$, the electroluminenscence mechanism is replaced by inelastic electron tunneling and finally for a conductance close to G_0, overbias photon emission is observed.

By controlling the filament growth one can therefore tune the light emission mechanism of such junctions. This allows to study and compare these different regimes within one device.

The same series of emission regimes should also be observed in the silver-platinum memristors of Chapter 3, by allowing a similar filament growth and higher conductances.

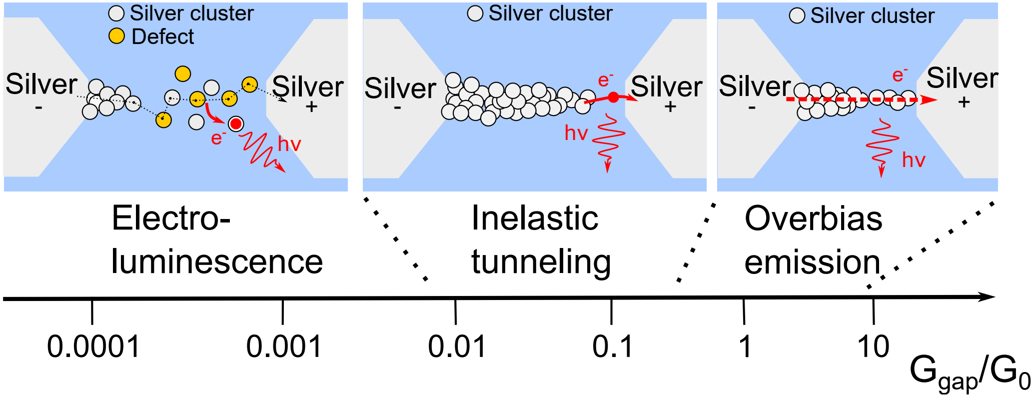

Figure 6.7.: *Sketch of the different emission regimes for silver gaps in PMMA in function of the junction conductance resp. silver filament growth.*

Chapter 7.

Conclusion and outlook

This thesis is a study of electrically-induced light generation and the associated physical phenomena in small metal gaps. These nanometer-size gaps are fabricated using standard clean room techniques. Depending on the junction's gap size, which also evolves in function of the applied electrical field, different emission mechanisms are at play.

This is highlighted in the silver junctions embedded in PMMA of Chapter 6, which, through the voltage induced silver filament growth, show three different conductance and light emission regimes: from the largest gap separation and conductances generating photons by electroluminescence of defects to intermediate separation associated to inelastic electron tunneling to almost ballistic regime enabling overbias photon emission. These results summarize and provide an overview of the light emission studies of thesis.

Electroluminescence in wide gaps

The first type of devices presented in this thesis are the wide gap gold junctions of Chapter 2: two gold electrodes, spaced by 20 nm to 50 nm, on top of a glass cover slips. These junctions are either exposed in air or embedded in a SiO_2 dielectric matrix. Despite this rather simple structure these devices show complex current and light behavior.

Under electrical activation the junctions show a significant increase of conductance, particularly seen in voltage sweeps as hysteresis in the current-voltage plots. Over several cycles the current could be increased from some nA up to some µA. This is a consequence of both a defect creation within the SiO_2 matrix and substrate and the migration of small gold clusters into the gap. The presence of localized electron hopping sites is confirmed by the observation of current noise result of the trap assisted tunneling regime in the junction.

With the appearance of the current light is emitted in the junction's gap with an efficiency in the range of $10^{-7} - 10^{-5}$ photons/e^-. These photons are originated either in SiO_2 defects (Si-clusters) or the gold clusters involved in the current conduction. This is confirmed in the spectral distribution of the photons in discrete peaks and the time evolution of the photon count rates, showing intensity fluctuations, typical of single emitters. By analyzing in greater detail these intensity fluctuations (in particular their photon correlation) the emission of the luminescent centers could be further characterized (active time, brightness, etc.).

Similar structures are investigated in Chapter 3, where the gold electrodes are replaced by silver and platinum tips. Quite expectedly these memristive devices show qualitatively a similar current transport and light emission to the wide-gap gold junctions. There are however are few differences due to the electro-chemical properties of silver-platinum and gold. This allows by comparison to infer the influence of the electrode material on the junction's behavior.

Whereas for a negative bias on the silver electrode only SiO_2 defects contribute to current transport and light emission, for a positive voltage a silver filament, growing from the platinum electrode, contributes to the conductance increase and switching. The same behavior independent on the polarity of the applied voltage allows to attribute the photon emission to the electroluminescence of silicon rich nanoclusters inside the SiO_2 matrix. These luminescent centers, which are created during the electrical stress of the memristive devices, are confirmed by photoluminescence experiments.

The analyses of the evolution of the photon count rates in time, as performed for the wide-gap gold junctions, highlight the difference between both type of devices. In particular the voltage required to observe electroluminescence is considerably higher for the silver-platinum gaps than for the gold junctions. This might imply that for the wide gap gold junctions different defects (few atom gold clusters instead of the silicon rich nanoclusters) are involved in the photon generation process.

Overbias emission

Overbias emission in small metal gaps is presented in Chapter 4. This emission regime is observed in almost closed gap junctions with conductance values close the quantum of conductance $G_0 = 7.75 \times 10^{-5}\,S$. From different experimental systems reaching these conditions and reporting overbias emission, the gaps created by electromigrating of small gold constrictions are used to present the overbias emission experimentally. These junctions were also previously investigated in the group [176].

The second part of the chapter then discusses different hypotheses about the origin of this emission regime. Two main lines of argumentation exist: The first attributes the overbias emission to thermal radiation of an hot electron bath, the second considers coherent multi-electron inelastic tunneling. Between these two poles intermediate hypotheses exist, combining some aspects of both poles. As described in Chapter 5, to discern between these hypotheses and further characterize the overbias emission I aimed at measure its photon correlation. As a first step in this direction I measured the photon correlation of the nonlinear photoluminescence of metals. The nonlinear photoluminescence of metals shows similar characteristics as the overbias emission, and can be explained by a similar mechanism of hot electron radiation.

The photon correlation measurements show consistently photon bunching. This is expected for the thermal radiation mechanism, in particular the bunching peak height is consistent with the dynamics reported in literature [180, 181] and seems to rule faster emission processes.

These photon correlation measurements showed also the importance of a bright light emission and source stability to discern a photon bunching, this prevents currently such measurements on the overbias emission from the electromigrated gold gaps.

Electro-optical antennas

Electrically excited optical antennas are a main research topic of the nano-optic research community in recent years. These antennas are typically excited by inelastic electron tunneling [30, 236] or overbias emission [40, 166], partially studied in this thesis. Both mechanism require small gap sizes and requires thus elaborate fabrication techniques such as electromigration [40, 237], vertical stacking [35, 107], particle self-assembly [38] or the electrophoretic trapping of small gold nanoparticles in a gap [21, 238–241].

In this context the present work adds a more fabrication friendly light source partially integrated with optical antennas by studying the electroluminescence in wide-gap junctions. A similar approach is pursued in [242] depositing a electroluminescent organic layer between similarly spaced electrodes The achieved efficiencies around 10^{-6} photons/e^{-} are however in the same order as our naive approach of simple wide gaps.

Outlook

This thesis provides thus a study of different light emission mechanism in small gap junctions. These junctions could provide scalable, on-chip light sources and can be fabricated with standard clean room technology. It is however clear that at the current stage, the low emission efficiency and relatively low brightness prevent a use in practical applications. For example a typical wide-gap gold junction with an efficiency of 10^{-6} photons/e^{-} driven at 2 V requires already 320 fJ to emit a single photon, while the photon count rate of 10 MHz limits the optical link to similar data rates, which is far below the required 14 GHz to make optical interconnects competitive. Further research on the gap junctions and a deeper understanding of the emission mechanism are therefore necessary to improve these gap junctions.

Quite general two approaches for both the wide gaps and the overbias emission could be pursued. The first would be to tailor the optical environment, similar to what is done for devices relying on inelastic tunneling. This would enhance and shape the light emission through optical resonators and has been partially addressed for the wide-gap gold junctions and the silver-platinum memristors in their electrode design but should be investigated more systematically. The second approach is to tailor the electric and luminescent properties by the choice of materials. For example for the wide gap junctions one could consider a different (perhaps already luminescent) dielectric matrix in the gap, as in [242], which may boost the emission efficiency. Similarly, as already partially investigated in this thesis, one could also consider a specific electrode material (perhaps also a semiconductor) to improve the properties of the gap sources.

It is further interesting to study the reaction of the wide-gaps when excited both electrically and by coherent light. This has been already investigated for smaller gap junctions in STM tips relying on inelastic electron tunneling [243, 244] and for electromigrated junctions with overbias emission [245], featuring in both cases a significant nonlinear light emission increase. This might also help to measure the intrinsic lifetimes of the electroluminescent species. Conversely, when shining light and electrically biasing these gap junctions, also the current and junction conductance could change, as observed in [165] (optical recification) or [23] filament dissolution. This would allow to consider these gaps also as photon detectors.

Appendix A.

Calculation of the bunching peak height and integration times

In this appendix I will show how to evaluate equation 5.11 to obtain the expressions of Table 5.1. Just as a reminder we have:

$$\begin{aligned} C_r = &\int_{\tau_o - \frac{\Delta\tau}{2}}^{\tau_o + \frac{\Delta\tau}{2}} d\tau \int_0^{T_o} dt \int_{-\infty}^{\infty} dt_1 \int_{-\infty}^{\infty} dt_2 \; I_1(t_1) I_2(t_2) \cdot \\ &D_1(t_1 - t) \cdot D_2(t_2 + \tau - t) \end{aligned} \tag{A.1}$$

$$\begin{aligned} C_b(\tau_o) = &\int_{\tau_o - \frac{\Delta\tau}{2}}^{\tau_o + \frac{\Delta\tau}{2}} d\tau \int_0^{T_o} dt \int_{-\infty}^{\infty} dt_1 \int_{-\infty}^{\infty} dt_2 \; I_1(t_1) I_2(t_2) \cdot \\ &D_1(t_1 - t) \cdot D_2(t_2 + \tau - t) \cdot C |g_1(t_1 - t_2)|^2 \end{aligned} \tag{A.2}$$

where $I_{1,2}(t)$ are the time dependent intensities at detector 1 resp. 2 and $D_{1,2}(t)$ are the detectors time response functions normalized such that $\int_{-\infty}^{\infty}(D_1(t)) = 1$. In order to evaluate both integrals both for pulsed and continuous sources I will use the functions shown below.

$$\begin{aligned} |g_1(t)|^2 &= \exp(-\frac{t^2}{\tau_c^2}) \\ D_{1,2}(t) &= \frac{1}{\tau_d \sqrt{2\pi}} \exp(-\frac{t^2}{2\tau_d^2}) \end{aligned} \tag{A.3}$$

I further model the pulsed source as:

$$\begin{aligned} &I_{1,2}(t) = \sum_n \frac{\bar{I}_{1,2}}{f_{\text{rep}}} I_{\text{p}} \left(t - n \cdot \frac{1}{f_{\text{rep}}} \right) \\ &\text{with} \\ &I_{\text{p}}(t) = \begin{cases} 0 & \text{for } t < 0 \\ \frac{1}{\tau_p} e^{-\frac{t}{\tau_p}} & \text{for } t \geq 0 \end{cases} \end{aligned} \tag{A.4}$$

where $\bar{I}_{1,2}$ is the mean detected intensity and I_p is the identical pulse shape (an exponential intensity decay as expected for a thermal source) repeating periodically with frequency f_rep.

A.1. Evaluation of the integrals CW source

Random background counts I now evaluate the integral of equation A.1 by inserting the above defined functions:

$$
\begin{aligned}
C_r =& \int_{\tau_o-\frac{\Delta\tau}{2}}^{\tau_o+\frac{\Delta\tau}{2}} d\tau \int_0^{T_o} dt \int_{-\infty}^{\infty} dt_1 \int_{-\infty}^{\infty} dt_2 \; I_1 \cdot I_2 \cdot \\
& D_1(t_1-t) \cdot D_2(t_2+\tau-t) \\
=& \int_{\tau_o-\frac{\Delta\tau}{2}}^{\tau_o+\frac{\Delta\tau}{2}} d\tau \int_0^{T_o} dt \int_{-\infty}^{\infty} dt_1 \int_{-\infty}^{\infty} dt_2 \; I_1 \cdot I_2 \cdot \\
& \frac{1}{\tau_d\sqrt{2\pi}} \exp\left(-\frac{(t_1-t)^2}{2\tau_d^2}\right) \cdot \frac{1}{\tau_d\sqrt{2\pi}} \exp\left(-\frac{(t_2+\tau-t)^2}{2\tau_d^2}\right) \\
=& \int_{\tau_o-\frac{\Delta\tau}{2}}^{\tau_o+\frac{\Delta\tau}{2}} d\tau \int_0^{T_o} dt \int_{-\infty}^{\infty} d\tilde{t}_1 \int_{-\infty}^{\infty} d\tilde{t}_2 \; I_1 \cdot I_2 \cdot \\
& \frac{1}{t_d\sqrt{2\pi}} \exp\left(-\frac{(\tilde{t}_1)^2}{2t_d^2}\right) \cdot \frac{1}{t_d\sqrt{2\pi}} \exp\left(-\frac{(\tilde{t}_2)^2}{2t_d^2}\right) \\
\overset{\text{Integration } \tilde{t}_2}{=}& \int_{\tau_o-\frac{\Delta\tau}{2}}^{\tau_o+\frac{\Delta\tau}{2}} d\tau \int_0^{T_o} dt \int_{-\infty}^{\infty} d\tilde{t}_1 \; I_1 \cdot I_2 \cdot \; \frac{1}{\tau_d\sqrt{2\pi}} \exp\left(-\frac{(\tilde{t}_1)^2}{2\tau_d^2}\right) \\
\overset{\text{Integration } \tilde{t}_1}{=}& \int_{\tau_o-\frac{\Delta\tau}{2}}^{\tau_o+\frac{\Delta\tau}{2}} d\tau \int_0^{T_o} dt \; I_1 \cdot I_2 \\
=& I_1 \cdot I_2 \cdot \Delta\tau \cdot T_o
\end{aligned}
\tag{A.5}
$$

This result is independent of the actual functions for $D_{1,2}$ as long they are normalized.

Additional bunching counts Again inserting all the functions into Equation A.2 I obtain:

$$\begin{aligned} C_b(\tau_o) = & \int_{\tau_o-\frac{\Delta\tau}{2}}^{\tau_o+\frac{\Delta\tau}{2}} d\tau \int_0^{T_o} dt \int_{-\infty}^{\infty} dt_1 \int_{-\infty}^{\infty} dt_2 \; \bar{I}_1 \bar{I}_2 \cdot \\ & \frac{1}{\tau_d\sqrt{2\pi}} \exp\left(-\frac{(t_1-t)^2}{2\tau_d^2}\right) \cdot \frac{1}{\tau_d\sqrt{2\pi}} \exp\left(-\frac{(t_2+\tau-t)^2}{2\tau_d^2}\right) \cdot C \cdot \exp\left(-\frac{(t_1-t_2)^2}{\tau_c^2}\right) \\ = & \int_{\tau_o-\frac{\Delta\tau}{2}}^{\tau_o+\frac{\Delta\tau}{2}} d\tau \int_0^{T_o} dt \cdot I_1 I_2 \cdot C \cdot \frac{\tau_{coh}}{\tau_{\text{tot}}} \cdot e^{-\frac{\tau^2}{\tau_{\text{tot}}^2}} \end{aligned} \tag{A.6}$$

with $\tau_{\text{tot}} = \sqrt{4\tau_d + \tau_c}$.
At zero time delay and for $\Delta\tau = \tau_{\text{tot}}$ I obtain:

$$\frac{C_b}{C_r} = C \cdot \frac{t_{coh}}{\tau_{\text{tot}}} \cdot \tau_{\text{tot}} \sqrt{2\pi} \frac{\text{erf}(\frac{\Delta\tau}{2\tau_{\text{tot}}})}{\Delta\tau} \simeq C \cdot \frac{\tau_c}{\tau_{\text{tot}}} \cdot 0.96 \tag{A.7}$$

where $\text{erf}(x) = \frac{1}{\sqrt{\pi}} \int_{-x}^{x} dy \cdot e^{-y^2}$ is the so called error function.

A.2. Pulsed source

For the pulsed source I will assume that $\tau_p < \tau_d \ll \frac{1}{f_{\text{rep}}}$. The last inequality allows us to disregard contributions coming from the overlap of two different pulses. Inserting into equation A.1 I obtain then:

$$\begin{aligned} C_r = & \sum_n \int_{\tau_o-\frac{\Delta\tau}{2}}^{\tau_o+\frac{\Delta\tau}{2}} d\tau \int_0^{T_o} dt \int_{-\infty}^{\infty} dt_1 \int_{-\infty}^{\infty} dt_2 \; \frac{\bar{I}_1}{f_{rep}} I_{\text{p}}\left(t_1 - n\cdot\frac{1}{f_{\text{rep}}}\right) \cdot \frac{\bar{I}_2}{f_{rep}} I_{\text{p}}\left(t_2 - n\cdot\frac{1}{f_{\text{rep}}}\right) \cdot \\ & \frac{1}{\tau_d\sqrt{2\pi}} \exp\left(-\frac{(t_1-t)^2}{2\tau_d^2}\right) \cdot \frac{1}{\tau_d\sqrt{2\pi}} \exp\left(-\frac{(t_2+\tau-t)^2}{2\tau_d^2}\right) \end{aligned} \tag{A.8}$$

I evaluate now the integral for a single pulse (or fixed n).
Since in our data processing I integrate over the whole instrument response function, I can set $\Delta\tau = \infty$ in our calculation. Similarly, since the integration time T_o is much larger than the time scale involved for the instrument time response functions and the pulses I will set the integral limits also to infinity.

For a single pulse I then obtain:

$$\begin{aligned}
&\int_{-\infty}^{\infty} d\tau \int_{-\infty}^{\infty} dt \int_{-\infty}^{\infty} dt_1 \int_{-\infty}^{\infty} dt_2 \; \frac{\bar{I}_1}{f_{\text{rep}}} I_{\text{p}}(t_1) \cdot \frac{\bar{I}_2}{f_{\text{rep}}} I_{\text{p}}(t_2) \cdot \\
&\frac{1}{\tau_d \sqrt{2\pi}} \exp\left(-\frac{(t_1 - t)^2}{2\tau_d^2}\right) \cdot \frac{1}{\tau_d \sqrt{2\pi}} \exp\left(-\frac{(t_2 + \tau - t)^2}{2\tau_d^2}\right) \\
=& \int_{-\infty}^{\infty} dt_1 \int_{-\infty}^{\infty} dt_2 \; \frac{\bar{I}_1}{f_{\text{rep}}} I_{\text{p}}(t_1) \cdot \frac{\bar{I}_2}{f_{\text{rep}}} I_{\text{p}}(t_2) \\
=& \frac{\bar{I}_1}{f_{\text{rep}}} \cdot \frac{\bar{I}_2}{f_{\text{rep}}}
\end{aligned}$$

The only thing left to do is to multiply this expression by the number of detected pulses $N_{\text{pul}} = f_{\text{rep}} \cdot T_o$ within the integration time T_o and I obtain:

$$\begin{aligned}
C_r =& N_{\text{pul}} \cdot \frac{\bar{I}_1}{f_{\text{rep}}} \cdot \frac{\bar{I}_2}{f_{\text{rep}}} \\
=& \frac{\bar{I}_1 \cdot \bar{I}_2 \cdot T_o}{f_{\text{rep}}}
\end{aligned} \tag{A.9}$$

The result again does not depend on the specific functions chosen as long as they are normalized and our assumptions are valid.

Additional bunching counts I will only show here the calculation for a single pulse:

$$
\begin{aligned}
C_b(0)_{\text{sp}} =& \int_{-\infty}^{\infty} d\tau \int_{-\infty}^{\infty} dt \int_{-\infty}^{\infty} dt_1 \int_{-\infty}^{\infty} dt_2 \; \frac{\bar{I}_1}{f_{\text{rep}}} I_{\text{p}}\left(t_1\right) \cdot \frac{\bar{I}_2}{f_{\text{rep}}} I_{\text{p}}\left(t_2\right) \cdot \\
& \frac{1}{\tau_d\sqrt{2\pi}} \exp\left(-\frac{(t_1-t)^2}{2\tau_d^2}\right) \cdot \frac{1}{\tau_d\sqrt{2\pi}} \exp\left(-\frac{(t_2+\tau-t)^2}{2\tau_d^2}\right) \cdot \\
& C \cdot \exp\left(-\frac{(t_1-t_2)^2}{\tau_c^2}\right) \\
=& \int_{-\infty}^{\infty} dt_1 \int_{-\infty}^{\infty} dt_2 \; \frac{\bar{I}_1}{f_{\text{rep}}} I_{\text{p}}(t_1) \cdot \frac{\bar{I}_2}{f_{\text{rep}}} I_{\text{p}}(t_2) \cdot C \cdot \exp\left(-\frac{(t_1-t_2)^2}{\tau_c^2}\right) \\
=& \int_{0}^{\infty} dt_1 \int_{0}^{\infty} dt_2 \; \frac{\bar{I}_1 \cdot \bar{I}_2}{f_{\text{rep}}^2} \frac{1}{\tau_p^2} \exp\left(-\frac{t_1}{\tau_p}\right) \exp\left(-\frac{t_2}{\tau_p}\right) \cdot C \cdot \exp\left(-\frac{(t_1-t_2)^2}{\tau_c^2}\right) \\
=& \frac{\bar{I}_1}{f_{\text{rep}}} \cdot \frac{\bar{I}_2}{f_{\text{rep}}} C \cdot \sqrt{\pi} \frac{\tau_c}{2\tau_p} \cdot \left(1-\operatorname{erf}\left(\frac{\tau_c}{2\tau_p}\right)\right) \cdot \exp\left(\frac{\tau_c}{2\tau_p}^2\right) \\
\simeq& \frac{\bar{I}_1}{f_{\text{rep}}} \cdot \frac{\bar{I}_2}{f_{\text{rep}}} C \cdot \sqrt{\pi} \frac{\tau_c}{2\tau_p}
\end{aligned}
\tag{A.10}
$$

where the last approximation is valid for $\frac{\tau_c}{2\tau_p} \ll 1$.
From this I obtain the bunching peak height at zero time delay

$$
\begin{aligned}
\frac{C_b}{C_r} &= C \cdot \sqrt{\pi} \frac{\tau_c}{2\tau_p} \cdot \left(1-\operatorname{erf}\left(\frac{\tau_c}{2\tau_p}\right)\right) \cdot \exp\left(\frac{\tau_c}{2\tau_p}\right)^2 \\
&\simeq C \cdot \sqrt{\pi} \frac{\tau_c}{2\tau_p}
\end{aligned}
\tag{A.11}
$$

If instead of exponential decaying pulses I consider gaussian pulses in equation A.4:

$$
I_{\text{P}}(t) = \frac{1}{\tau_p\sqrt{2\pi}} \exp\left(-\frac{t^2}{2\tau_p^2}\right)
$$

This changes the calculated bunching peak height to:

$$
\frac{C_b}{C_r} = C \cdot \frac{t_{coh}}{\sqrt{4\tau_p^2 + t_{coh}^2}}
\tag{A.12}
$$

A.3. Integration time

The integration time can be estimated following the procedure found in [246]. The noise in the experiment is given by the shot noise fluctuations of the random photon events, the signal are the additional counts of photon pairs with zero time delay the signal to noise ratio SNR is therefore:

$$\mathrm{SNR} = \frac{C_b}{\sqrt{C_r}} = C \cdot \frac{\tau_c}{\tau_{\mathrm{tot}}} \cdot 0.96 \cdot \sqrt{I_1 \cdot I_2 \cdot \tau_{\mathrm{tot}} \cdot T_o}$$

where for the last equality I have inserted the results for a continuous source. By inverting this relation one than extracts the integration time T_o.

A.4. Background contribution

The contribution of additional background counts $B_{1,2}$ at the APDs, coming from stray light or the dark counts of the APDs gives additional random photon pairs without additional bunching counts. This increases the value of C_r by a multiplication factor F_B:

$$F_B = \begin{cases} 1 + \frac{B_1}{I_1} + \frac{B_2}{I_2} + \frac{B_1 B_2}{I_1 I_2} & \text{for CW sources} \\ 1 + \left(\frac{B_1}{\bar{I}_1} + \frac{B_2}{\bar{I}_2}\right) \cdot \Delta\tau \cdot f_{\mathrm{rep}} + \frac{B_1 B_2}{\bar{I}_1 \bar{I}_2} \cdot \Delta\tau \cdot f_{\mathrm{rep}} & \text{for pulsed sources} \end{cases} \tag{A.13}$$

The bunching peak height is divided by F_B, the integration time is multiplied by F_B.

Appendix B.

Spectral brightness and photon correlation measurements

The spectral brightness δ, i.e. the mean number of photons emitted into a coherence volume [214] (or a single photon mode) sets basically the integration time for the photon correlation measurements [246], as will be shown in the following, assuming a series of discrete independent photon modes.

For a mean photon occupation number per photon mode δ and M detected photon modes[1] within a time resolution τ_{r}, and detection efficiency η, one has the following relationships[2] shown in Table B.1.

As can be seen from the formulas the bunching peak height is inversely proportional to the number of photon modes detected (for the discrete case considered here), whereas the integration time itself only depends on the spectral brightness δ of the source and the detection efficiency η,[3] but not on the bunching peak height.

With the above formulas and the measured intensities and bunching peak heights one can estimate the spectral brightness δ, from which I can further calculate a lower limit on the electron temperature.

For the thin gold film of Figure 5.11, I obtained a bunching peak height of 0.038, this gives a detected photon number of $M \approx 26$. The total countrate within the experiment was about $I = 10^5$ Hz, the detector efficiency at 630 nm is about $\eta = 40$ % and $f_{\mathrm{rep}} = 80\,\mathrm{MHz}$. I thus obtain $\delta = \frac{I}{M\eta f_{\mathrm{rep}}} \approx 10^{-4}$.

For blackbody radiation one has that:

$$\delta = \left(\exp\left(\frac{h\nu}{k_{\mathrm{B}}T}\right) - 1\right)^{-1} \simeq \exp\left(-\frac{h\nu}{k_{\mathrm{B}}T}\right) \tag{B.1}$$

---

[1] Assuming that each mode has the same spectral brightness and ideal spatial alignment of both detectors in the experiment

[2] The relationships given here are approximations, considering well separated (both spatially and in frequency) photon modes. Spatial and temporal overlap is not considered here.

[3] I neglect here the contributions of background noise.

		CW	Pulsed
Detected mean intensity	I	$M\frac{\eta\delta}{\tau_\mathrm{r}}$	$M\eta\delta f_\mathrm{rep}$
Random coincidences	C_R	$M^2\eta^2\delta^2\frac{T}{\tau_\mathrm{r}}$	$M^2\eta^2\delta^2 T f_\mathrm{rep}$
Extra bunching coincidences	C_B	$M\eta^2\delta^2\frac{T}{\tau_\mathrm{r}}$	$M\eta^2\delta^2 T f_\mathrm{rep}$
Bunching peak height	$g_2(0)-1$	$\frac{1}{M}$	$\frac{1}{M}$
Integration time	T	$\frac{\mathrm{SNR}^2}{\eta^2\delta^2}\cdot\tau_\mathrm{r}$	$\frac{\mathrm{SNR}^2}{\eta^2\delta^2}\cdot\frac{1}{f_\mathrm{rep}}$

Table B.1.: *Theoretical expectations of photon pair count rates, bunching peak height and integration time for pulsed and continuous chaotic sources, emitting with a spectral brightness or mean photon occupation number per photon mode δ.*

assuming that $h\nu \gg k_\mathrm{B}T$. Which can be inverted to obtain the temperature T:

$$T = -\frac{h\nu}{k_\mathrm{B}}\frac{1}{\ln(\delta)} \approx \frac{1.97}{8.617\cdot 10^{-5}}\frac{1}{9.17}\ \mathrm{K} \approx 2.5\cdot 10^3\ \mathrm{K} \tag{B.2}$$

This seems a reasonable electron temperature, especially for all the excitation power put on the sample. In the estimation above, I considered a perfect blackbody, for a reflecting metal one would need to take into account smaller photon coupling and would therefore obtain even a higher electron temperature. This dependence is however logarithmic, for example assuming only 10% percent photon coupling would lead in our case to a 4/3 times higher electron temperature.

Note on the derivation of the expression in table B.1 In order to derive the expressions above I consider here each photon mode as a spatially and temporally localized wavepacket, with a time duration of the wavepacket of τ_r greater than the time resolution of the detector. Each mode is distinguishable from any other mode either by frequency, polarization or wavevector, with negligible overlap between the different modes.
The mean photon number detected in an interval τ_r is thus given by sum of the mean photon number of each mode δ_n multiplied by the detection efficiency $I = \sum_{n=0}^{M}\delta_n\eta$. For a pulsed source as long as τ_r is smaller than the repetition period, it is replaced by the latter in the formula for the mean intensity.

From this it is not difficult to calculate the number or random coincidences detected in an interval by using the formula from Table 5.1.
Since all photon modes are assumed to be independent of each other, there is no photon correlation between different photon modes. The number of additional photon pairs scales thus linearly in the number of photon modes, $C_{\mathrm{B,tot}} = \sum_{n=0}^{M} C_{\mathrm{B,n}} = \sum_{n=0}^{M} \delta_n^2 \eta^2 \frac{T}{\tau_{\mathrm{r}}}$, where $C_{\mathrm{B,n}}$ are the extra bunching counts for each photon mode.

Appendix C.

Some remarks about instrumentation and setup

For a better overview about some of the conditions and limitations of the experiments performed for this thesis work, this appendix presents two characteristics of the used instrumentation: its wavelength dependent photon detection efficiency and its time resolution. For more detail, each instrument is named in the main text and its specification sheet can be generally found by a simple internet search.

Wavelength dependent detection efficiency

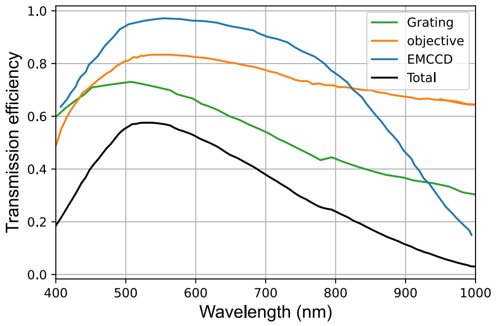

Figure C.1.: *The spectral detection efficiency in function of wavelength for the measurements of Chapters 2, 3, 4* and *6.*

The wavelength dependent detection efficiency of spectral acquisitions is shown in Figure C.1. The black curve shows the total detection efficiency of the setup, resulting of a combination of the different elements used: a EM-CCD camera, a grating and the oil immersion objective. This curves are references provided by the manufacturers.

The camera (EMCCD, blue curve) shows for example a clear detection cut-off towards 1000 nm. This limit is also present in the used APDs and was invoked throughout the main text.

The total detection efficiency is just a product of all the transmission/ detection efficiencies, and would correspond to the measured spectra of a white light source having a flat wavelength independent spectrum.

It is important to remark here, that none of the spectra presented in this thesis have been corrected by the total detection efficiency. The true emission therefore has more prominent long wavelength contributions, as detected for example in the spectra of Figure 2.23. This also leads to an underestimation of the hot electron temperature in Figure 5.6 a), which does not change the power law behavior in Figure 5.6 b), except for modifying its exponent.

Temporal resolution of the measurements

The temporal resolution of this thesis' experiments is limited by different factors. First it might be limited by time resolution of the instruments (or APDs). In particular the APDs (Micro Photon Devices, PD 050 CTC) used in Chapter 5 have time resolution of about 30 ps, this resolution is seen as the FWHM of the autocorrelation curve in Figure 5.10 b). For all the other measurements a different type of APD (SPCM-ARQH) was used, which has a lower time resolution of 350 ps. Similarly for the electrical measurements, the TIA has a time resolution of 4.5 µs, whereas the active probe of 40 ps.

However such a high time resolutions result also in large data files even for relatively short data acquisitions. This is why typically for longer measurements, an integrated time resolution of 1-100 µs was set on the Lock in amplifier when used as an oscilloscope.

List of Figures

List of Tables

Bibliography

[1] Apple, "Introducing m1 pro and m1 max: the most powerful chips apple has ever built," 2021. [Online; accessed 27-January-2022].

[2] IBM, "Ibm unveils world's first 2 nanometer chip technology, opening a new frontier for semiconductors," 2021. [Online; accessed 27-January-2022].

[3] I. L. Markov, "Limits on fundamental limits to computation," *Nature*, vol. 512, no. 7513, pp. 147–154, 2014.

[4] D. A. Miller, "Device requirements for optical interconnects to CMOS silicon chips," *Optics InfoBase Conference Papers*, vol. 97, no. 7, 2010.

[5] D. A. Miller, "Attojoule Optoelectronics for Low-Energy Information Processing and Communications," *Journal of Lightwave Technology*, vol. 35, no. 3, pp. 346–396, 2017.

[6] D. Miller and H. Ozaktas, "Limit to the Bit-Rate Capacity of Electrical Interconnects from the Aspect Ratio of the System Architecture," *Journal of Parallel and Distributed Computing*, vol. 41, pp. 42–52, feb 1997.

[7] W. Van Heddeghem, S. Lambert, B. Lannoo, D. Colle, M. Pickavet, and P. Demeester, "Trends in worldwide ict electricity consumption from 2007 to 2012," *Computer Communications*, vol. 50, pp. 64–76, 2014. Green Networking.

[8] J. Morley, K. Widdicks, and M. Hazas, "Digitalisation, energy and data demand: The impact of internet traffic on overall and peak electricity consumption," *Energy Research and Social Science*, vol. 38, pp. 128–137, 2018.

[9] E. Masanet, A. Shehabi, N. Lei, S. Smith, and J. Koomey, "Recalibrating global data center energy-use estimates," *Science*, vol. 367, no. 6481, pp. 984–986, 2020.

[10] Iea, "Data centres and data transmission networks – analysis," Nov 2021. [Online; accessed 03-May-2022].

[11] A. H. Atabaki, S. Moazeni, F. Pavanello, H. Gevorgyan, J. Notaros, L. Alloatti, M. T. Wade, C. Sun, S. A. Kruger, H. Meng, K. Al Qubaisi, I. Wang, B. Zhang, A. Khilo, C. V. Baiocco, M. A. Popović, V. M. Stojanović, and R. J. Ram, "Integrating photonics with silicon nanoelectronics for the next generation of systems on a chip," *Nature*, vol. 556, pp. 349–354, apr 2018.

[12] D. A. Miller, "Rationale and challenges for optical interconnects to electronic chips," *Proceedings of the IEEE*, vol. 88, no. 6, pp. 728–749, 2000.

[13] J. Goodman, F. Leonberger, S.-Y. Kung, and R. Athale, "Optical interconnections for vlsi systems," *Proceedings of the IEEE*, vol. 72, no. 7, pp. 850–866, 1984.

[14] J. Bashir, E. Peter, and S. R. Sarangi, "A survey of on-chip optical interconnects," *ACM Computing Surveys*, vol. 51, no. 6, pp. 1–35, 2019.

[15] X. Li and Q. Gu, "High-speed on-chip light sources at the nanoscale," *Advances in Physics: X*, vol. 4, no. 1, 2019.

[16] B. Romeira and A. Fiore, "Physical Limits of NanoLEDs and Nanolasers for Optical Communications," *Proceedings of the IEEE*, vol. 108, no. 5, pp. 735–748, 2020.

[17] D. K. Gramotnev and S. I. Bozhevolnyi, "Plasmonics beyond the diffraction limit," *Nature Photonics*, vol. 4, pp. 83–91, Feb 2010.

[18] J. B. Khurgin, "How to deal with the loss in plasmonics and metamaterials," *Nature Nanotechnology*, vol. 10, no. 1, pp. 2–6, 2015.

[19] M. Ochs, L. Zurak, E. Krauss, J. Meier, M. Emmerling, R. Kullock, and B. Hecht, "Nanoscale electrical excitation of distinct modes in plasmonic waveguides," *Nano Letters*, vol. 21, pp. 4225–4230, May 2021.

[20] L. Novotny and N. van Hulst, "Antennas for light," *Nature Photonics*, vol. 5, pp. 83–90, feb 2011.

[21] R. Kullock, M. Ochs, P. Grimm, M. Emmerling, and B. Hecht, "Electrically-driven Yagi-Uda antennas for light," *Nature Communications*, vol. 11, no. 1, pp. 5–11, 2020.

[22] U. Koch, C. Uhl, H. Hettrich, Y. Fedoryshyn, C. Hoessbacher, W. Heni, B. Baeuerle, B. I. Bitachon, A. Josten, M. Ayata, H. Xu, D. L. Elder, L. R. Dalton, E. Mentovich, P. Bakopoulos, S. Lischke, A. Krüger, L. Zimmermann, D. Tsiokos, N. Pleros, M. Möller, and J. Leuthold, "A monolithic bipolar CMOS electronic–plasmonic high-speed transmitter," *Nature Electronics*, vol. 3, no. 6, pp. 338–345, 2020.

[23] A. Emboras, J. Niegemann, P. Ma, C. Haffner, A. Pedersen, M. Luisier, C. Hafner, T. Schimmel, and J. Leuthold, "Atomic Scale Plasmonic Switch," *Nano Letters*, vol. 16, no. 1, pp. 709–714, 2016.

[24] J. Lavrencik, S. Varughese, V. A. Thomas, J. S. Gustavsson, E. Haglund, A. Larsson, and S. E. Ralph, "102Gbps PAM-2 over 50m OM5 Fiber using 850nm Multimode VCSELs," *2019 IEEE Photonics Conference, IPC 2019 - Proceedings*, vol. 2, no. 1, pp. 1–2, 2019.

[25] K. Takeda, T. Sato, A. Shinya, K. Nozaki, W. Kobayashi, H. Taniyama, M. Notomi, K. Hasebe, T. Kakitsuka, and S. Matsuo, "Few-fJ/bit data transmissions using directly modulated lambda-scale embedded active region photonic-crystal lasers," *Nature Photonics*, vol. 7, no. 7, pp. 569–575, 2013.

[26] V. Dolores-Calzadilla, B. Romeira, F. Pagliano, S. Birindelli, A. Higuera-Rodriguez, P. J. van Veldhoven, M. K. Smit, A. Fiore, and D. Heiss, “Waveguide-coupled nanopillar metal-cavity light-emitting diodes on silicon,” *Nature Communications*, vol. 8, p. 14323, apr 2017.

[27] L. Wojszvzyk, A. Nguyen, A. L. Coutrot, C. Zhang, B. Vest, and J. J. Greffet, “An incandescent metasurface for quasimonochromatic polarized mid-wave infrared emission modulated beyond 10 MHz,” *Nature Communications*, vol. 12, no. 1, pp. 1–8, 2021.

[28] Y. D. Kim, Y. Gao, R. J. Shiue, L. Wang, O. B. Aslan, M. H. Bae, H. Kim, D. Seo, H. J. Choi, S. H. Kim, A. Nemilentsau, T. Low, C. Tan, D. K. Efetov, T. Taniguchi, K. Watanabe, K. L. Shepard, T. F. Heinz, D. Englund, and J. Hone, “Ultrafast Graphene Light Emitters,” *Nano Letters*, vol. 18, no. 2, pp. 934–940, 2018.

[29] R. J. Shiue, Y. Gao, C. Tan, C. Peng, J. Zheng, D. K. Efetov, Y. D. Kim, J. Hone, and D. Englund, “Thermal radiation control from hot graphene electrons coupled to a photonic crystal nanocavity,” *Nature Communications*, vol. 10, no. 1, pp. 1–7, 2019.

[30] M. Parzefall and L. Novotny, “Optical antennas driven by quantum tunneling: a key issues review,” *Reports on progress in physics. Physical Society (Great Britain)*, vol. 82, no. 11, p. 112401, 2019.

[31] J. Lambe and S. L. McCarthy, “Light Emission from Inelastic Electron Tunneling,” *Physical Review Letters*, vol. 37, pp. 923–925, oct 1976.

[32] D. C. Tsui, “Observations of Surface Plasmon Excitation by Tunneling Electrons in GaAs-Pb Tunnel Junctions,” *Physical Review Letters*, vol. 22, pp. 293–295, feb 1969.

[33] K. L. Ngai and E. N. Economou, “Theory of Electron-Surface-Plasmons Interactions in Tunneling, Low-Energy-Electron Diffraction, and Photoemission,” *Physical Review B*, vol. 4, pp. 2132–2146, oct 1971.

[34] P. Février and J. Gabelli, “Tunneling time probed by quantum shot noise,” *Nature Communications*, vol. 9, no. 1, pp. 1–8, 2018.

[35] M. Parzefall, P. Bharadwaj, A. Jain, T. Taniguchi, K. Watanabe, and L. Novotny, “Antenna-coupled photon emission from hexagonal boron nitride tunnel junctions,” *Nature Nanotechnology*, vol. 10, pp. 1058–1063, dec 2015.

[36] M. Parzefall and L. Novotny, “Light at the End of the Tunnel,” *ACS Photonics*, vol. 5, no. 11, pp. 4195–4202, 2018.

[37] A. V. Uskov, J. B. Khurgin, I. E. Protsenko, I. V. Smetanin, and A. Bouhelier, “Excitation of plasmonic nanoantennas by nonresonant and resonant electron tunnelling,” *Nanoscale*, vol. 8, no. 30, pp. 14573–14579, 2016.

[38] H. Qian, S. W. Hsu, K. Gurunatha, C. T. Riley, J. Zhao, D. Lu, A. R. Tao, and Z. Liu, “Efficient light generation from enhanced inelastic electron tunnelling,” *Nature Photonics*, vol. 12, no. 8, pp. 485–488, 2018.

[39] H. Qian, S. Li, S.-W. Hsu, C.-F. Chen, F. Tian, A. R. Tao, and Z. Liu, “Highly-efficient electrically-driven localized surface plasmon source enabled by resonant inelastic electron tunneling,” *Nature Communications*, vol. 12, p. 3111, dec 2021.

[40] M. Buret, A. V. Uskov, J. Dellinger, N. Cazier, M. M. Mennemanteuil, J. Berthelot, I. V. Smetanin, I. E. Protsenko, G. Colas-Des-Francs, and A. Bouhelier, “Spontaneous Hot-Electron Light Emission from Electron-Fed Optical Antennas,” *Nano Letters*, vol. 15, no. 9, pp. 5811–5818, 2015.

[41] B. Cheng, A. Emboras, Y. Salamin, F. Ducry, P. Ma, Y. Fedoryshyn, S. Andermatt, M. Luisier, and J. Leuthold, “Ultra compact electrochemical metallization cells offering reproducible atomic scale memristive switching,” *Communications Physics*, vol. 2, no. 1, pp. 1–9, 2019.

[42] M. Buret, I. V. Smetanin, A. V. Uskov, G. Colas des Francs, and A. Bouhelier, “Effect of quantized conductivity on the anomalous photon emission radiated from atomic-size point contacts,” *Nanophotonics*, vol. 9, pp. 413–425, feb 2020.

[43] P.-J. Peters, F. Xu, K. Kaasbjerg, G. Rastelli, W. Belzig, and R. Berndt, “Quantum Coherent Multielectron Processes in an Atomic Scale Contact,” *Physical Review Letters*, vol. 119, p. 066803, aug 2017.

[44] K. Malchow and A. Bouhelier, “Photon bunching of the nonlinear photoluminescence emitted by plasmonics metals,” *Journal of the Optical Society of America B*, vol. 38, p. 576, feb 2021.

[45] G. Dearnaley, A. M. Stoneham, and D. V. Morgan, “Electrical phenomena in amorphous oxide films,” *Reports on Progress in Physics*, vol. 33, no. 3, pp. 1129–1191, 1970.

[46] T. W. Hickmott, “Potential distribution and negative resistance in thin oxide films,” *Journal of Applied Physics*, vol. 35, no. 9, pp. 2679–2689, 1964.

[47] C. Barriac, P. Pinard, and F. Davoine, “Étude des propriétés électriques des structures Al-Al2O3–métal,” *physica status solidi (b)*, vol. 34, no. 2, pp. 621–633, 1969.

[48] J. G. Simmons and R. R. Verderber, “New conduction and reversible memory phenomena in thin insulating films,” *Proceedings of the Royal Society of London. Series A. Mathematical and Physical Sciences*, vol. 301, pp. 77–102, oct 1967.

[49] I. Emmer, “Conducting filaments and voltage-controlled negative resistance in Al-Al2O3-Au structures with amorphous dielectric,” *Thin Solid Films*, vol. 20, no. 1, pp. 43–52, 1974.

[50] H. Pagnia and N. Sotnik, “Bistable switching in electroformed metal–insulator–metal devices,” *Physica Status Solidi (a)*, vol. 108, pp. 11–65, jul 1988.

[51] R. Blessing, H. Pagnia, and N. Sotnik, “The electroforming process in MIM diodes,” *Thin Solid Films*, vol. 85, pp. 119–128, nov 1981.

[52] M. Bischoff and H. Pagnia, “Electroluminescence spectra from gold island structure thin films,” *Thin Solid Films*, vol. 29, pp. 303–312, oct 1975.

[53] R. Blessing and H. Pagnia, “Forming process, i-v characteristics and switching in gold island films,” *Thin Solid Films*, vol. 52, pp. 333–341, aug 1978.

[54] H. Biederman and J. Plášek, “The electroluminescence and associated phenomena in metal-insulator-metal structures and in discontinuous metal films,” *Thin Solid Films*, vol. 47, pp. L1–L4, dec 1977.

[55] M. Bischoff, V. Olt, and H. Pagnia, “Electroluminescence spectra of discontinuous conducting films,” *Thin Solid Films*, vol. 165, no. 1, pp. 49–54, 1988.

[56] D. Wolters, “Tunnelling in thin SiO 2,” *Philosophical Transactions of the Royal Society of London. Series A: Mathematical, Physical and Engineering Sciences*, vol. 354, pp. 2327–2350, oct 1996.

[57] D. R. Wolters and A. T. A. Zegers-van Duynhoven, “Electronic Charge Transport in Thin SiO2 Films,” in *The Physics and Technology of Amorphous SiO2*, pp. 391–409, Boston, MA: Springer US, 1988.

[58] S. Lombardo, J. H. Stathis, B. P. Linder, K. L. Pey, F. Palumbo, and C. H. Tung, “Dielectric breakdown mechanisms in gate oxides,” *Journal of Applied Physics*, vol. 98, no. 12, pp. 1–36, 2005.

[59] Z. A. Weinberg, G. W. Rubloff, and E. Bassous, “Transmission, photoconductivity, and the experimental band gap of thermally grown SiO2 films,” *Physical Review B*, vol. 19, no. 6, pp. 3107–3117, 1979.

[60] L. Quattropani, I. Maggio-Aprile, P. Niedermann, and Ø. Fischer, “Ballistic-electron-emission-microscopy studies on-type Si(100) and-type Si(100) structures with very thin oxides,” *Physical Review B - Condensed Matter and Materials Physics*, vol. 57, no. 11, pp. 6623–6628, 1998.

[61] K. Inoue, M. Yagi, M. Ito, T. Ito, and J. I. Shirakashi, “Investigation of electromigration induced by field emission current flowing through Au nanogaps in ambient air,” *Journal of Applied Physics*, vol. 122, no. 8, 2017.

[62] D. Arnold, E. Cartier, and D. J. DiMaria, “Theory of high-field electron transport and impact ionization in silicon dioxide,” *Physical Review B*, vol. 49, no. 15, pp. 10278–10297, 1994.

[63] P. E. Nicollian, *Physics of trap generation and electrical breakdown in ultra-thin SiO and SiON gate dielectric materials.* PhD thesis, University of Twente, 2007.

[64] S. Menzel and R. Waser, *Mechanism of memristive switching in OxRAM.* Elsevier Ltd., second edi ed., 2019.

[65] C. Funck and S. Menzel, “Comprehensive Model of Electron Conduction in Oxide-Based Memristive Devices,” *ACS Applied Electronic Materials*, no. Vcm, 2021.

[66] J. Ralph and J. Woodcock, “A new filamentary model for voltage formed amorphous oxide films,” *Journal of Non-Crystalline Solids*, vol. 7, pp. 236–250, apr 1972.

[67] B. W. Fowler, Y. F. Chang, F. Zhou, Y. Wang, P. Y. Chen, F. Xue, Y. T. Chen, B. Bringhurst, S. Pozder, and J. C. Lee, “Electroforming and resistive switching in silicon dioxide resistive memory devices,” *RSC Advances*, vol. 5, no. 27, pp. 21215–21236, 2015.

[68] K. Maturova, S. U. Nanayakkara, J. M. Luther, and J. Van De Lagemaat, “Fast current blinking in individual PbS and CdSe quantum dots,” *Nano Letters*, vol. 13, pp. 2338–2345, jun 2013.

[69] T. P. Chen, M. S. Tse, X. Zeng, and S. Fung, “On the switching behaviour of post-breakdown conduction in ultra-thin SiO2 films,” *Semiconductor Science and Technology*, vol. 16, no. 9, pp. 793–797, 2001.

[70] A. Cester, L. Bandiera, G. Ghidini, I. Bloom, and A. Paccagnella, “Soft breakdown current noise in ultra-thin gate oxides,” *Solid-State Electronics*, vol. 46, no. 7, pp. 1019–1025, 2002.

[71] O. Brière, J. A. Chroboczek, and G. Ghibaudo, “Random telegraph signal in the quasi-breakdown current of MOS capacitors,” *European Solid-State Device Research Conference*, no. ii, pp. 759–762, 1996.

[72] E. Miranda and J. Suñé, “Electron transport through broken down ultra-thin SiO2 layers in MOS devices,” *Microelectronics Reliability*, vol. 44, no. 1, pp. 1–23, 2004.

[73] C. N. Peng, C. W. Wang, T. C. Chan, W. Y. Chang, Y. C. Wang, H. W. Tsai, W. W. Wu, L. J. Chen, and Y. L. Chueh, “Resistive switching of Au/ZnO/Au resistive memory: An in situ observation of conductive bridge formation,” *Nanoscale Research Letters*, vol. 7, pp. 1–6, 2012.

[74] J. R. Szdeon and R. M. Handy, “Migration of Gold and Nickel Ions in Thin Films of Silicon Dioxide,” in *Fifth Annual Symposium on the Physics of Failure in Electronics*, pp. 292–309, IEEE, nov 1966.

[75] C. J. Madams, D. V. Morgan, and M. J. Howes, “Migration of gold atoms through thin silicon oxide films,” *Journal of Applied Physics*, vol. 45, no. 11, pp. 5088–5090, 1974.

[76] E. Cattaruzza, F. Gonella, S. Ali, C. Sada, and A. Quaranta, “Silver and gold doping of SiO2 glass by solid-state field-assisted diffusion,” *Journal of Non-Crystalline Solids*, vol. 355, no. 18-21, pp. 1136–1139, 2009.

[77] S. G. Bratsch, “Standard Electrode Potentials and Temperature Coefficients in Water at 298.15 K,” *Journal of Physical and Chemical Reference Data*, vol. 18, pp. 1–21, jan 1989.

[78] M. Lübben and I. Valov, “Active Electrode Redox Reactions and Device Behavior in ECM Type Resistive Switching Memories,” *Advanced Electronic Materials*, vol. 5, no. 9, pp. 1–8, 2019.

[79] Y. Yang, P. Gao, L. Li, X. Pan, S. Tappertzhofen, S. Choi, R. Waser, I. Valov, and W. D. Lu, "Electrochemical dynamics of nanoscale metallic inclusions in dielectrics," *Nature Communications*, vol. 5, no. May, 2014.

[80] K. Patel, J. Cottom, M. Bosman, A. J. Kenyon, and A. L. Shluger, "An oxygen vacancy mediated Ag reduction and nucleation mechanism in SiO2 RRAM devices," *Microelectronics Reliability*, vol. 98, no. May, pp. 144–152, 2019.

[81] H. Park, A. K. Lim, A. P. Alivisatos, J. Park, and P. L. McEuen, "Fabrication of metallic electrodes with nanometer separation by electromigration," *Applied Physics Letters*, vol. 75, no. 2, pp. 301–303, 1999.

[82] A. Mangin, A. Anthore, M. L. Della Rocca, E. Boulat, and P. Lafarge, "Transport through metallic nanogaps in an in-plane three-terminal geometry," *Journal of Applied Physics*, vol. 105, no. 1, pp. 1–6, 2009.

[83] F. Wang, J. Fang, S. Chang, S. Qin, X. Zhang, and H. Xu, "Room temperature Coulomb blockade mediated field emission via self-assembled gold nanoparticles," *Physics Letters, Section A: General, Atomic and Solid State Physics*, vol. 381, no. 5, pp. 476–480, 2017.

[84] S. Tani, M. Ito, M. Yagi, M. Shimada, K. Sakai, K. Minami, and J. I. Shirakashi, "Single-electron tunneling effects in electromigrated Coulomb Island between Au nanogaps," *2018 IEEE 13th Nanotechnology Materials and Devices Conference, NMDC 2018*, pp. 1–4, 2019.

[85] M. Parzefall, Á. Szabó, T. Taniguchi, K. Watanabe, M. Luisier, and L. Novotny, "Light from van der Waals quantum tunneling devices," *Nature Communications*, vol. 10, no. 1, pp. 1–9, 2019.

[86] Y. Uehara, J. Watanabe, S. Fujikawa, and S. Ushioda, "Light-emission mechanism of Si-MOS tunnel junctions," *Physical Review B*, vol. 51, no. 4, pp. 2229–2238, 1995.

[87] K. De Kort, P. Damink, and H. Boots, "Spectrum emitted by hot electrons in p-i-n cold cathodes," *Physical Review B*, vol. 48, no. 16, pp. 11912–11920, 1993.

[88] C. Itoh, T. Suzuki, and N. Itoh, "Luminescence and defect formation in undensified and densified amorphous SiO2," *Physical Review B*, vol. 41, pp. 3794–3799, feb 1990.

[89] A. Irrera, F. Iacona, I. Crupi, C. D. Presti, G. Franzò, C. Bongiorno, D. Sanfilippo, G. Di Stefano, A. Piana, P. G. Fallica, A. Canino, and F. Priolo, "Electroluminescence and transport properties in amorphous silicon nanostructures," *Nanotechnology*, vol. 17, no. 5, pp. 1428–1436, 2006.

[90] C. He, J. Li, X. Wu, P. Chen, J. Zhao, K. Yin, M. Cheng, W. Yang, G. Xie, D. Wang, D. Liu, R. Yang, D. Shi, Z. Li, L. Sun, and G. Zhang, "Tunable electroluminescence in planar graphene/sio2 memristors," *Advanced Materials*, vol. 25, no. 39, pp. 5593–5598, 2013.

[91] J. L. Frieiro, J. López-Vidrier, O. Blázquez, D. Yazlcloğlu, S. Gutsch, J. Valenta, S. Hernández, M. Zacharias, and B. Garrido, "Silicon nanocrystals-based electroluminescent resistive switching device," *Journal of Applied Physics*, vol. 126, no. 14, 2019.

[92] J. I. Gonzalez, T. H. Lee, M. D. Barnes, Y. Antoku, and R. M. Dickson, "Quantum mechanical single-gold-nanocluster electroluminescent light source at room temperature," *Physical Review Letters*, vol. 93, no. 14, pp. 1–4, 2004.

[93] J. M. Woodcock and J. E. Ralph, "Electroluminescence from MIS and MIM structures," *Journal of Non-Crystalline Solids*, vol. 11, pp. 83–96, jul 1972.

[94] R. Salh, "Defect Related Luminescence in Silicon Dioxide Network: A Review," in *Crystalline Silicon - Properties and Uses*, InTech, jul 2011.

[95] T. Anutgan, M. Anutgan, I. Atilgan, and B. Katircioglu, "Electroformed silicon nitride based light emitting memory device," *Applied Physics Letters*, vol. 111, no. 5, 2017.

[96] J. Zheng, C. Zhang, and R. M. Dickson, "Highly fluorescent, water-soluble, size-tunable gold quantum dots," *Physical Review Letters*, vol. 93, no. 7, pp. 5–8, 2004.

[97] R. A. Rosenberg, G. K. Shenoy, P. S. Kim, and T. K. Sham, "Temporal-And site-specific determination of the origin of the luminescent bands in silicon nanowires," *Journal of Physical Chemistry C*, vol. 112, no. 36, pp. 13943–13946, 2008.

[98] Y. Yu, G. Fan, A. Fermi, R. Mazzaro, V. Morandi, P. Ceroni, D. M. Smilgies, and B. A. Korgel, "Size-Dependent Photoluminescence Efficiency of Silicon Nanocrystal Quantum Dots," *Journal of Physical Chemistry C*, vol. 121, no. 41, pp. 23240–23248, 2017.

[99] P. Anger, P. Bharadwaj, and L. Novotny, "Enhancement and quenching of single-molecule fluorescence," *Physical Review Letters*, vol. 96, no. 11, pp. 3–6, 2006.

[100] A. Derkachova, K. Kolwas, and I. Demchenko, "Dielectric Function for Gold in Plasmonics Applications: Size Dependence of Plasmon Resonance Frequencies and Damping Rates for Nanospheres," *Plasmonics*, vol. 11, no. 3, pp. 941–951, 2016.

[101] T. Zellweger, "Atomic photon source," Master's thesis, ETH Zurich, 2020. Master thesis.

[102] B. Cheng, T. Zellweger, K. Malchow, X. Zhang, M. Lewerenz, E. Passerini, J. Aeschlimann, U. Koch, M. Luisier, A. Emboras, A. Bouhelier, and J. Leuthold, "Atomic scale memristive photon source," *Light: Science and Applications*, vol. 11, p. 78, dec 2022.

[103] O. Jambois, H. Rinnert, X. Devaux, and M. Vergnat, "Photoluminescence and electroluminescence of size-controlled silicon nanocrystallites embedded in Si O 2 thin films," *Journal of Applied Physics*, vol. 98, no. 4, pp. 2–5, 2005.

[104] J. Valenta, N. Lalic, and J. Linnros, "Electroluminescence microscopy and spectroscopy of silicon nanocrystals in thin SiO2 layers," *Optical Materials*, vol. 17, no. 1-2, pp. 45–50, 2001.

[105] G. Franzò, A. Irrera, E. C. Moreira, M. Miritello, F. Iacona, D. Sanfilippo, G. Di Stefano, P. G. Fallica, and F. Priolo, "Electroluminescence of silicon nanocrystals in MOS structures," *Applied Physics A: Materials Science and Processing*, vol. 74, no. 1, pp. 1–5, 2002.

[106] J. Zheng, P. R. Nicovich, and R. M. Dickson, "Highly Fluorescent Noble-Metal Quantum Dots," *Annual Review of Physical Chemistry*, vol. 58, pp. 409–431, may 2007.

[107] A. Kuzmina, M. Parzefall, P. Back, T. Taniguchi, K. Watanabe, A. Jain, and L. Novotny, "Resonant Light Emission from Graphene/Hexagonal Boron Nitride/Graphene Tunnel Junctions," *Nano Letters*, pp. 1–14, 2021.

[108] R. Verberk, A. M. Van Oijen, and M. Orrit, "Simple model for the power-law blinking of single semiconductor nanocrystals," *Physical Review B - Condensed Matter and Materials Physics*, vol. 66, no. 23, pp. 1–4, 2002.

[109] N. Amecke, A. Heber, and F. Cichos, "Distortion of power law blinking with binning and thresholding," *Journal of Chemical Physics*, vol. 140, no. 11, pp. 0–8, 2014.

[110] C. Galland, Y. Ghosh, A. Steinbrück, M. Sykora, J. A. Hollingsworth, V. I. Klimov, and H. Htoon, "Two types of luminescence blinking revealed by spectroelectrochemistry of single quantum dots," *Nature*, vol. 479, no. 7372, pp. 203–207, 2011.

[111] P. Frantsuzov, M. Kuno, B. Jankó, and R. A. Marcus, "Universal emission intermittency in quantum dots, nanorods and nanowires," *Nature Physics*, vol. 4, pp. 519–522, jul 2008.

[112] F. D. Stefani, J. P. Hoogenboom, and E. Barkai, "Beyond quantum jumps: Blinking nanoscale light emitters," *Physics Today*, vol. 62, no. 2, pp. 34–39, 2009.

[113] C. M. Galloway, C. Artur, J. Grand, and E. C. Le Ru, "Photobleaching of fluorophores on the surface of nanoantennas," *Journal of Physical Chemistry C*, vol. 118, no. 49, pp. 28820–28830, 2014.

[114] E. C. Le Ru, P. G. Etchegoin, and M. Meyer, "Enhancement factor distribution around a single surface-enhanced Raman scattering hot spot and its relation to single molecule detection," *Journal of Chemical Physics*, vol. 125, no. 20, pp. 1–14, 2006.

[115] Y. Fang, N. H. Seong, and D. D. Dlott, "Measurement of the distribution of site enhancements in surface-enhanced raman scattering," *Science*, vol. 321, no. 5887, pp. 388–392, 2008.

[116] E. C. Le Ru and P. G. Etchegoin, "Phenomenological local field enhancement factor distributions around electromagnetic hot spots," *Journal of Chemical Physics*, vol. 130, no. 18, 2009.

[117] D. a. Clayton, D. M. Benoist, Y. Zhu, and S. Pan, "Photoluminescence and Nanowires," *ACS Nano*, vol. 4, no. 4, pp. 2363–2373, 2010.

[118] X. Wu and E. K. Yeow, "Fluorescence blinking dynamics of silver nanoparticle and silver nanorod films," *Nanotechnology*, vol. 19, no. 3, 2008.

[119] C. T. Yuan, W. C. Chou, J. Tang, C. A. Lin, W. H. Chang, J. L. Shen, and D. S. Chuu, "Single fluorescent gold nanoclusters," *Optics Express*, vol. 17, no. 18, p. 16111, 2009.

[120] M. Kuno, D. P. Fromm, H. F. Hamann, A. Gallagher, and D. J. Nesbitt, "Nonexponential "blinking" kinetics of single CdSe quantum dots: A universal power law behavior," *The Journal of Chemical Physics*, vol. 112, no. 7, pp. 3117–3120, 2000.

[121] P. Bharadwaj and L. Novotny, "Robustness of quantum dot power-law blinking," *Nano Letters*, vol. 11, no. 5, pp. 2137–2141, 2011.

[122] J. Ziegler, R. Klaiss, A. Blaikie, D. Miller, V. R. Horowitz, and B. J. Alemán, "Deterministic Quantum Emitter Formation in Hexagonal Boron Nitride via Controlled Edge Creation," *Nano Letters*, vol. 19, no. 3, pp. 2121–2127, 2019.

[123] M. Pelton, G. Smith, N. F. Scherer, and R. A. Marcus, "Evidence for a diffusion-controlled mechanism for fluorescence blinking of colloidal quantum dots," *Proceedings of the National Academy of Sciences of the United States of America*, vol. 104, no. 36, pp. 14249–14254, 2007.

[124] L. P. Watkins and H. Yang, "Detection of intensity change points in time-resolved single-molecule measurements," *Journal of Physical Chemistry B*, vol. 109, no. 1, pp. 617–628, 2005.

[125] R. Verberk and M. Orrit, "Photon statistics in the fluorescence of single molecules and nanocrystals: Correlation functions versus distributions of on- and off-times," *Journal of Chemical Physics*, vol. 119, no. 4, pp. 2214–2222, 2003.

[126] J. M. Lupton and J. Vogelsang, "Photon correlations probe the quantized nature of light emission from optoelectronic materials," *Applied Physics Reviews*, vol. 8, p. 041302, dec 2021.

[127] J. Wang, Z. Li, C. P. Yao, F. Xue, Z. X. Zhang, and G. Hüttmann, "Brownian diffusion of gold nanoparticles in an optical trap studied by fluorescence correlation spectroscopy," *Laser Physics*, vol. 21, no. 1, pp. 130–136, 2011.

[128] A. Michelman-Ribeiro, D. Mazza, T. Rosales, T. J. Stasevich, H. Boukari, V. Rishi, C. Vinson, J. R. Knutson, and J. G. McNally, "Direct measurement of association and dissociation rates of DNA binding in live cells by fluorescence correlation spectroscopy," *Biophysical Journal*, vol. 97, no. 1, pp. 337–346, 2009.

[129] F. Höfling and T. Franosch, "Anomalous transport in the crowded world of biological cells," *Reports on Progress in Physics*, vol. 76, no. 4, 2013.

[130] W. P. Ambrose, T. Basché, and W. E. Moerner, "Detection and spectroscopy of single pentacene molecules in a p-terphenyl crystal by means of fluorescence excitation," *The Journal of Chemical Physics*, vol. 95, no. 10, pp. 7150–7163, 1991.

[131] J. Y. P. Butter and B. Hecht, "Fast determination of saturation intensity and maximum emission rate by single-emitter imaging," *Optics Express*, vol. 14, no. 20, p. 9350, 2006.

[132] Becker-Hickl, "Classic tcspc," Nov 2019. [Online; accessed 08-February-2022].

[133] T.-H. Lee, J. I. Gonzalez, and R. M. Dickson, "Strongly enhanced field-dependent single-molecule electroluminescence," *Proceedings of the National Academy of Sciences*, vol. 99, no. 16, pp. 10272–10275, 2002.

[134] X. Brokmann, L. F. Marshall, and M. G. Bawendi, "Revealing single emitter spectral dynamics from intensity correlations in an ensemble fluorescence spectrum," *Optics Express*, vol. 17, no. 6, p. 4509, 2009.

[135] J. J. Yang, D. B. Strukov, and D. R. Stewart, "Memristive devices for computing," *Nature Nanotechnology*, vol. 8, no. 1, pp. 13–24, 2013.

[136] K. H. Kim, S. Gaba, D. Wheeler, J. M. Cruz-Albrecht, T. Hussain, N. Srinivasa, and W. Lu, "A functional hybrid memristor crossbar-array/CMOS system for data storage and neuromorphic applications," *Nano Letters*, vol. 12, no. 1, pp. 389–395, 2012.

[137] G. Indiveri, E. Linn, and S. Ambrogio, "ReRAM-Based Neuromorphic Computing," *Resistive Switching*, pp. 715–736, 2016.

[138] Z. Wang, H. Wu, G. W. Burr, C. S. Hwang, K. L. Wang, Q. Xia, and J. J. Yang, "Resistive switching materials for information processing," *Nature Reviews Materials*, vol. 5, no. 3, pp. 173–195, 2020.

[139] Y. Zhu, C. Wu, Z. Xu, Y. Liu, H. Hu, T. Guo, T. W. Kim, Y. Chai, and F. Li, "Light-Emitting Memristors for Optoelectronic Artificial Efferent Nerve," *Nano Letters*, vol. 21, no. 14, pp. 6087–6094, 2021.

[140] B. Cheng, *Tip-enhanced atomic memristor*. PhD thesis, ETH Zurich, 2021.

[141] Y. Yang, P. Gao, S. Gaba, T. Chang, X. Pan, and W. Lu, "Observation of conducting filament growth in nanoscale resistive memories," *Nature Communications*, vol. 3, 2012.

[142] W. Sun, B. Gao, M. Chi, Q. Xia, J. J. Yang, H. Qian, and H. Wu, "Understanding memristive switching via in situ characterization and device modeling," *Nature Communications*, vol. 10, no. 1, pp. 1–13, 2019.

[143] C. F. Chang, J. Y. Chen, C. W. Huang, C. H. Chiu, T. Y. Lin, P. H. Yeh, and W. W. Wu, "Direct Observation of Dual-Filament Switching Behaviors in Ta2O5-Based Memristors," *Small*, vol. 13, no. 15, pp. 1–7, 2017.

[144] T. H. Lee, J. I. Gonzalez, and R. M. Dickson, "Strongly enhanced field-dependent single-molecule electroluminescence," *Proceedings of the National Academy of Sciences of the United States of America*, vol. 99, no. 16, pp. 10272–10275, 2002.

[145] T. Vosch, Y. Antoku, J. C. Hsiang, C. I. Richards, J. I. Gonzalez, and R. M. Dickson, "Strongly emissive individual DNA-encapsulated Ag nanoclusters as single-molecule fluorophores," *Proceedings of the National Academy of Sciences of the United States of America*, vol. 104, no. 31, pp. 12616–12621, 2007.

[146] H. Nishikawa, "Structures and properties of amorphous silicon dioxide—Issues on the reliability and novel applications," in *Silicon-Based Material and Devices*, vol. 2, pp. 93–122, Elsevier, 2001.

[147] L. Skuja, M. Hirano, and H. Hosono, "Oxygen-Related Intrinsic Defects in Glassy SiO2 : Interstitial Ozone Molecules," *Physical Review Letters*, vol. 84, pp. 302–305, jan 2000.

[148] Y. Sakurai, K. Nagasawa, H. Nishikawa, and Y. Ohki, "Characteristic red photoluminescence band in oxygen-deficient silica glass," *Journal of Applied Physics*, vol. 86, no. 1, pp. 370–373, 1999.

[149] S. Menzel and J.-H. Hur, "Modeling the VCM- and ECM-Type Switching Kinetics," *Resistive Switching*, pp. 395–436, 2016.

[150] S. Choi, R. M. Dickson, and J. Yu, "Developing luminescent silver nanodots for biological applications," *Chemical Society Reviews*, vol. 41, no. 5, pp. 1867–1891, 2012.

[151] J. J. Velázquez, V. K. Tikhomirov, L. F. Chibotaru, N. T. Cuong, A. S. Kuznetsov, V. D. Rodríguez, M. T. Nguyen, and V. V. Moshchalkov, "Energy level diagram and kinetics of luminescence of Ag nanoclusters dispersed in a glass host," *Optics Express*, vol. 20, no. 12, p. 13582, 2012.

[152] H. Van Houten and C. Beenakker, "Quantum point contacts," *Physics Today*, vol. 49, no. 7, pp. 22–27, 1996.

[153] O. Scholder, K. Jefimovs, I. Shorubalko, C. Hafner, U. Sennhauser, and G.-L. Bona, "Helium focused ion beam fabricated plasmonic antennas with sub-5 nm gaps," *Nanotechnology*, vol. 24, p. 395301, sep 2013.

[154] L. D. Menard and J. M. Ramsey, "Fabrication of sub-5 nm nanochannels in insulating substrates using focused ion beam milling," *Nano Letters*, vol. 11, pp. 512–517, Feb 2011.

[155] K. Kuhnke, C. Große, P. Merino, and K. Kern, "Atomic-scale imaging and spectroscopy of electroluminescence at molecular interfaces," *Chemical Reviews*, vol. 117, no. 7, pp. 5174–5222, 2017.

[156] E. D. Fung and L. Venkataraman, "Too Cool for Blackbody Radiation: Overbias Photon Emission in Ambient STM Due to Multielectron Processes," *Nano Letters*, vol. 20, pp. 8912–8918, dec 2020.

[157] A. Rosławska, P. Merino, A. Grewal, C. C. Leon, K. Kuhnke, and K. Kern, "Atomic-Scale Structural Fluctuations of a Plasmonic Cavity," *Nano Letters*, vol. 21, no. 17, pp. 7221–7227, 2021.

[158] C. M. Gruber, L. Herrmann, E. P. Bellido, J. Dössegger, A. Olziersky, U. Drechsler, G. Puebla-Hellmann, G. A. Botton, L. Novotny, and E. Lörtscher, "Resonant Optical Antennas with Atomic-Sized Tips and Tunable Gaps Achieved by Mechanical Actuation and Electrical Control," *Nano Letters*, vol. 20, pp. 4346–4353, jun 2020.

[159] L. Gerhard and W. Wulfhekel, "Conductance and adhesion in an atomically precise Au-Au point contact," *Physical Review B*, vol. 101, no. 3, pp. 1–7, 2020.

[160] H. Huntington, "Electromigration in Metals," in *Diffusion in Solids*, pp. 303–352, Elsevier, 1975.

[161] D. G. Pierce and P. G. Brusius, "Electromigration: A review," *Microelectronics Reliability*, vol. 37, no. 7 SPEC. ISS., pp. 1053–1072, 1997.

[162] K. O'Neill, E. A. Osorio, and H. S. J. Van Der Zant, "Self-breaking in planar few-atom au constrictions for nanometer-spaced electrodes," *Applied Physics Letters*, vol. 90, no. 13, pp. 1–3, 2007.

[163] P. S. Ho and T. Kwok, "Electromigration in metals," *Reports on Progress in Physics*, vol. 52, pp. 301–348, mar 1989.

[164] H. Ceric and S. Selberherr, "Electromigration in submicron interconnect features of integrated circuits," *Materials Science and Engineering R: Reports*, vol. 71, no. 5-6, pp. 53–86, 2011.

[165] A. Dasgupta, M. Buret, N. Cazier, M. M. Mennemanteuil, R. Chacon, K. Hammani, J. C. Weeber, J. Arocas, L. Markey, G. C. des Francs, A. Uskov, I. Smetanin, and A. Bouhelier, "Electromigrated electrical optical antennas for transducing electrons and photons at the nanoscale," *Beilstein Journal of Nanotechnology*, vol. 9, no. 1, pp. 1964–1976, 2018.

[166] L. Cui, Y. Zhu, M. Abbasi, A. Ahmadivand, B. Gerislioglu, P. Nordlander, and D. Natelson, "Electrically Driven Hot-carrier Generation and Above-threshold Light Emission in Plasmonic Tunnel Junctions," *Nano Letters*, 2020.

[167] L. Cui, Y. Zhu, P. Nordlander, M. D. Ventra, and D. Natelson, "Thousand-fold Increase in Plasmonic Light Emission via Combined Electronic and Optical Excitations," *Nano Letters*, vol. 21, no. 6, pp. 2658–2665, 2021.

[168] Y. Zhu, L. Cui, and D. Natelson, "Hot-carrier enhanced light emission: The origin of above-threshold photons from electrically driven plasmonic tunnel junctions," *Journal of Applied Physics*, vol. 128, no. 23, p. 233105, 2020.

[169] K. Kaasbjerg and A. Nitzan, "Theory of Light Emission from Quantum Noise in Plasmonic Contacts: Above-Threshold Emission from Higher-Order Electron-Plasmon Scattering," *Physical Review Letters*, vol. 114, p. 126803, mar 2015.

[170] W. S. Fann, R. Storz, H. W. K. Tom, and J. Bokor, "Electron thermalization in Gold-Fann.pdf," *Physical Review B*, vol. 46, no. 20, pp. 13 592—-13595, 1992.

[171] M. L. Brongersma, N. J. Halas, and P. Nordlander, "Plasmon-induced hot carrier science and technology.," *Nature nanotechnology*, vol. 10, no. 1, pp. 25–34, 2015.

[172] M. Bauer, A. Marienfeld, and M. Aeschlimann, "Hot electron lifetimes in metals probed by time-resolved two-photon photoemission," *Progress in Surface Science*, vol. 90, no. 3, pp. 319–376, 2015.

[173] J. R. M. Saavedra, A. Asenjo-Garcia, and F. J. García De Abajo, "Hot-Electron Dynamics and Thermalization in Small Metallic Nanoparticles," *ACS Photonics*, vol. 3, no. 9, pp. 1637–1646, 2016.

[174] A. Giri and P. E. Hopkins, "Transient thermal and nonthermal electron and phonon relaxation after short-pulsed laser heating of metals," *Journal of Applied Physics*, vol. 118, no. 21, 2015.

[175] R. H. M. Groeneveld, R. Sprik, and A. Lagendijk, "Femtosecond spectroscopy of electron-electron and electron-phonon energy relaxation in Ag and Au," *Physical Review B*, vol. 51, no. 17, pp. 11433–11445, 1995.

[176] M. Buret, *Antenne optique tunnel pilotée électriquement : une source lumineuse large bande à l'échelle du nanomètre.* PhD thesis, Universite Bourgogne, 2019. Thèse de doctorat dirigée par Bouhelier, Alexandre Physique Bourgogne Franche-Comté 2019.

[177] C. Ott, S. Götzinger, and H. B. Weber, "Thermal origin of light emission in nonresonant and resonant nanojunctions," *Physical Review Research*, vol. 2, no. 4, p. 42019, 2020.

[178] J. J. Greffet, P. Bouchon, G. Brucoli, and F. Marquier, "Light Emission by Nonequilibrium Bodies: Local Kirchhoff Law," *Physical Review X*, vol. 8, no. 2, p. 21008, 2018.

[179] A. Martín-Jiménez, K. Lauwaet, Ó. Jover, D. Granados, A. Arnau, V. M. Silkin, R. Miranda, and R. Otero, "Electronic Temperature and Two-Electron Processes in Overbias Plasmonic Emission from Tunnel Junctions," *Nano Letters*, no. 111, 2021.

[180] O. Demichel, M. Petit, S. Viarbitskaya, R. Méjard, F. De Fornel, E. Hertz, F. Billard, A. Bouhelier, and B. Cluzel, "Dynamics, Efficiency, and Energy Distribution of Nonlinear Plasmon-Assisted Generation of Hot Carriers," *ACS Photonics*, vol. 3, no. 5, pp. 791–795, 2016.

[181] R. Méjard, A. Verdy, M. Petit, A. Bouhelier, B. Cluzel, and O. Demichel, "Energy-Resolved Hot-Carrier Relaxation Dynamics in Monocrystalline Plasmonic Nanoantennas," *ACS Photonics*, vol. 3, no. 8, pp. 1482–1488, 2016.

[182] N. L. Schneider, G. Schull, and R. Berndt, "Optical probe of quantum shot-noise reduction at a single-atom contact," *Physical Review Letters*, vol. 105, no. 2, pp. 1–4, 2010.

[183] M. A. Fikiet, D. Tuschel, V. V. Ermolenkov, and I. K. Lednev, "Clarifying Glass Luminescence at Near-Infrared Excitation," *Applied Spectroscopy*, vol. 74, no. 2, pp. 187–192, 2020.

[184] A. Mooradian, "Photoluminescence of metals," *Physical Review Letters*, vol. 22, no. 5, pp. 185–187, 1969.

[185] P. Apell, R. Monreal, and S. Lundqvist, "Photoluminescence of noble metals," *Physica Scripta*, vol. 38, no. 2, pp. 174–179, 1988.

[186] M. Beversluis, A. Bouhelier, and L. Novotny, "Continuum generation from single gold nanostructures through near-field mediated intraband transitions," *Physical Review B - Condensed Matter and Materials Physics*, vol. 68, no. 11, pp. 1–10, 2003.

[187] J. B. Khurgin, "Ultimate limit of field confinement by surface plasmon polaritons," *Faraday Discussions*, vol. 178, pp. 109–122, 2015.

[188] J. Mertens, M. E. Kleemann, R. Chikkaraddy, P. Narang, and J. J. Baumberg, "How Light Is Emitted by Plasmonic Metals," *Nano Letters*, vol. 17, no. 4, pp. 2568–2574, 2017.

[189] G. T. Boyd, Z. H. Yu, and Y. R. Shen, "Photoinduced luminescence from the noble metals and its enhancement on roughened surfaces," *Physical Review B*, vol. 33, no. 12, pp. 7923–7936, 1986.

[190] P. Biagioni, M. Celebrano, M. Savoini, G. Grancini, D. Brida, S. Mátéfi-Tempfli, M. Mátéfi-Tempfli, L. Duò, B. Hecht, G. Cerullo, and M. Finazzi, "Dependence of the two-photon photoluminescence yield of gold nanostructures on the laser pulse duration," *Physical Review B - Condensed Matter and Materials Physics*, vol. 80, no. 4, pp. 1–5, 2009.

[191] K. Imura, T. Nagahara, and H. Okamoto, "Near-field two-photon-induced photoluminescence from single gold nanorods and imaging of plasmon modes," *Journal of Physical Chemistry B*, vol. 109, no. 27, pp. 13214–13220, 2005.

[192] D. Xie, F. O. Laforge, I. Grigorenko, and H. A. Rabitz, "Dual coherent and incoherent two-photon luminescence in single gold nanorods revealed by polarization and time-resolved nonlinear autocorrelation," *Journal of the Optical Society of America B*, vol. 36, no. 7, p. 1931, 2019.

[193] P. Biagioni, D. Brida, J. S. Huang, J. Kern, L. Duò, B. Hecht, M. Finazzi, and G. Cerullo, "Dynamics of four-photon photoluminescence in gold nanoantennas," *Nano Letters*, vol. 12, no. 6, pp. 2941–2947, 2012.

[194] J. Wang, E. Gürdal, A. Horneber, S. Dickreuter, S. Kostcheev, A. J. Meixner, M. Fleischer, P. M. Adam, and D. Zhang, "Carrier recombination and plasmonic emission channels in metallic photoluminescence," *Nanoscale*, vol. 10, no. 17, pp. 8240–8245, 2018.

[195] J. Chen, A. Krasavin, P. Ginzburg, A. V. Zayats, T. Pullerits, and K. J. Karki, "Evidence of High-Order Nonlinearities in Supercontinuum White-Light Generation from a Gold Nanofilm," *ACS Photonics*, vol. 5, no. 5, pp. 1927–1932, 2018.

[196] T. Haug, P. Klemm, S. Bange, and J. M. Lupton, "Hot-Electron Intraband Luminescence from Single Hot Spots in Noble-Metal Nanoparticle Films," *Physical Review Letters*, vol. 115, no. 6, pp. 1–5, 2015.

[197] L. Roloff, P. Klemm, I. Gronwald, R. Huber, J. M. Lupton, and S. Bange, "Light Emission from Gold Nanoparticles under Ultrafast Near-Infrared Excitation: Thermal Radiation, Inelastic Light Scattering, or Multiphoton Luminescence?," *Nano Letters*, vol. 17, pp. 7914–7919, dec 2017.

[198] Y. Zhang, J. Han, L. Shi, S. Chen, Z. Feng, H. Lu, M. Gu, and X. Li, "Extremely Polarized and Efficient Hot Electron Intraband Luminescence from Aluminum Nanostructures for Nonlinear Optical Encoding," *Laser and Photonics Reviews*, vol. 15, no. 1, pp. 1–9, 2021.

[199] C. López-Bastidas, "Thermalization time of noble metal nanoparticles: Effects of the electron density profile," *European Physical Journal B*, vol. 85, no. 2, 2012.

[200] A. Giri, J. T. Gaskins, B. M. Foley, R. Cheaito, and P. E. Hopkins, "Experimental evidence of excited electron number density and temperature effects on electron-phonon coupling in gold films," *Journal of Applied Physics*, vol. 117, no. 4, 2015.

[201] S. T. Weber and B. Rethfeld, "Laser-excitation of electrons and nonequilibrium energy transfer to phonons in copper," *Applied Surface Science*, vol. 417, pp. 64–68, 2017.

[202] E. P. Silaeva, E. Bevillon, R. Stoian, and J. P. Colombier, "Ultrafast electron dynamics and orbital-dependent thermalization in photoexcited metals," *Physical Review B*, vol. 98, no. 9, p. 94306, 2018.

[203] Winter, Mark, "Webelements gold." `https://www.webelements.com/gold/`, 2021. [Online; accessed 20-March-2021].

[204] Y. Sivan and Y. Dubi, "Theory of " hot " photoluminescence from Drude metals," *ACS Nano*, pp. 1–25, apr 2021.

[205] Z. Lin, L. V. Zhigilei, and V. Celli, "Electron-phonon coupling and electron heat capacity of metals under conditions of strong electron-phonon nonequilibrium," *Physical Review B - Condensed Matter and Materials Physics*, vol. 77, no. 7, pp. 1–17, 2008.

[206] Y. Y. Cai, E. Sung, R. Zhang, L. J. Tauzin, J. G. Liu, B. Ostovar, Y. Zhang, W. S. Chang, P. Nordlander, and S. Link, "Anti-stokes emission from hot carriers in gold nanorods," *Nano Letters*, vol. 19, no. 2, pp. 1067–1073, 2019.

[207] O. P. Varnavski, M. B. Mohamed, M. A. El-Sayed, and T. Goodson, "Relative enhancement of ultrafast emission in gold nanorods," *Journal of Physical Chemistry B*, vol. 107, no. 14, pp. 3101–3104, 2003.

[208] L. Mandel and E. Wolf, *Optical Coherence and Quantum Optics*. Cambridge University Press, 1995.

[209] R. Glauber, "Photon correlations," *Physical Review Letters*, vol. 10, no. 7, pp. 276–277, 1963.

[210] F. Davidson, "Measurements of photon correlations in a laser beam near threshold with time-to-amplitude converter techniques," *Physical Review*, vol. 185, no. 2, pp. 446–453, 1969.

[211] E. Purcell, "HBT response," *Nature*, vol. 178, no. 4548, pp. 1449–1450, 1956.

[212] U. Fano, "Quantum Theory of Interference Effects in the Mixing of Light from Phase-Independent Sources," *American Journal of Physics*, vol. 29, no. 8, pp. 539–545, 1961.

[213] R. Feynman and A. Zee, *QED: The Strange Theory of Light and Matter.* Alix G. Mautner memorial lectures, Princeton University Press, 2006.

[214] J. Stöhr, "Overcoming the diffraction limit by multi-photon interference: a tutorial," *Advances in Optics and Photonics*, vol. 11, no. 1, p. 215, 2019.

[215] F. Boitier, A. Godard, E. Rosencher, and C. Fabre, "Measuring photon bunching at ultrashort timescale by two-photon absorption in semiconductors," *Nature Physics*, vol. 5, no. 4, pp. 267–270, 2009.

[216] B. Bai, J. Liu, Y. Zhou, H. Zheng, H. Chen, S. Zhang, Y. He, F. Li, and Z. Xu, "Photon superbunching of classical light in the Hanbury Brown–Twiss interferometer," *Journal of the Optical Society of America B*, vol. 34, no. 10, p. 2081, 2017.

[217] C. W. J. Beenakker and H. Schomerus, "Counting statistics of photons produced by electronic shot noise," *Physical Review Letters*, vol. 86, no. 4, pp. 700–703, 2001.

[218] C. W. J. Beenakker and H. Schomerus, "Antibunched photons emitted by a quantum point contact out of equilibrium," *Physical Review Letters*, vol. 93, no. 9, pp. 1–4, 2004.

[219] I. C. Fulga, F. Hassler, and C. W. J. Beenakker, "Nonzero temperature effects on antibunched photons emitted by a quantum point contact out of equilibrium," *Physical Review B*, vol. 81, p. 115331, mar 2010.

[220] C. C. Leon, A. Rosławska, A. Grewal, O. Gunnarsson, K. Kuhnke, and K. Kern, "Photon superbunching from a generic tunnel junction," *Science Advances*, vol. 5, pp. 1–6, may 2019.

[221] J. C. Forgues, C. Lupien, and B. Reulet, "Emission of microwave photon pairs by a tunnel junction," *Physical Review Letters*, vol. 113, no. 4, pp. 1–5, 2014.

[222] J. O. Simoneau, S. Virally, C. Lupien, and B. Reulet, "Photon-pair shot noise in electron shot noise," *Physical Review B*, vol. 95, no. 6, pp. 1–5, 2017.

[223] J. Koch, F. Von Oppen, and A. V. Andreev, "Theory of the Franck-Condon blockade regime," *Physical Review B - Condensed Matter and Materials Physics*, vol. 74, no. 20, pp. 1–19, 2006.

[224] T. H. Park and M. Galperin, "Self-consistent full counting statistics of inelastic transport," *Physical Review B - Condensed Matter and Materials Physics*, vol. 84, no. 20, pp. 1–8, 2011.

[225] M. O. Scully, *Quantum optics.* Cambridge, England: Cambridge University Press, 2008 - 1997.

[226] P. K. Tan, G. H. Yeo, H. S. Poh, A. H. Chan, and C. Kurtsiefer, "Measuring temporal photon bunching in blackbody radiation," *Astrophysical Journal Letters*, vol. 789, no. 1, pp. 1–5, 2014.

[227] C. Kurtsiefer, P. Zarda, S. Mayer, and H. Weinfurter, "The breakdown flash of silicon avalanche photodiodes - Back door for eavesdropper attacks?," *Journal of Modern Optics*, vol. 48, no. 13 SPEC., pp. 2039–2047, 2001.

[228] R. Hanbury Brown and R. Q. Twiss, "Correlation between photons in two coherent beams of light," *Nature*, vol. 4497, pp. 27–29, 1956.

[229] A. Delteil, C. Tat Ngai, T. Fink, and A. İmamoğlu, "Second-order photon correlation measurement with picosecond resolution using frequency upconversion," *Optics Letters*, vol. 44, p. 3877, aug 2019.

[230] L. Mandel, "Concept of Cross-Spectral Purity in Coherence Theory," *Journal of the Optical Society of America*, vol. 51, no. 12, p. 1342, 1961.

[231] D. B. Scarl, "Measurements of photon correlations in partially coherent light," *Physical Review*, vol. 175, no. 5, pp. 1661–1668, 1968.

[232] L. Novotny and B. Hecht, *Principles of Nano-Optics.* Cambridge: Cambridge University Press, 2012.

[233] Y. Shih, *An introduction to quantum optics : photon and biphoton physics.* Series in Optics and Optoelectronics, Boca Raton, Florida ;: CRC Press, 2011 - 2011.

[234] Y. Qu and S. Singh, "Measurements of photon statistics in second harmonic generation," *Physical Review A*, vol. 51, no. 3, pp. 2530–2536, 1995.

[235] B. Romeira and A. Fiore, "Purcell Effect in the Stimulated and Spontaneous Emission Rates of Nanoscale Semiconductor Lasers," *IEEE Journal of Quantum Electronics*, vol. 54, no. 2, pp. 1–12, 2018.

[236] K. Braun, F. Laible, O. Hauler, X. Wang, A. Pan, M. Fleischer, and A. J. Meixner, "Active optical antennas driven by inelastic electron tunneling," *Nanophotonics*, vol. 7, no. 9, pp. 1503–1516, 2018.

[237] S. P. Gurunarayanan, N. Verellen, V. S. Zharinov, F. James Shirley, V. V. Moshchalkov, M. Heyns, J. Van De Vondel, I. P. Radu, and P. Van Dorpe, "Electrically Driven Unidirectional Optical Nanoantennas," *Nano Letters*, vol. 17, no. 12, pp. 7433–7439, 2017.

[238] J. Kern, R. Kullock, J. Prangsma, M. Emmerling, M. Kamp, and B. Hecht, "Electrically driven optical antennas," *Nature Photonics*, vol. 9, no. 9, pp. 582–586, 2015.

[239] Y. Vardi, E. Cohen-Hoshen, G. Shalem, and I. Bar-Joseph, “Fano Resonance in an Electrically Driven Plasmonic Device,” *Nano Letters*, vol. 16, no. 1, pp. 748–752, 2016.

[240] X. He, J. Tang, H. Hu, J. Shi, Z. Guan, S. Zhang, and H. Xu, “Electrically Driven Optical Antennas Based on Template Dielectrophoretic Trapping,” *ACS Nano*, vol. 13, no. 12, pp. 14041–14047, 2019.

[241] J. Tang, H. Hu, X. He, Y. Xu, Y. Zhang, Z. Guan, S. Zhang, and H. Xu, “Switchable Electrically Driven Optical Antenna Based on Ultrathin Amorphous Silica,” *Advanced Optical Materials*, vol. 9, no. 19, pp. 1–9, 2021.

[242] P. Grimm, S. Zeißner, M. Rödel, S. Wiegand, S. Hammer, M. Emmerling, E. Schatz, R. Kullock, J. Pflaum, and B. Hecht, “Color-Switchable Subwavelength Organic Light-Emitting Antennas,” *Nano Letters*, vol. 22, no. 3, pp. 1032–1038, 2022.

[243] K. Braun, X. Wang, D. Zhang, and A. J. Meixner, “Hot-electron-induced light amplification,” *Journal of Photonics for Energy*, vol. 6, no. 4, p. 42506, 2016.

[244] S. Liu, A. Hammud, M. Wolf, and T. Kumagai, “Anti-Stokes Light Scattering Mediated by Electron Transfer Across a Biased Plasmonic Nanojunction,” *ACS Photonics*, vol. 8, no. 9, pp. 2610–2617, 2021.

[245] L. Cui, Y. Zhu, P. Nordlander, M. Di Ventra, and D. Natelson, “Thousand-fold Increase in Plasmonic Light Emission via Combined Electronic and Optical Excitations,” *Nano Letters*, vol. 21, no. 6, pp. 2658–2665, 2021.

[246] R. H. Brown and R. Q. Twiss, “The Question of Correlation between Photons in Coherent Beams of Light,” *Nature*, vol. 178, no. 4548, pp. 1447–1448, 1956.